# DESIGN AND INVESTIGATION ON SUBSTRATE INTEGRATED WAVEGUIDE FED DIELECTRIC RESONATOR ANTENNAS FOR D-BAND APPLICATIONS

A thesis submitted in fulfillment of the requirements for the
degree of

Doctor of Philosophy in Engineering

(ELECTRONIC ENGINEERING)

by

**Emmanuel Kiprop Chemweno**

COLLEGE OF AGRICULTURE, ENGINEERING AND SCIENCE

UNIVERSITY OF KWAZULU-NATAL

DURBAN-4041 SOUTH AFRICA

November 2023

# DESIGN AND INVESTIGATION ON SUBSTRATE INTEGRATED WAVEGUIDE FED DIELECTRIC RESONATOR ANTENNAS FOR D-BAND APPLICATIONS

**Emmanuel Kiprop Chemweno**

A thesis submitted in fulfillment of the requirements for the

degree of

Doctor of Philosophy: Electronic Engineering

Discipline of Electrical, Electronic and Computer Engineering

School of Engineering, College of Agriculture, Engineering and Science

University of Kwazulu-Natal, Durban, South Africa

Supervisor: Prof. Pradeep Kumar

Co-supervisor: Prof. Thomas Afullo

As the candidate's supervisors, we agree to the submission of this thesis.

Signed ....................................Date ....................................

Name: Prof. Pradeep Kumar

Signed ....................................Date ....................................

Name: Prof. Thomas J. O. Afullo

# Declaration 1 - Plagiarism

I, **Emmanuel Kiprop Chemweno**, declare that;

1. The research reported in this thesis, except where otherwise indicated, is my original research.
2. This thesis has not been submitted for any degree or examination at any other university.
3. This thesis does not contain other persons' data, pictures, graphs or other information, unless specifically acknowledged as being sourced from other persons.
4. This thesis does not contain other persons' writing, unless specifically acknowledged as being sourced from other researchers. Where other written sources have been quoted, then:
    (a) Their words have been re-written but the general information attributed to them has been referenced,
    (b) Where their exact words have been used, then their writing has been placed in italics and inside quotation marks, and referenced.
5. This thesis does not contain text, graphics or tables copied and pasted from the Internet, unless specifically acknowledged, and the source being detailed in the thesis and in the References sections.

Signed ....... [redacted] .......Date .....................................

# Declaration 2 - Publications

DETAILS OF CONTRIBUTION TO PUBLICATIONS that form part and/or include research presented in this thesis:

(i) E. K. Chemweno, P. Kumar and T. J. O. Afullo, ”Substrate Integrated Waveguide - Dielectric Resonator Antenna for Future Wireless Communication,” in SAIEE Africa Research Journal, vol. 113, no. 3, Sept. 2022, pp. 119-128, doi: 10.23919/SAIEE.2022.9853021.

(ii) E. K. Chemweno, P. Kumar, T. J. O. Afullo, ”Design of high-gain wideband substrate integrated waveguide dielectric resonator antenna for D-band applications,” in Optik, Volume 272, 2023, pp. 1-15, doi.org/10.1016/j.ijleo.2022.170261.

(iii) E. K. Chemweno, P. Kumar, T. J. O. Afullo, ”Investigation on the use of Metamaterial Polarization-Rotator Wall for Isolation Improvement in SIW-Fed MIMO DRA for D-Band Applications”, submitted to Optics & Laser Technology, 2023.

(iv) E. K. Chemweno, P. Kumar and T. J. O. Afullo, ”Bandwidth Enhancement of a Substrate Integrated Waveguide Dielectric Resonator Antenna using Metallic Shorting Vias,” 2022 International Conference on Electromagnetics in Advanced Applications (ICEAA), Cape Town, South Africa, 2022, pp. 302-305, doi: 10.1109/ICEAA49419.2022.9899987.

(v) E. K. Chemweno, P. Kumar and T. J. O. Afullo, ”Design of Dual-band Substrate Integrated Waveguide Dielectric Resonator Antenna in D-band,” 2023 IEEE AFRICON, Nairobi, Kenya, 2023, pp. 1-5, doi: 10.1109/AFRICON55910.2023.10293347.

Signed ...................................Date ....................................

# Acknowledgements

I first would like to give glory to the Almighty God for His unending love and mercies.

I would like to express my deepest gratitude to my supervisors, Professor Pradeep Kumar and Professor Thomas Afullo for their mentorship, guidance and inspiration throughout my studies.

I am also indebted to my fellow colleagues at Howard, friends and the UKZN fraternity for their invaluable support and encouragement. Special thanks go to the *braai* family for the friendship we cherished.

Finally, I wish to extend my sincere appreciation to my family, for their love, patience and understanding during this period. “I share this achievement with you”.

To all of you who made me accomplish this work, I pray that the Almighty God bless you abundantly.

# Abstract

This thesis is devoted to the design of substrate integrated waveguide (SIW) fed dielectric resonator antennas (DRAs) for D-band applications. These antennas are necessary to establish high-speed communication links in wireless communication networks so as to support the emerging broadband applications such as the internet of things (IoTs), smart cities, virtual reality among others. Some of these applications demand for networks that can support high data rates and low latencies that exceed the capabilities of 5G networks. Consequently, communication systems are projected to operate in the millimeter wave (mm-wave) and terahertz (THz) frequencies.

The D-band frequency spectrum is attractive for utilization in 6G communication systems owing to its vast bandwidths and is capable of very high data rates up to terabits per second (Tbps). However, this band suffers the limitations of short propagation distances due to the increased path losses at high frequencies. These effects can be mitigated by efficient antenna designs characterized by broad bandwidths and high-gains with low-loss interconnect networks. In addition, antenna structures with low profiles are attractive for ease of integration with other front-end devices.

In this work, the substrate integrated waveguide fed dielectric resonator antenna is the preferred topology for the antenna design. Three different wideband antenna designs are presented and analyzed. The wideband operation of the presented designs is achieved through the higher-order mode (HOM) excitation of the dielectric resonator (DR) element to achieve multiple resonances in this frequency band. Adjacent resonances are merged together using various impedance matching techniques to enhance the antenna bandwidth. These designs investigate on different impedance matching techniques such as the use of defected ground structures (DGS), inductive metal vias (posts), cross-slots among others for antenna bandwidth enhancement and gain improvement. This work extends further the design of single element antenna to multiple-input multiple-output (MIMO) antenna design. A technique for mutual coupling reduction in closely packed antenna elements, which is based on metamaterial polarization rotation is presented and investigated. The investigation on the performance of the antennas is carried out using the commercial CST Microwave Studio full-wave electromagnetic simulator. The simulation results are analyzed in terms of the bandwidth, gain, radiation efficiency and radiation characteristics.

The first design presents a SIW-DRA operating between 122.58 GHz and 139.51 GHz. The antenna exhibits multiple resonances at 123.64 GHz, 125.76 GHz, 127.4 GHz, 129.9 GHz, 134.9 GHz and 137.7 GHz. The design investigates the use of DGS and iris-type discontinuity techniques for impedance matching improvement of a multi-resonant antenna. Simulation results show that the applied techniques are effective in merging together the adjacent bands of a multiband antenna for bandwidth enhancement. The antenna achieves a -10 dB impedance bandwidth of 13.4%, a peak gain of 12.3 dBi,

maximum directivity of 13.14 dBi and a high radiation efficiency of 84%. In addition, the antenna possesses stable broadband radiation patterns across the frequency band of operation.

The second design presents a novel approach for the transformation of a dual-band SIW-DRA to a broadband antenna design. The design proposes systematic and sequential application of impedance matching techniques to improve the impedance matching in the stop band of the dual-band antenna without deterioration of its performance in the passbands. In the development of this approach, two preliminary designs are presented and investigated. The first preliminary design investigates the use of inductive metal vias in the SIW feeding structure for bandwidth enhancement. The effects of incorporating inductive via and DGS on the SIW feed structure of a dual-band antenna operating between 140.82 GHz - 145.24 GHz and 147.27 GHz - 151.02 GHz with a relatively narrow stop band of 2.03 GHz are investigated. The simulated results show that the inductive via and DGS effectively merge together the passbands of a dual-band antenna to achieve a wideband response of 138.27 GHz - 150.95 GHz. The second preliminary design presents a dual-band antenna operating between 126.95 GHz - 136.5 GHz and 139.67 GHz - 149.48 GHz in the lower and upper-frequency bands. The antenna is optimized for dual-band operation through the modification of the feeding slot to an I-shape to achieve a bandwidth 9.55 GHz and 9.81 GHz, representing fractional bandwidths of 7.2% and 6.78% in the lower and upper-frequency bands respectively. The impedance matching in the relatively wide stop band can be improved to merge together the passbands of the dual-band antenna to achieve a wideband response. This transformation is achieved through the use of inductive via, matching stub and DRA offset techniques in the dual-band antenna design. These techniques are systematically applied to the dual-band design and the parameters optimized to achieve a high-gain and wide bandwidth SIW-DRA. The antenna operates between 123.97 GHz and 152.13 GHz, with a -10 dB impedance bandwidth of 20.39% at the center frequency of 138.05 GHz, exhibiting a high gain of 11.67 dBi, directivity of 13.36 dBi and maximum total radiation efficiency of 79%. The radiation characteristics of the higher-order resonances excited at 124.38 GHz, 125.22 GHz, 130.28 GHz, 140.72 GHz, 141.59 GHz, 143.47 GHz, 149.7 GHz and 151.17 GHz show broadside radiation patterns.

The research also focuses on the design of a wideband and low-isolation 2 × 2 SIW-DRA based MIMO antenna. Initially, a single-element SIW-DRA is designed based on higher-order mode excitation with the antenna exhibiting multiple resonances. Different impedance matching techniques involving the embedding of inductive metal vias in the SIW feed, cross-slot feed and stepped-impedance sections are employed to minimize reflections and to achieve a good impedance matching between 136.68 GHz – 166.28 GHz. A -10 dB bandwidth performance of 19.5%, a gain of 11.06 dBi and a high radiation efficiency of 84% is achieved. Two antenna elements are linearly arranged with zero inter-element distance in a 2 × 2 MIMO configuration to achieve high integration of antenna elements in a given space. A metamaterial-based decoupling network is investigated for isolation enhancement in the 2 × 2 MIMO configuration. The decoupling network is designed as a metamaterial polarization rotator (MTMPR) wall to rotate the polarization

state of the electromagnetic wave transmitting through it. The MTMPR wall is integrated with the MIMO antenna for mutual coupling reduction. The Simulation results show that the MTMPR wall does not degrade the bandwidth performance of the MIMO antenna, and the presented design achieves an isolation performance greater than 21.16 dB across the entire bandwidth of operation. Besides the isolation, the antenna is analyzed by evaluating its diversity metrics. MIMO diversity metrics such as the envelope correlation coefficient (ECC), diversity gain (DG), mean effective gain (MEG), channel capacity loss (CCL) and the total active reflection coefficient (TARC) are evaluated. The MIMO design achieves an ECC of 0.008, DG $>$ 9.9 between the two ports, MEG $<$ 3 dB, TARC close to -10 dB for different phase angles of the input excitation and a CCL below 0.4 bits/s/Hz.

The performances of the presented SIW-DRA designs are compared with published results and confirmed to meet the established minimum criteria for the appraisal of the presented designs. The results show that the presented designs are suitable for application in future 6G wireless systems.

# Contents

# List of Figures

# List of Tables

# Abbreviations and acronyms

**3GPP** Third Generation Partnership Project

**4G** Fourth Generation Communication Systems

**5G** Fifth Generation Communication Systems

**6G** Sixth Generation Communication Systems

**ABS** Absolute

**AiP** Antenna in-Package

**AMC** Artificial Magnetic Conductor

**AoC** Antenna on-Chip

**BiCMOS** Bipolar Complementary Metal-Oxide Semiconductor

**BMW** Beamwidth

**CBS** Cavity Backed Slot

**CCL** Channel Capacity Loss

**CDRA** Cylindrical Dielectric Resonator Antenna

**CMOS** Complementary Metal-Oxide Semiconductor

**CPSS** Circular-polarization Selective Surface

**CP** Circularly Polarized

**CSRR** Complementary Split-ring Resonator

**CST MWS** Computer Simulation Technology Microwave Studio

**DG** Diversity Gain

**DGS** Defected Ground Structure

**DR** Dielectric Resonator

**DRA** Dielectric Resonator Antenna

**DWM** Dielectric Waveguide Model

**EIRP** Effective Isotropic Radiated Power

**EBG** Electromagnetic Bandgap

**ECC** Envelope Correlation Coefficient

**eMBB** enhanced Mobile Broadband

**FR1** Frequency Range 1

**FR2** Frequency Range 2

**FSS** Frequency Selective Surface

**Gbps** Gigabits per second

**HDI** High Density Interconnect

**HIS** High Impedance Surface

**HMSIW** Half-Mode Substrate Integrated Waveguide

**HOM** Higher-Order Mode

**IoT** Internet of Things

**IPD** Integrated Passive Device

**LBE** Localized Backside Etching

**LHCP** Left Hand Circularly Polarized

**LP** Linearly Polarized

**LTCC** Low Temperature Co-fired Ceramic

**LWA** Leaky Wave Antenna

**ME** Magneto-electric

**MEG** Mean Effective Gain

**MIMO** Multiple-Input Multiple-Output

**MLD** Main Lobe Direction

**mm-wave** Millimeter wave

**MMIC** Monolithic Microwave Integrated Circuit

**mMTC** massive Machine Type Communication

**MOL** Method of Lines

**MPA** Microstrip Patch Antenna

**MRWG** Microstrip Ridge gap Waveguide

**MTM** Metamaterial

**MTMPR** Metamaterial Polarization Rotator

**MWM** Magnetic Wall Model

**NFV** Network Function Virtualization

**NR** New Radio

**PBG** Photonic Bandgap

**PCB** Printed Circuit Board

**PCR** Polarization Conversion Rate

**PEC** Perfect Electric Conductor

**PMC** Perfect Magnetic Conductor

**RDL** Redistribution Layer

**RDRA** Rectangular Dielectric Resonator Antenna

**RHCP** Right Hand Circularly Polarized

**RWG** Rectangular Waveguide

**SIW** Substrate Integrated Waveguide

**SLL** Side Lobe Level

**SRR** Split-ring Resonator

**TARC** Total Active Reflection Coefficient

**Tbps** Terabits per second

**TE** Transverse Electric

**THz** Terahertz

**TM** Transverse Magnetic

**uRLLC** ultra-Reliable Low Latency Communication

**WLP** Wafer-Level Package

# Chapter 1

# INTRODUCTION

## 1.1 Background information

Over the last two decades, there has been an increase in demand for reliable high-speed wireless communication systems and networks. These are required to provide high-speed data links necessary to support the emerging broadband wireless applications and services. These applications which constitute the internet of things (IoT), smart cities, machine-to-machine communication, virtual reality, smart healthcare systems, etc. are becoming integral to daily human life [1]. These demands which are occasioned by the emerging 5G applications have stimulated rapid advances in innovations and technology. As a result, there has been a sharp increase in the number of interconnected mobile equipment that seeks to integrate all these applications into a single platform.

The high connection densities due to the massive number of interconnected devices pose the challenges of congestion in mobile access networks and backhaul systems. In anticipation of these challenges, the Third Generation Partnership Project (3GPP) identified and enumerated key scenarios for the fulfillment of the requirements for emerging applications as: enhanced Mobile Broadband (eMBB), massive Machine Type Communications (mMTC) and Ultra-Reliable Low-Latency Communications (uRLLC) [1], [2]. Despite these scenarios defining different performance requirements, they point to the need for more spectrum [3]. This spectrum demand is expected to push the communication carrier frequencies to the unlicensed 5G millimeter (mm) waves band and beyond. The need to fulfill these requirements demands for several network revolutions. These revolutions include signal transmission in the mm-wave frequencies, signal modulation to conserve bandwidth, frame structure arrangement of data, flexible channel multiplexing, network function virtualization (NFV), network slicing and 5G massive MIMO antennas [4].

5G is currently being commercially deployed in the FR1 (sub-6 GHz) as well as the FR2 (mm-wave) NR bands. The mm-wave band (24 GHz - 52 GHz) is expected to deliver higher data rates, with a peak rate projection of up to 20 Gbps. Despite 5G offering significant improvements compared to 4G, it still has limitations in terms of seamless coverage. Applications and services such as global coverage, ultra-high data rate transmission, ultra-dense connections, high precision positioning etc. require communication performances that is beyond the capabilities of 5G [5]. It is envisaged that these limitations will be addressed by future wireless communication systems. These systems, dubbed 6G, are still in its initial stages of exploration. Exploitation of higher frequencies is necessary to provide the global coverage in 6G communication. The terahertz (THz) band is defined for 100 GHz - 10 THz and is potential for utilization in 6G communication systems because of the enormous bandwidths required for ultra-high data rate services. The THz band lies between the mm-waves and optical frequencies and remains the largely unexplored frequency 'gap'. This spectrum is characterized by large bandwidths, high path loss as well as high molecular absorption.

The THz technology remains potential as a key enabler for future wireless communication systems. However, this band has traditionally not been considered for wireless communications owing to lack of compact THz signal sources and efficient transceivers [6], [7]. Recent advances in electronic and photonic THz transceiver designs have enabled efficient generation and modulation of THz signals. The electronic solutions are based on the extension of the mm-wave silicon-based device technologies to the THz band. However, there exists a maximum operating frequency which is dictated by the transistor frequency characteristics. For silicon-based BiCMOS/CMOS transistors, the maximum operation frequency lies between 110 GHz - 250 GHz [7]. The initial deployment of 6G is expected to be in the sub-THz band between the frequencies of 100 GHz and 300 GHz. This is because the technology in this frequency range is more mature [8]. On the contrary, the THz frequencies in the infrared spectrum (above 300 GHz) introduce additional challenges of spreading losses and short propagation distances due to low-power THz transmitters [9].

The D-band spectrum constitutes part of the sub-THz frequencies ranging from 110 GHz to 170 GHz. This spectrum is characterized by low signal attenuation due to atmospheric absorption and is becoming attractive as a frontier for 6G communications. This band has been gaining attention in the recent years for possible exploitation in high-speed communication systems that are capable of transferring data up to terabit per second (Tbps). This is evident from the number of emerging publications on the characterizations of the D-band channel as well as design of accessories such as transceivers, amplifiers, modulators, filters, antennas, power dividers etc. One limitation of the D-band frequencies is the increased path loss. At high frequencies, attenuation due to atmospheric absorption, rain-induced fading and foliage cannot be neglected [10]. These effects limit the range of communication leading to short propagation distances. To compensate for these path losses and the effects of reduced power generation ability of active electronic devices at higher frequencies, antenna systems with high effective radiated power are desirable. Therefore, there is need for high-gain, efficient and broadband antenna designs at these high frequencies to mitigate the high path loss and maintain a reliable communication.

Different types of antenna structures have been proposed for D-band applications. They include horn antennas [11], microstrip patches [12], substrate integrated waveguide (SIW) slot antennas [13], dielectric resonator antennas (DRAs) [14], magneto-electric (ME) dipole antennas [15] etc. At high frequencies, the physical size of the antenna is greatly reduced because of the short wavelengths. This makes it feasible to design miniaturized and compact antennas which may be realized using low-profile planar structures. The microstrip patch antenna (MPA) is a low-cost, planar antenna that is easy to design and fabricate. However, they are based on metallic patches, which suffer the drawbacks of narrow bandwidths and increased ohmic losses [16]. Besides, the effects of surface waves cause poor radiation efficiency and introduces distortion in the radiation pattern [17]. Dielectric resonators (DRs) is a class of high permittivity and low-loss ceramic materials that is suitable for application as antenna elements at high frequencies. The bandwidth performance and radiation efficiency of a DRA is superior to that of a MPA. Moreover, its attributes of light-weight, low-profile and small size make them possible for miniaturization [18] for the purposes of integration.

A low-loss feed is necessary for high-gain antenna performance. At high frequencies, the losses associated with the microstrip feeding is considerably high. The SIW is a low-loss interconnect that is capable of minimizing the radiation losses associated with the microstrip feeding. Its low-profile and ease of fabrication using printed circuit board (PCB) technology makes it versatile for integration with other circuit elements. This makes it attractive for construction of antenna feed networks at high frequencies. Besides, it provides a convenient way for integration of the antenna with other front-end devices.

## 1.2 Motivation

The D-band spectrum is suitable for exploitation for 6G wireless communication networks because it can support large bandwidths and high data rates without additional spectral efficiency enhancement techniques. However, there are challenges associated with the design and implementation of D-band links. D-band frequencies suffer the disadvantage of short propagation distances because of the high path losses associated with high frequencies.

There is need for designs of broadband wireless communication systems that are capable of overcoming these limitations. This requires that a wireless system should possess sufficient effective isotropic radiated power (EIRP). At high frequencies, there is limitation on the amount of power generated by the electronic devices. This low-power handling capability remains a significant hurdle in achieving sufficient EIRP. Therefore, the key challenge for wireless communication systems lie in the design of high-performance antennas and the associated feed networks.

## 1.3 Objectives

The main aim of this thesis is to design wideband and high-gain antennas for application in the D-band frequency spectrum. D-band antennas should possess high gains and high radiation efficiencies to mitigate the high free-space path losses. In addition, they should have broad bandwidths in order to realize the high data rate potential of the D-band frequencies. Some the critical parameters to consider in the design of the antennas are the antenna topology and its associated feed method, material properties and tolerances in antenna fabrication. It is also desirable to integrate the antenna elements with other front end devices for the development of integrated communication components. This requires that antenna elements be of low profile and compact size for ease of integration. This lead to close packing of antenna elements in designs that require multiple antenna systems such as MIMO technology. This poses the potential problem of increased mutual coupling. The need to satisfy these requirements presents the design challenges for D-band antennas. The specific objectives in the design D-band antennas are as follows:

i. Carry out a literature survey on the requirements of high-frequency antennas and the different antenna structures proposed for applications in the millimeter wave and D-band frequencies.

ii. Design and simulation of wideband and high-gain substrate integrated waveguide fed dielectric resonator antennas for D-band frequency applications.

iii. Design and simulation of a metamaterial based decoupling network for isolation improvement in MIMO antennas.

iv. Design and simulation of a high-isolation SIW-DRA based MIMO antenna with closely packed elements.

## 1.4 Scope of the thesis

This thesis investigates on the design of SIW fed DRAs for D-band frequency band. The scope of this thesis include the following:

- Review of performance requirements of antenna elements for high frequency applications. The review involves extensive studies on different antenna structures and associated feed networks proposed for D-band frequencies to establish their suitability for application in future wireless communication systems. The review also investigates on the various techniques applied for mutual coupling reduction in closely spaced antennas.

- Design, simulation and analysis of different SIW-DRA designs in the D-band spectrum. This involves the selection of materials for the antenna and feed elements and the determination of antenna dimensional parameters. The modeling, simulation, parameter optimization and performance analysis of the SIW-DRA designs is carried out using CST MWS and HFSS software.

- Comparative analysis of the performances of the SIW-DRA designs with other published works comprising of different designs, topologies, feed configurations among others.

## 1.5 Research contributions

The contribution of this research is in the design of wideband antennas for future generation wireless communication systems. The specific contributions may be outlined as follows:

- The first contribution is the investigation of different techniques involving the modifications of the SIW feeding structure for bandwidth enhancement of DRAs. The excitation of higher-order modes (HOMs) in DRAs and the use of techniques that involve modifications of the DR elements have been demonstrated in low-frequency antennas. This research explains the difficulty posed by the fabrication technologies on the tolerances and precision of DR elements at high frequencies, rendering techniques on the modifications of the SIW feed to be attractive.
- The second contribution is the design of wideband SIW-DRAs from dual-band designs. This contribution demonstrates the feasibility of the transformation of a dual-band or multiband DRA to a wideband DRA and also suggests an approach for the transformation. It further demonstrates that it is possible to target improvement of impedance matching in the stop band without deteriorating the performance in the passbands.
- Another contribution is the finding that a SIW structure offers a robust feed structure for MIMO applications. The SIW confines electromagnetic energy within itself which minimizes circulating currents between different antenna elements that cause low isolation. This enables the individual MIMO elements to be spaced very close to each other to achieve high integration of antenna elements.
- The fourth contribution of this research is the minimization of the mutual coupling in closely packed MIMO antenna elements. This research work demonstrates that a metamaterial (MTM) wall structure can be used to minimize the spatial interactions of electromagnetic fields between adjacent DRs for isolation improvement.

## 1.6 Thesis layout

This thesis is organized into six chapters as follows:

**Chapter one** is the introduction to the study. The motivation for the design of high-performance antennas for high-frequency applications is outlined. The contributions of this research is also presented.

**Chapter two** presents a brief literature review on the previous works reported on D-band antennas. A brief description of the fundamental parameters used in the characterization of the performance of antennas is presented. This chapter reviews the different antenna structures and topologies for applications in this frequency regime. The theoretical principles of the DRA radiators and SIW feeds are also outlined. The concept of MIMO antennas and metamaterial structures are also presented.

**Chapter three** presents a wideband SIW-DRA D-band antenna design. The design is based on the use of a defected ground structure (DGS) and via offset impedance matching techniques for the realization of a wideband antenna design.

In **chapter four**, a wideband and high-gain SIW-DRA antenna is presented. The wideband design is based on the merging together the passbands of a dual-band antenna. Initially, the embedding of inductive shorting vias in the SIW feeding structure is investigated for DRA bandwidth performance enhancement. This inductive via technique is applied to a dual-band antenna design to achieve impedance matching in the relatively wide stop band for bandwidth broadening. As a result, a method of conversion of a dual-band antenna to a wideband antenna design, through the systematic application of different impedance matching techniques is presented.

**Chapter five** presents a SIW-DRA based MIMO antenna design. The design allows for close packing together of antenna elements to achieve high integration. A metamaterial polarization rotator shield with a high polarization conversion rate is also designed. This shield is integrated with the MIMO antenna to rotate the polarization of the spatially interacting fields so as to minimize the effects of mutual coupling of the MIMO elements.

**Chapter six** presents the summary and conclusion of these research works. Suggestion for future works is also presented.

# Chapter 2

# LITERATURE REVIEW

## 2.1 Introduction

The development of D-band antennas for future wireless communication systems began in earnest in the last four decades. To date, there exist vast amounts of literature on the different antenna topologies and designs for communication and sensing applications. The physically-small sizes of these antennas make it possible for integration with other front-end electronics as single modules or packages. This offers two advantages. First, there is minimization of interconnection losses leading to improved antenna radiation efficiency. The second advantage is that the integrated antenna is smaller and cheaper in comparison to a system of separate components [19]. Different packaging technologies have been developed to meet the demands for integrated low-cost devices. In this section, we highlight the different antenna designs and the integration technologies reported in literature for this frequency regime.

Printed circuit board based MPAs and waveguide aperture antennas are attractive choices for a wide range of applications. However, waveguide based antennas are bulky and hence not amenable to integration. The MPA is the most popular antenna structure for a wide range of frequency applications due to its planarity and ease of fabrication. The different D-band antennas based on microstrip patches include the MPA [12], microstrip fed patch arrays [20], SIW-fed patch arrays [21], magneto-electric dipole antennas [15] etc. A microstrip patch antenna proposed on quartz glass substrate [12] is shown in Fig. 2.1. The quartz glass substrate is chosen to minimize the effects of surface waves and the antenna is designed to resonate at 146 GHz with a frequency of operation between 138.70 GHz - 147.80 GHz (6.4%) and a gain of 6.6 dBi. The single element antenna is extended to the design of a $1\times4$ array depicted in Figs. 2.1 (b) and (c), to enhance its gain performance to 11.4 dBi at the cost of bandwidth reduction to 5.9%. In [21], a $4 \times 4$ patch antenna array is designed and investigated. The antenna is fed via a corporate SIW feed network. The antenna is realized using multi-layered substrates using LTCC technology and its structure is shown in Fig. 2.2. The radiating patch is printed on the top substrate and is loaded with a crossed slot and two metallized vias for improved impedance matching. The SIW on substrate 2 feeds the patch through a coupling slot. Layers 2 and 3 constitute the SIW power divider network for feeding the 16-element array. A bandwidth performance of 12.5% and a gain of 16.8 dBi is achieved. Fig. 2.3 shows a ME dipole antenna studied in [15]. This structure is realized through the combination of an electric dipole and a patch that forms two symmetrical mushroom structures. The antenna is excited from a

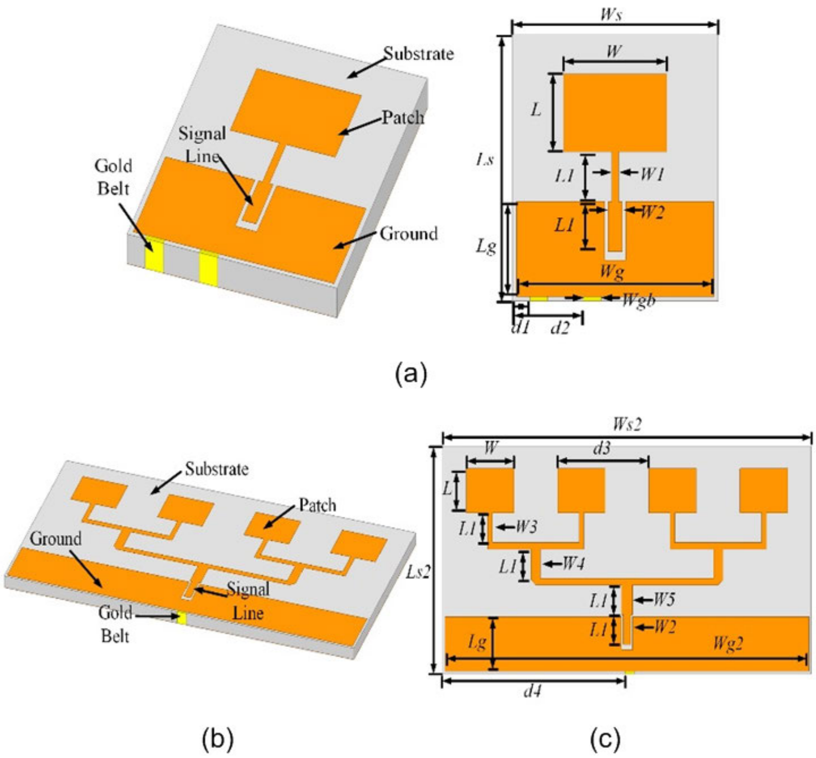

Figure 2.1: Microstrip patch antenna on a quartz glass substrate (a) single patch and (b) & (c) 3D and top view of the 1 × 4 patch array [12]

SIW cavity through a rectangular and H-shaped slot, in a multi-layer structure. A wide bandwidth of 12.8% and a gain of 19.3 dBi is realized. The limitation associated with these types of microstrip patch based antennas is narrow bandwidths and increased ohmic losses at high frequencies. Another class of antennas based on PCB technology is the SIW slotted antennas and arrays shown in Figs. 2.4 and 2.5. A wideband SIW-fed slot antenna is presented in [13]. The antenna is designed to exhibit multiple resonances for the different modes excited in the cavity. A wideband response of 42.86% is achieved, with a peak gain of 10.8 dBi. A low temperature co-fired ceramic (LTCC) based dual-band cavity-backed slot antenna is proposed in [22]. Fig. 2.5 shows the configuration of the different layers of the antenna. Four radiating slots are fed from a resonant substrate integrated cavity through an hour-glass shaped slot. Higher-order modes is used to excite dual-band radiation at 146.6 GHz and 167.2 GHz, with bandwidth performances of 3.89% and 3.95% respectively. Slot based antennas exhibit wide impedance bandwidths compared to MPAs. At high frequencies, the disadvantage associated with standard PCBs is the surface roughness losses in feed lines and distribution networks. These may be minimized by use of advanced PCB technologies capable of achieving high manufacturing tolerances such as the high density interconnect (HDI) technology [19]. Other antenna structures based on microstrip patches implemented using the PCB process include the transmit arrays [23] and the leaky-wave antenna (LWA) [24].

Metallic horn antennas have also been proposed for point-to-point communication in this frequency band. These types of antennas possess wideband and high gain

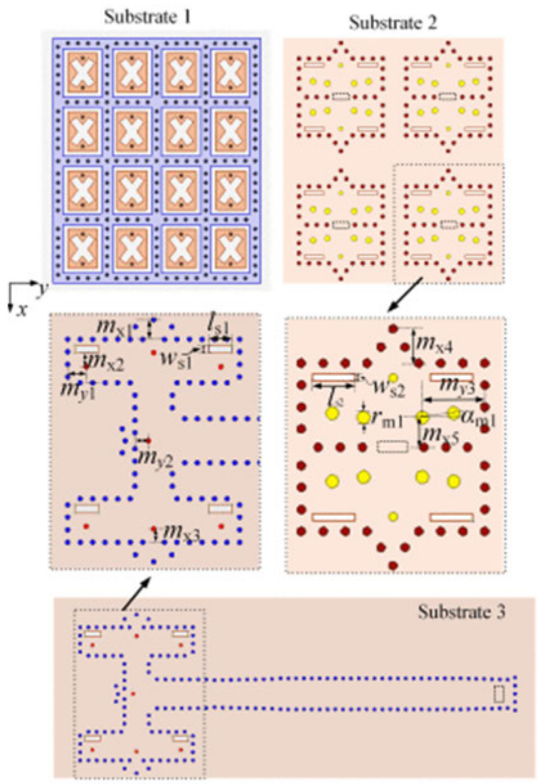

Figure 2.2: Geometry of the 4 × 4 patch antenna array proposed in [21].

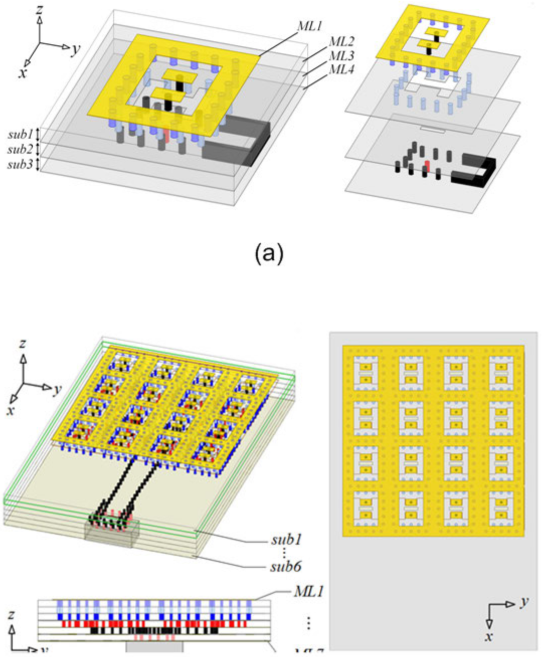

(a)

(b)

Figure 2.3: Magneto-electric dipole antenna (a) exploded view of a single element antenna (b) 3D & top views of a 4 × 4 antenna array configuration [15]

characteristics. A SIW integrated horn antenna based on the PCB process is presented in [11] for short-distance communications. The horn is excited through a planar SIW to

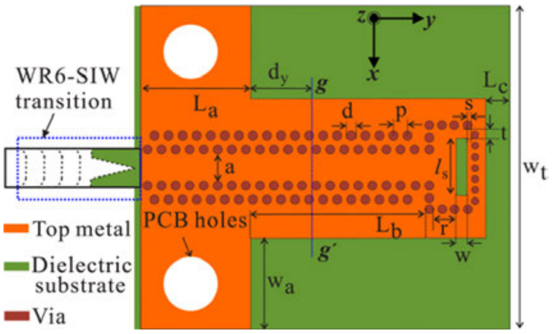

Figure 2.4: Configuration of the SIW slot antenna presented in [13].

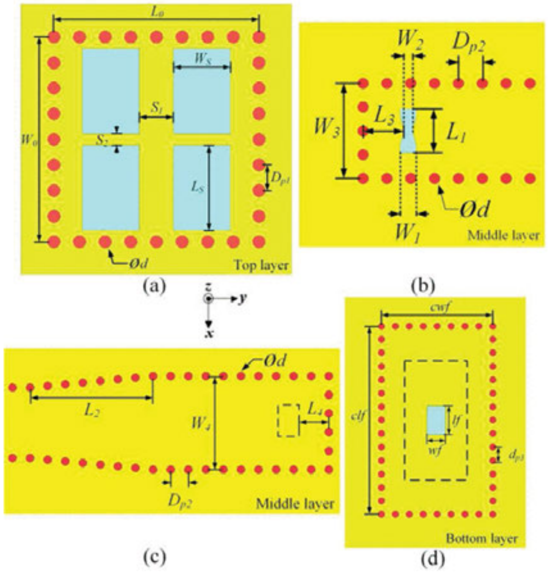

Figure 2.5: Top views of the different layers of a SIW cavity backed slot antenna showing (a) radiation slots and (b), (c) & (d) SIW feeding network [22]

rectangular waveguide (RWG) transition as shown in Fig. 2.6, to achieve a bandwidth of 18.9% and a gain of 15.46 dBi. The gain performance of a horn antenna can be improved by loading the antenna with a dielectric lens. This has been demonstrated in [25], whereby the incorporation of a focusing dielectric lens achieves a gain of 32 dB with increased directivity. Fig. 2.7 shows the proposed dielectric lens-loaded horn antenna. The effect of the lens is to narrow the antenna main lobe width to $5^o$ for increased directivity. The use of arrays has also been proposed for the improvement of the performance of horn antennas in [26]. The researchers therein propose an array of 8 × 8 stepped horn elements implemented in a single metal block. The exploded and cross-sectional views of the proposed array is shown in Fig. 2.8. The antennas are machined on a metal block and placed on top of a power divider feed network to minimize losses. The array configuration achieves a fractional bandwidth of 29.5% and a maximum gain of 32 dBi. The metallic horn antennas have a higher gain and radiation efficiency. However, they are bulky and complex three-dimensional structures that are not suitable for integration with other front-end planar devices.

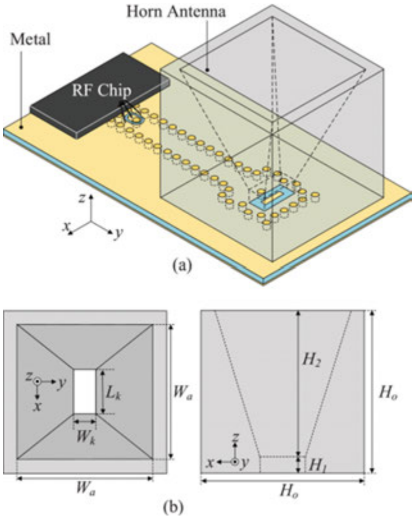

Figure 2.6: Configuration of the integrated horn antenna presented in [11].

Figure 2.7: Structure of the horn antenna with a focusing dielectric lens [25].

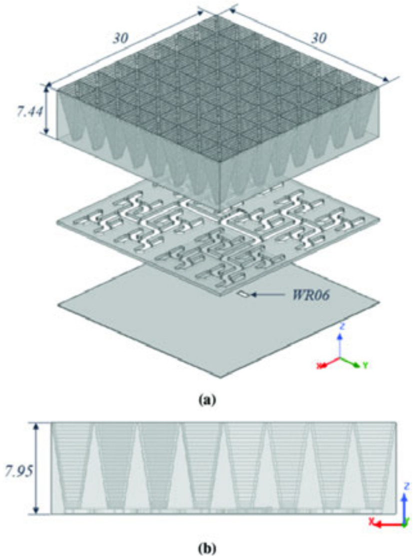

Figure 2.8: (a) Exploded 3D view and (b) cross-sectional view of the $8 \times 8$ slotted antenna array in [26].

Another main challenge that lies in the design of metallic horn antennas is the difficulty of fabrication at high frequencies. Dielectric-based antennas can be manufactured with ease using existing technologies. They may be fabricated in various forms such as dielectric rods, dielectric resonators, dielectric lenses etc. A tapered dielectric rod shown in Fig. 2.9 is proposed for operation between 135 GHz – 145 GHz [27]. The dielectric rod possesses excellent directional capabilities in the end-fire direction with a beamwidth of $34^o$ in both $E$- and $H$- planes and a gain of 19 dB. This tapering effect causes low side-lobe levels. A compact and high-gain DRA is designed for operation between 168 GHz - 178 GHz [28]. The radiating element is a 2-element array of square dielectric frustrums fed from a coplanar waveguide. Fig. 2.10 shows the configuration of the proposed design. The apex of the square pyramid DRA is truncated to form a frustrum for increased antenna performance. The proposed DRA exhibits a gain of 12.24 dBi with a high radiation efficiency of 82%.

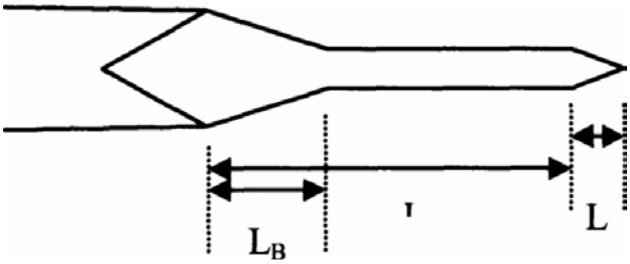

Figure 2.9: Sketch of the tapering dielectric rod antenna [27].

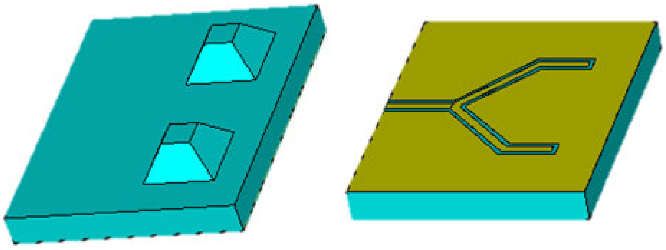

Figure 2.10: Schematic of the proposed DRA and the coplanar feeding network [28].

The demand for single-chip devices has seen the development of different packaging architectures which integrates single or multiple antennas together with other circuit components in a single package. The package-based antennas are broadly categorized into two types: antenna on-chip (AoC) and antenna in-package (AiP) antennas. AiPs are mainly fabricated using the LTCC, HDI and wafer-level package (WLP) technologies. The LTCC technology enables multilayer structures to design three-dimensional radiators. This allows for stacking, design of cavity-backed antennas as well as the use of aperture feeding techniques in highly integrated AiP designs. The HDI technology offers an advantage over the traditional PCB because the high resolution can realize smaller vias, thinner traces, multiple layers as well as smaller components [29]. In WLP technology, the components are packaged on the wafer level. Based on these technologies, a number of AoC package-based antennas have been reported. A compact, differentially fed, AoC patch antenna is reported in [30] for radar measurement applications. The patch is excited using microstrip coupled feed and is integrated with a radar transmitter on-chip as shown in Fig. 2.11. A peak gain of 7 dB is achieved over a frequency of 156 GHz - 166 GHz. The design of an AoC dipole antenna is described in [31]. The dipole antenna is designed using the standard Bi-CMOS process for 165 GHz radar applications. The layout of the design is depicted in Fig. 2.12. The antenna achieves a maximum gain of 6 dBi at 160 GHz. A half-mode SIW (HMSIW) cavity-backed DRA on-chip antenna is proposed in [14]. The configuration of the proposed on-chip DRA using standard CMOS technology with six layers is illustrated in Fig. 2.13. The DRA is excited for higher-order mode operation to achieve a bandwidth of 7% and gain of 7.5 dBi. AoC slot based antennas have also been studied. A microstrip-fed slot antenna is designed in [32]. The structure of the proposed AoC slot antenna is shown in Fig. 2.14. The hybrid structure of the slot antenna and the PCB packaging causes an improvement in the radiation performance of the antenna. A gain performance of 4.9 dBi and a radiation efficiency of 41% is reported, with no mention of the bandwidth.

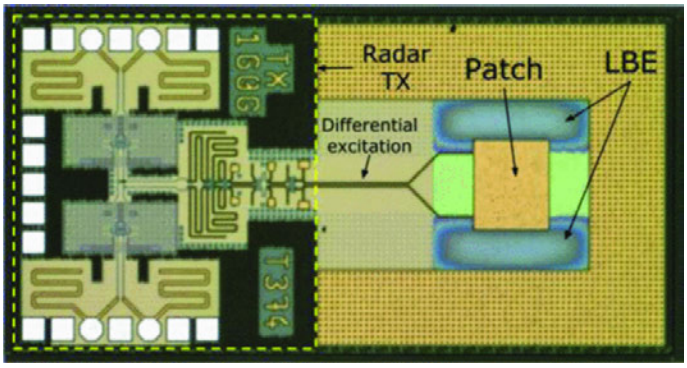

Figure 2.11: Layout of the differentially fed AoC integrated with radar circuits for radar applications [30].

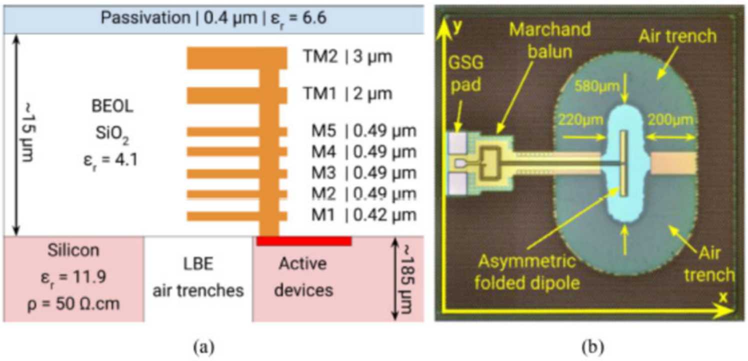

Figure 2.12: (a) Stack-up view and (b) micrograph of the folded dipole antenna described in [31].

On-chip antennas allow for high level of integration. However, their application is limited by low directivities and poor radiation efficiencies due to the poor resistivity of silicon. This is because waves are dissipated as heat as a result of this low resistivity. The AiP technology offers better directivity and radiation efficiency performance. An E-shaped

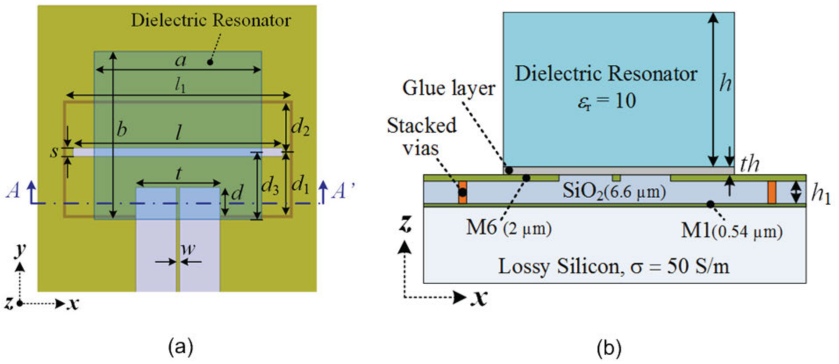

Figure 2.13: Proposed on-chip DRA showing (a) top view and (b) sectional view [14].

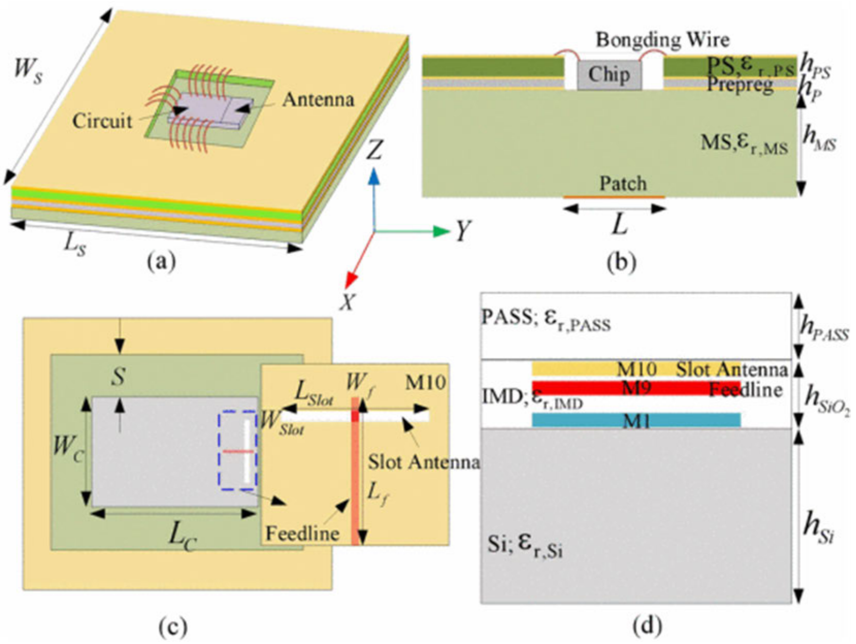

Figure 2.14: Structure of the proposed AoC slot antenna showing (a) 3D view (b) side view (c) top view and (d) sectional side view of the chip [32].

patch for AiP application is designed on a low permittivity quartz substrate shown in Fig. 2.15 [33]. The patch is fed from a microstrip line with two open stubs providing for direct connection of the patch to the monolithic microwave integrated circuit (MMIC) as well as a means of controlling the antenna impedance. The antenna exhibits a 15.2% impedance bandwidth and a gain of about 6 dBi. Another design proposed is a 2 × 2 patch array implemented using AiP technology [34]. The patch elements are designed on an Alumina substrate and fed from a coplanar waveguide as shown in Fig. 2.16. The proposed design resonates at 122 GHz with a gain of 9.9 dBi and a usable bandwidth of 4%. A DRA on package has also been demonstrated based on the HDI PCB technology. A cubic-shaped DRA made of alumina dielectric excited using a microstrip line is presented in [35]. The configuration of the proposed DRA implemented using the AiP technology is shown in Fig. 2.17. The impedance bandwidth of the proposed antenna ranges from 115 GHz to 162 GHz with a gain of 5.5 dBi. Another AiP antenna structure consists of the 4 × 4 array of MPA with a monopole feeder reported in [36]. The antenna is implemented using multilayer PCB technology depicted in Fig. 2.18. The proposed array uses the multimode resonances of the patch and the feeder to realize a wide bandwidth of 53%, gain of 18.1 dBi and a high radiation efficiency of 80%. A D-band ME dipole antenna is also proposed in [37]. The antenna whose structure is shown in Fig. 2.19 is composed of two planar ME dipoles, a center patch and a cavity-backed aperture fed from a low-loss SIW through the slot coupling. A 4 × 2 array is designed from a 2 × 2 subarray of ME dipole elements for gain enhancement. The design achieves a bandwidth from 135.4 to 158.8 GHz (23.4 GHz) with a peak gain of 14.1 dBi at 150 GHz.

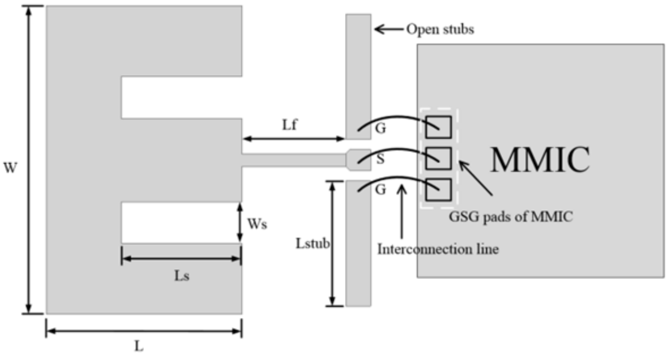

Figure 2.15: Geometry of the E-shaped patch antenna using AiP technology designed in [33].

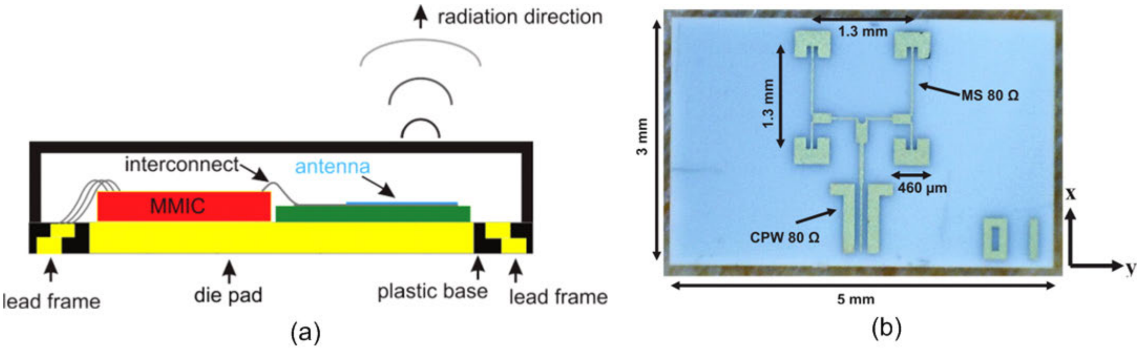

Figure 2.16: Layout of the (a) AiP system and (b) 2 × 2 antenna patch arrays presented in [34].

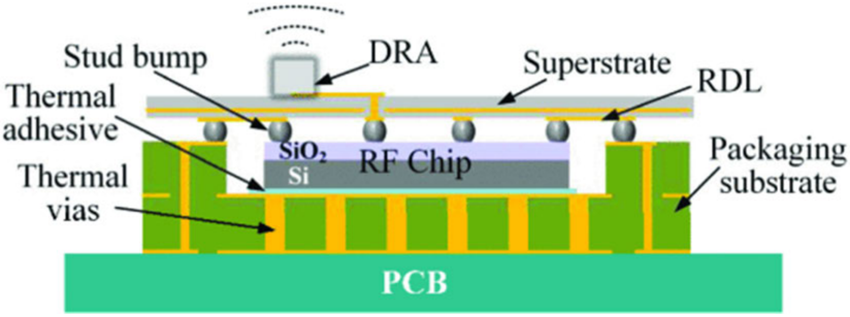

Figure 2.17: Configuration of the AiP DRA proposed in [35].

The packaging materials are also important for antenna system performance. At higher frequencies, the loss tangent ($\tan\delta$) and the surface roughness of the substrates is critical

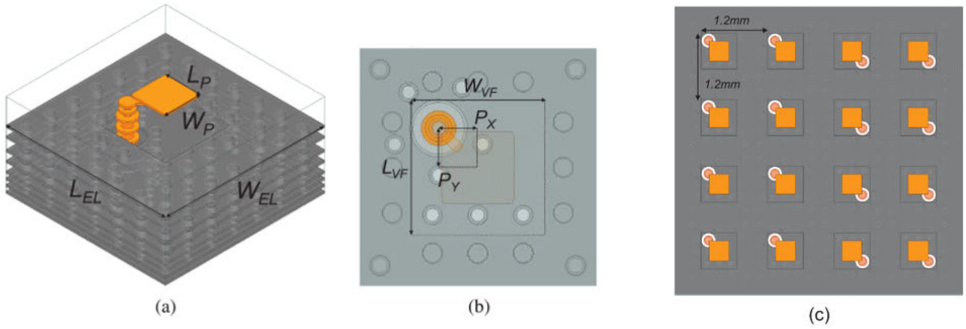

Figure 2.18: Structure of the proposed wideband patch antenna with monopole feed (a) 3D view showing the different layers (b) top view (c) 4 × 4 antenna array [36]

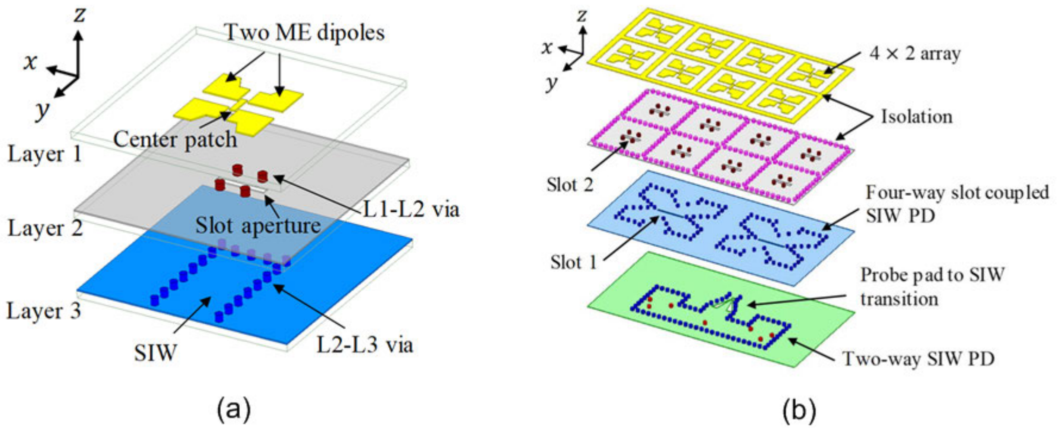

Figure 2.19: Configuration of the proposed ME dipole antenna (a) exploded view showing the different antenna structural layers and (b) 4 × 2 ME antenna array [37]

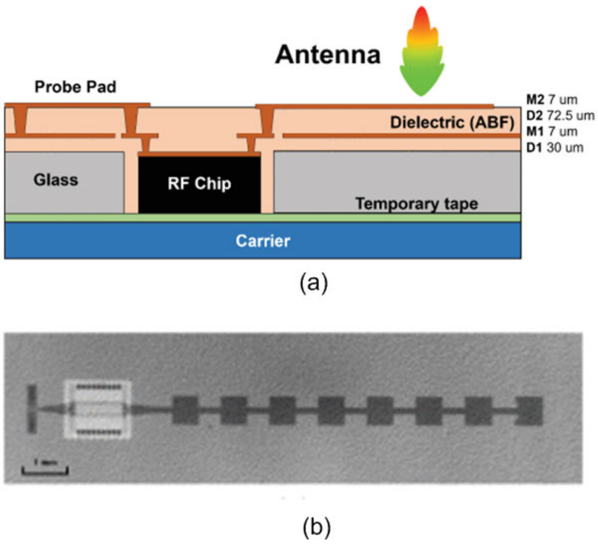

Figure 2.20: Illustrations of (a) Configuration of the material stack-up for the antenna-integrated module (b) layout of the series-fed 1 × 8 proposed MPA array [38]

in order to avoid the degradation of the antenna performance. Silicon interposers are less popular at high frequencies because of its high dielectric constant. Glass is emerging as a substrate of choice for mm-wave interposers. This is due to its low surface roughness which can support fine feature sizes and its good mechanical properties. The different antenna structures based on glass interposers include the 1 × 8 series-fed MPA array [38], 4 × 4 parallel and series-fed MPA array [39], SIW-fed vivaldi antenna [40] and the quasi-yagi antenna [41]. Fig. 2.20 shows the stack-up design and the layout of the 1 × 8 MPA array described in [38]. The proposed interposer design allows for the compact integration of the die and the antenna array to achieve a gain of 11.6 dB in the 134 GHz - 141 GHz band. Several antennas based on other techniques such as micromachining [42], integrated passive device (IPD) process [43] and 3-D printed antennas [44] have also been reported. A summary of the various D-band antenna topologies reported and their associated fabrication technologies is shown in Table 2.1. These designs are compared in terms of their radiation performances and structural geometries for the realization of compact and integrated designs.

In designing D-band antennas, the design topology needs to address the good performance requirements of broad bandwidths, high gains as well as high efficiencies. Moreover, the antenna technology should be compatible with front-end circuitry for ease of integration. Metallic horn antennas offer excellent bandwidth and gain performance. However, they are bulky and cannot be readily integrated with other front-end modules. From the low-profile point of view, AoC and AiP package-based designs are attractive. However, the performance of these fully integrated antennas suffer from limited gains and low radiation efficiencies. Improved gain performances has been realized through the use of arrays. The extensive use of interconnections for array feed networks may also introduce additional losses. An efficient radiator such as the DRA is highly desirable at high frequencies. DRAs have been demonstrated to exhibit high efficiencies when implemented in AoC using CMOS technology [14] or when integrated in standard PCB and LTCC technologies [45], [46]. The designs presented in [45] and [46] are implemented in the millimeter-wave band at 60 GHz. These radiator designs may be downscaled to realize efficient antenna designs in the D-band and THz frequencies with the main task being the design of low-loss feeding network.

Table 2.1: Summary of the different antenna structures reported for D-band applications

| Ref. | Type | Technology | $f_0$,(GHz) | Bandwidth | Gain | Efficiency | Remarks |
|---|---|---|---|---|---|---|---|
| [12] | MPA | CNC Machine | 146 | 5.9% | 11.4 dBi | - | simple structure, low profile, narrow BW, high ohmic (metallic) and feed losses |
| [21] | MPA | LTCC | 166 | 12.5% | 16.8 dBi | - | Low profile, 4 × 4 array for high gain, narrow BW, metallic losses |
| [15] | ME dipole | LTCC | 159 | 12.8% | 19.3 dBi | - | Low profile, 4 × 4 array for high gain, narrow BW, metallic losses |
| [13] | SIW slot | PCB | 110–170 | 42.86% | 10.8 dBi | - | Simple structure, low profile, wide BW |
| [22] | CBS | LTCC | 146.6 & 167.2 | >3.89% | 8.73 dBi | - | Low profile, low gain, narrow BW |
| [11] | Horn | PCB | 129.5–156.5 | 18.9% | 15.46 dBi | - | Relatively high BW and gain, bulky |
| [25] | Horn | NM | 140-150 | - | 32 dB | - | High gain, high directivity, bulky |
| [26] | Horn | Machining | 130-175 | 29.5% | 32 dBi | - | Wide BW, high gain, bulky |
| [27] | Dielectric rod | NM | 135-145 | 7.14% | 19 dB | - | High gain, narrow BW, bulky |
| [28] | DRA | Wet etching | 176 | 5.78% | 12.24 dB | 82% | Low profile, narrow BW, low gain, high efficiency |
| [30] | MPA | AoC | 156-166 | 6.21% | 7 dBi | 60% | Ease of integration, narrow BW, low gain, low efficiency |
| [31] | Dipole | AoC | 160 | - | 6 dBi | 60% | Ease of integration, low gain, low efficiency |
| [14] | DRA | AoC | 135 | 7% | 7.5 dBi | 42% | Ease of integration, narrow BW, low gain, low efficiency |
| [32] | Slot | AoC | 140 | 7.14% | 4.9 dBi | 41% | Ease of integration, narrow BW, low gain, low efficiency |
| [33] | MPA | AiP | 131 | 15.2% | 6 dBi | - | Ease of integration, narrow BW, low gain |
| [34] | MPA | AiP | 122 | 4% | 9.9 dBi | 80% | Ease of integration, narrow BW, low gain, high efficiency |
| [35] | DRA | AiP | 154 | 33.9% | 5.5 dBi | 85% | Ease of integration, wide BW, low gain, high efficiency |
| [36] | MPA | AiP | 140 | 53% | 18.1 dBi | 80% | Ease of integration, wide BW, 4 × 4 for high gain, high efficiency |
| [37] | ME dipole | AiP | 150 | 15.9% | 14.1 dBi | - | Ease of integration, narrow BW, low gain |
| [38] | MPA | Glass sub | 138 | 5.1% | 11.6 dB | - | Ease of integration, narrow BW, low gain |

BW - impedance bandwidth, efficiency - radiation efficiency, NM - not mentioned

## 2.2 Antenna system-level performance specifications

Antennas are used in wireless communication systems to convert electrical signals to free-space electromagnetic waves and vice-versa in their transmitting and receiving modes respectively. The performance of these antennas may be described by various parameters. This section discusses some of the parameters and figures-of-merit used in the characterization of the performance of antennas such as the antenna radiation pattern, impedance bandwidth, antenna gain and radiation efficiency.

### 2.2.1 Antenna radiation pattern

The radiation pattern of an antenna is a graphical representation of the far-field radiation characteristics of the antenna as a function of the spherical spatial dimensions, $(\theta, \phi)$ [47]. This is usually given as amplitude patterns of the electric and magnetic fields. However, it is possible to have patterns of other radiation properties such as power, phase or polarization. The radiation patterns of antennas may be broadly categorized as:

(i) Isotropic pattern which radiate equally in all directions.

(ii) Directional pattern which radiate or receive electromagnetic energy more effectively in certain particular directions than in others.

(iii) Omnidirectional pattern which is characterized by a non-directional pattern in a certain plane and a directional pattern in an orthogonal plane.

Fig. 2.21 shows the illustration of omnidirectional and directional radiation patterns.

The antenna field pattern is obtained by evaluating the trace of the electric (or magnetic) field at constant radius from the center of the coordinate system, which gives rise to a three-dimensional field pattern distribution. However, the most important sectional views that contain the useful information needed are those that correspond to the principal E-plane ($\phi = 0^o$) and H-plane ($\phi = 90^o$). Therefore, it is common to represent the radiation performance in terms of two-dimensional normalized cartesian or polar plots of the E- and H-planes. The radiation patterns provide additional antenna parameters such as main lobe direction (MLD), beamwidth (BMW), sidelobe levels (SLLs) among others. In addition, information on the directive properties of the antenna can easily be obtained.

### 2.2.2 Antenna impedance bandwidth

The input impedance of an antenna is the impedance seen looking into the input terminals of an antenna. An antenna can be modelled by its Thevenin equivalent circuit, and its input impedance given by [47], [48]:

$$Z_{Ant} = R_{rad} + R_{loss} + jX_{Ant} \tag{2.1}$$

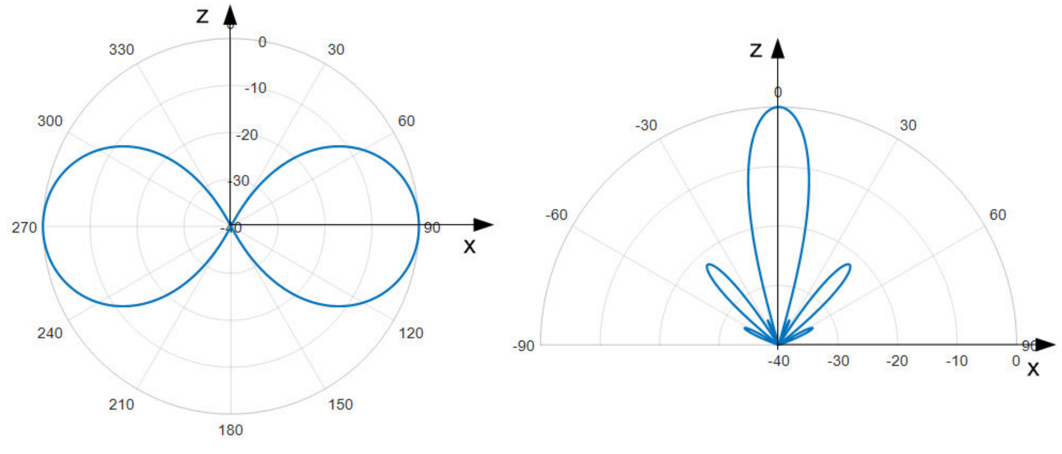

(a) (b)

Figure 2.21: Polar plots showing (a) omnidirectional and (b) directional radiation patterns showing the main lobe and the side lobes

$R_{rad}$ is the radiation resistance which represents the power scattered or radiated by the antenna, $R_{loss}$ is the loss resistance accounting for the conduction and dielectric losses and $X_{Ant}$ is the antenna reactance.

The input impedance and the antenna matching vary as a function of frequency. This means that the antenna will be matched to the transmission line within a certain frequency range. The frequency interval within which the input reflection coefficient is below -10 dB is referred to as the antenna impedance bandwidth or simply as antenna bandwidth. In this band, the antenna operates more efficiently. For relatively small bandwidths, the impedance bandwidth is often expressed as a percentage with respect to the center frequency $f_0$ as [48]:

$$BW = \frac{(f_u - f_l)}{f_0} \times 100\% \tag{2.2}$$

where $f_l$ and $f_u$ are the lower and upper boundaries of the antenna operating frequency, respectively.

### 2.2.3 Antenna directivity

The directivity of an antenna is defined as the ratio of the radiation intensity in a given direction to the average radiation intensity in all directions. This is given by [47]:

$$D = \frac{U(\theta, \phi)}{U_0} \tag{2.3}$$

$U(\theta, \phi)$ represents the radiation intensity in the $(\theta, \phi)$ direction and $U_0$ is the average radiation intensity. For total power radiated by an antenna $P_{rad}$, the average radiation intensity is given by [47]:

$$U_0 = \frac{P_{rad}}{4\pi} \tag{2.4}$$

The direction is always taken as that corresponding to maximum radiation intensity and the maximum radiation is obtained from [47]:

$$D_0 = 4\pi \frac{U_{max}}{P_{rad}} \tag{2.5}$$

$U_{max}$ = maximum $[U(\theta, \phi)]$

Equation (2.4) represents the radiation intensity of a hypothetical isotropic radiator. Equation (2.5) can be interpreted as a comparison of the maximum radiation intensity of an antenna to that of a reference isotropic radiator, and it provides a basis for the comparison of the directive properties of different antennas.

### 2.2.4 Antenna radiation efficiency

Antennas experience losses that may arise from reflections due to impedance mismatches and conductor and dielectric material losses. These losses cause the total input power not to be radiated. The total radiation efficiency accounts for all these different types of losses and is calculated from the total power radiated divided by the total power accepted at the input terminals of an antenna [47], [48]:

$$\eta = \frac{P_{rad}}{P_{in}} \tag{2.6}$$

$P_{in}$ is the total input power. Because of the losses, $\eta$ is always less than unity.

### 2.2.5 Antenna gain

Gain is the ratio of radiation intensity of an antenna in a given direction to that of a lossless isotropic antenna, for the same power input. The direction is always taken as that corresponding to maximum radiation intensity. This is expressed mathematically as [47]:

$$G = 4\pi \frac{U(\theta, \phi)}{P_{in}} \tag{2.7}$$

The gain and directivity of an antenna are closely related except that while the directivity is based on the radiated power, the gain is based on power input to the antenna and accounts for the antenna losses. The relationship between antenna gain and its directivity is given by [47]:

$$G = \eta D \tag{2.8}$$

## 2.3 Dielectric resonator antennas (DRAs)

DRAs are made from high-permittivity and low-loss dielectric materials. The typical values of the dielectric constant range between 10 and 100 [18]. The early works on DRs date back to 1939, whereby Richtmyer discovered that a high-permittivity block of dielectric material can radiate into free space [49]. However, the early applications of these DRs was in shielded microwave cavities where they were used to design filters and oscillators owing to their high Q-factor. It was not until 1983 when Long *et al* proposed a coaxial-fed cylindrical DRA (CDRA). In their investigations, they reported that a DRA is capable of radiating efficiently in the broadside direction [50]. In the last three decades, there has been an increased momentum in investigations on DRAs focusing on different applications, designs, performance improvements and optimization. These investigations have demonstrated that DRAs are efficient radiators with comparative advantages over the traditional low-gain antenna elements such as MPAs, monopoles and dipoles. DRs possess attractive physical and radiation characteristics such as small size, relatively wide bandwidth, high radiation efficiency and ease of excitation using the common transmission lines. Besides, different radiation characteristics can be obtained depending on the excited modes of the DR [18].

The radiation characteristics of a DRA is dependent on the internal field distributions of the excited modes. This means that the geometrical shape of the resonator and its feeding may be selected to obtain different radiation characteristics for various applications. Investigations show that a DRA of an arbitrary shape operating in its fundamental mode radiates like a magnetic dipole [51]. The higher-order modes radiate like magnetic multipoles such as quadrupoles, octupoles etc [18]. The magnetic fields of a rectangular DRA (RDRA) operating in its fundamental mode is illustrated in Fig. 2.22. DRs of various shapes have been investigated for utilization as antenna elements across different frequency bands. However, arbitrary and non-regular shaped DRs have the disadvantage that their radiation characteristics such as resonance frequency, Q-factor, bandwidth, radiation pattern etc. cannot be easily predicted. This renders such geometries less attractive in the design of DRAs. On the contrary, the radiation behaviour of some regular geometries can be determined without the use of a full-wave electromagnetic simulator. These shapes have been analyzed and the expressions for predicting their behaviour and radiation parameters developed. The formulations for the spherical DRAs, CDRAs and rectangular-shaped DRAs have been developed and are presented in [18]. In terms of analysis, the spherical DRA offers the simplest structure. It is the only shape for which analytic solution is possible, unlike the CDRAs and RDRAs where the solutions do not exist. However, approximate formulars have been developed based on empirical relations and approximate models. These expressions are fairly accurate in predicting the behaviour of these DRAs. This is useful in the simplification of the analysis and reduction of the design time.

The RDRA presents a better choice as an antenna when compared to the spherical

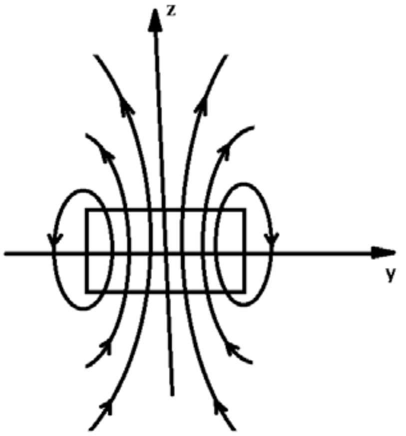

Figure 2.22: Magnetic field lines of an isolated rectangular DRA oriented along the $z-$ axis

and CDRAs. It offers the advantages of ease of fabrication as well as flexible design. There exists inherent degenerate modes in spherical and CDRAs owing to their structural symmetries [51]. These modes have an unwanted effect of increasing the level of cross-polarization and degradation of the antenna radiation pattern [52], [53]. The RDRA has a higher degree of free parameters. By proper choice of the aspect ratios (height-to-length and width-to-length ratios), the excitation of degenerate modes can be eliminated. The RDRA is versatile in terms of bandwidth control. The three dimensions of an RDRA may be independently selected to vary its aspect ratios. This has the effect of varying the radiation Q-factor of the resonator. The bandwidth of an RDRA is inversely related to the Q-factor. Consequently, the choice of the aspect ratios leads to flexible designs for the manipulation of the bandwidth.

### 2.3.1 Resonant modes of an RDRA

The practical design of an RDRA requires accurate computation of the DRs' resonant frequencies and the knowledge of the field pattern distributions inside the DR element. The latter is used to determine the modes excited by the DRA and to predict the far-field radiation pattern. Fig. 2.23 (a) shows an analytic model of an isolated DR. A rectangular DR element of a high permittivity, $\epsilon_{rd}$ is placed at the origin of the coordinate system. The dimensional parameters of the RDRA are $W_{dra}$, $L_{dra}$ and $2H_{dra}$ in the $x$-, $y$- and $z$-directions respectively. The wall boundaries may be assumed to be perfect electric conductors (PECs) and perfect magnetic conductors (PMCs). These boundaries are defined by the following boundary conditions:

For PEC walls,

$$\hat{\mathbf{n}} \times \mathbf{E} = 0 \tag{2.9}$$

$$\hat{\mathbf{n}} \cdot \mathbf{H} = 0 \tag{2.10}$$

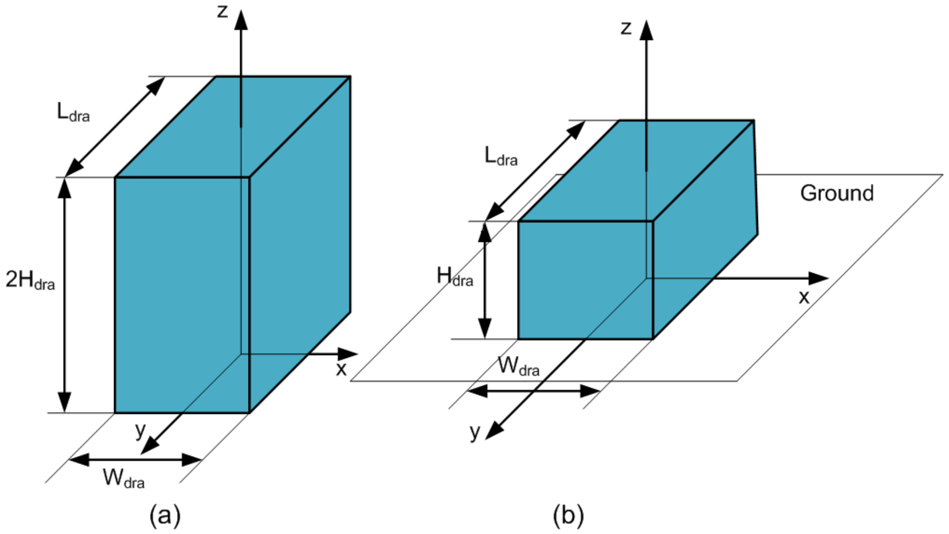

Figure 2.23: Geometry for the DRA model (a) isolated DR element and (b) equivalent DR on an infinite ground plane

For PMC walls,

$$\hat{\mathbf{n}} \times \mathbf{H} = 0 \tag{2.11}$$

$$\hat{\mathbf{n}} \cdot \mathbf{E} = 0 \tag{2.12}$$

The conventional dielectric waveguide model (DWM) is used to determine the expressions of the fields inside the DR. This formular assumes that an isolated DR is a truncation of an infinite dielectric waveguide. The fields can be approximated from the electric vector potential and the boundary conditions for the DWM [54]. The rectangular DR can support only transverse electric (TE) and transverse magnetic (TM) modes. From Van Bladel's asymptotic theory, the modes of an isolated rectangular DR are of *nonconfined* type [52]. These modes satisfy only one of the magnetic wall conditions $\hat{\mathbf{n}} \cdot \mathbf{E} = 0$ at all boundaries, while the condition, $\hat{\mathbf{n}} \times \mathbf{H} = 0$ is not necessarily satisfied. Therefore, DR boundary walls assumes perfect magnetic walls at $x = \pm W_{dra}/2$ and $y = \pm L_{dra}/2$. The tangential fields are continuous at the imperfect magnetic boundaries, at $z = \pm H_{dra}$. This is referred to as the magnetic wall model (MWM). TM modes do not satisfy the boundary conditions of the MWM. Therefore, the existence of TM modes cannot be confirmed [55]. Thus an isolated rectangular DR radiates like a magnetic dipole. The lowest order modes are given as $TE^x_{111}$, $TE^y_{111}$ and $TE^z_{111}$. These modes radiate like $x$-, $y$- and $z$-directed magnetic dipoles respectively. The mode subscripts refer to the number of half-wave field variations in the three orthogonal directions. By proper selection of the DR dimensions and its aspect ratios, higher-order modes can be excited, alongside the fundamental modes [56]. When mounted on a ground plane, the modes are expressed as $TE^x_{\delta np}$ or $TE^y_{m\delta p}$; $(1 < \delta < 1)$ depending on the orientation of the equivalent magnetic dipole. $m$,$n$ and $p$ represent the mode indicies. Throughout this text, these modes are simply denoted $TE_{\delta np}$ or $TE_{m\delta p}$.

When utilized as an antenna element, the DR is often placed above some metal ground plane. The image theory may be used to replace this isolated DR with a grounded DR of half its size in the $z$-direction. An infinite sheet of a PEC is placed in the $x-y$ plane at $z=0$, with the DR element height reduced by half, $H_{dra}$. The fields of the grounded DR and those of the isolated DR in the upper half-space are similar. The effects of the finite ground plane on the field distribution inside the DR is be assumed to be negligible. This allows for the approximation of the infinite sheet of PEC ground plane using a finite-size ground conductor. This is depicted in Fig. 2.23 (b) above.

Within the DRA, the field components associated with the various modes may be approximated from the expressions given in [57].

$$E_x = 0 \tag{2.13}$$

$$E_y = Ak_z cos\left(k_x x\right) sin\left(k_y y\right) sin\left(k_z z\right) \tag{2.14}$$

$$E_z = Ak_y cos\left(k_x x\right) cos\left(k_y y\right) cos\left(k_z z\right) \tag{2.15}$$

$$H_x = A\frac{k_y^2+k_z^2}{j\omega\mu_0} cos\left(k_x x\right) sin\left(k_y y\right) cos\left(k_z z\right) \tag{2.16}$$

$$H_y = -A\frac{k_x k_y}{j\omega\mu_0} sin\left(k_x x\right) cos\left(k_y y\right) cos\left(k_z z\right) \tag{2.17}$$

$$H_z = A\frac{k_x k_z}{j\omega\mu_0} sin\left(k_x x\right) sin\left(k_y y\right) sin\left(k_z z\right) \tag{2.18}$$

where $A$ is an arbitrary constant and the wavenumbers $k_x$, $k_y$ and $k_z$ represent the half-wave field variations in the different directions. The equation for the wavenumber $k_x$ is formulated from the DWM as:

$$k_x \tan\left(\frac{k_x L_{dra}}{2}\right) = \sqrt{\left(\epsilon_{rd}-1\right) k_{0,mn}^2 - k_x^2} \tag{2.19}$$

The wavenumbers in the $y$- and $z$-directions are given by:

$$k_y = \frac{m\pi}{W_{dra}} \tag{2.20}$$

$$k_z = \frac{n\pi}{2H_{dra}} \tag{2.21}$$

These wavenumbers must satisfy the separation equation:

$$k_x^2 + k_y^2 + k_z^2 = \epsilon_{rd} k_{0,mn}^2 \tag{2.22}$$

The transcendental equation in (2.19) is solved to determine the resonant frequencies $f_{0,mn}$ for $TE_{\delta mn}$ modes using equation (2.23):

$$k_{0,mn} = \frac{2\pi f_{0,mn}}{c} \tag{2.23}$$

$c$ denotes the speed of light and $k_{0,mn}$ the free space wavenumber corresponding to the resonant frequency $f_{0,mn}$. The theoretical resonant frequency obtained from this DWM model is very close to the experimental value obtained from experiment [58].

The radiated field patterns in the far-field region is determined from the knowledge of the field distribution of the DR [59]. The equivalent current densities $\vec{J}_s$ and $\vec{M}_s$ are determined from these field distributions through the application of Huygens' field equivalence principle [47]. The radiation patterns of RDRAs operating in both fundamental and higher-order modes have been investigated both using theoretical formulation and experimentation. Two major approaches in open literature on the theoretical prediction of the radiation pattern are the use of magnetic dipole models and the equivalence principle. It is well known the magnetic field of an isolated DR in its dominant mode is similar to that of a magnetic dipole. This knowledge has been extended in [60] to approximate higher-order modes using a set of short magnetic dipoles. The DR is modelled using an array of magnetic dipoles separated by a short distance of approximately $0.4\lambda$. The number of the array elements depend on the mode to be excited. Experimental verification was carried out to verify the radiation model. The predicted and measured data were similar, showing a broadside radiation characteristics. Similar patterns were obtained from the closed-form expressions reported in [61]. The researchers formulate the approximate solution of the eigenfunction of higher-order modes, and the closed-form expressions for the far-field radiation pattern formulated using the equivalence principle. The measured and simulated data showed good agreement, showing consistent broadside patterns.

The DR element is often mounted on top of a conducting metal plane, for mechanical support as well as to provide a grounding plane. This ground plane has the effect that the even modes of the DR are extinguished in the $z-$direction. Therefore, only the $TE_{\delta np}$ and $TE_{m\delta p}$ ($p$=odd) modes exist. The excited modes may be identified by observing the field patterns of the DR at the resonant frequencies. The particular modes excited are determined from the number of half-wave variations in the $E-$ and $H-$fields along the different directions. Fig. 2.24 shows the illustration for the electric field distributions for $TE_{\delta 11}$, $TE_{\delta 21}$, $TE_{\delta 31}$ and $TE_{\delta 13}$ modes.

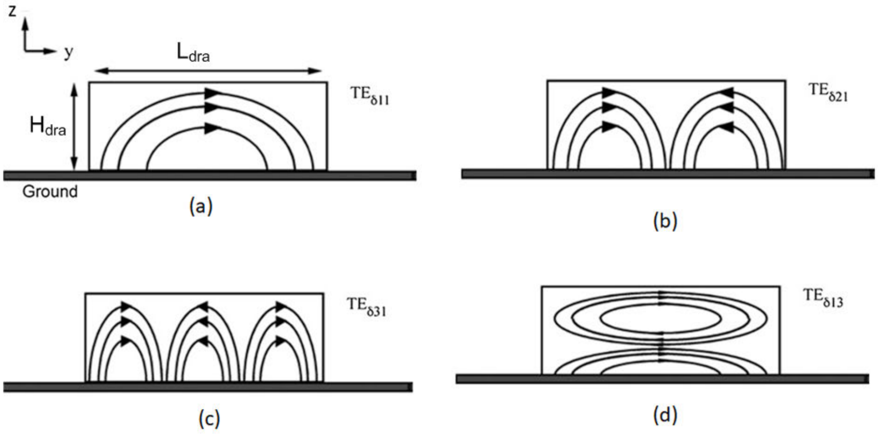

Figure 2.24: Electric field distribution patterns for (a) $TE_{\delta 11}$ (b) $TE_{\delta 21}$, (c) $TE_{\delta 31}$ and (d) $TE_{\delta 13}$ modes.

### 2.3.2 Feeding techniques

DRAs are easily coupled to different feed mechanisms. The energy from the transmission line needs to be coupled to the DR efficiently. The different feeding arrangements include coaxial probes, open microstrip lines, coplanar waveguide feed [62], aperture-coupled feeds, conformal metal strips [63], among other waveguiding structures. Different modes of the DR may be excited depending on the feeding arrangement used as well as the position of the excitation. The use of coaxial probes have been proposed and investigated. Impedance matching is achieved by varying the length of the probe and its position inside the DR element. The disadvantage associated with the coaxial probe feeding is that the DR must be drilled so that the probe can penetrate. Precision drilling is required so as to minimize the airgap around the probe. This airgap has the undesirable effect of shifting the resonance frequency to introduce impedance mismatches [64].

The microstrip line is a planar feeding network that is commonly used to excite the DRA. It has the advantage that it is easy to design and fabricate, which allows for the direct integration of the antenna with microwave circuits. An open microstrip is often placed underneath or in close proximity to the DR so as to excite the desired modes. However, owing to this feedline not being isolated from the radiating element, the radiation performance of the DRA may be significantly degraded. A microstrip line may also be used in conjunction with an aperture feed, whereby, it is positioned below the ground plane, for better radiation performance. The challenge associated with coaxial and microstrip feeds is the increased transmission losses associated with the feeding network. These affect the antenna gain and radiation efficiency.

Aperture-coupled feeds are desirable because this isolation is achieved by the use of the ground plane. This reduces the effects of spurious radiation associated with the feed network. The slot and the DRA have similar radiation patterns because they both radiate like magnetic dipoles. This means that the resonant modes of the slot and the DRA may be coupled for more bandwidth. Consequently, there is minimization of the undesirable effects of cross-polarized fields [53], [54].

As mentioned, the different modes are defined by the unique internal field distributions. These field patterns are used to identify the modes that are excited at any given resonance frequency. This knowledge of the electric and magnetic field patterns is also very important in choosing the proper excitation arrangements. The electric current probe couple to the electric field lines, while narrow apertures behave as magnetic current sources and couple to the magnetic field lines. For strong coupling to the required mode, these probes or the slot must be located along the field lines where the field strength is greatest [65].

Rectangular waveguides have much lower conduction loss. However, they are not compatible with MMIC technology for integration with other planar devices. The SIW is a planar waveguide, which offers the advantage of ease of integration with other devices using PCB technologies. It presents a better choice for feeding the DRA owing to its low leakage and high isolation properties as compared with microstrip lines and coplanar waveguides.

### 2.3.3 Bandwidth improvement of DRAs

One major limitation associated with the DRA is the narrow impedance bandwidth. The bandwidth performance of the DRA is dependent upon its geometry, permittivity of the DR material and the feeding arrangements. A high permittivity provides the much desired miniaturization. However, it leads to a narrow bandwidth. The typical bandwidth of an RDRA is about 6–10%. By using a low-permittivity dielectric material, this bandwidth can be increased beyond 10%. This achievement comes with an increase in the overall size of the DR [66]. For a given application, a trade-off between these two key design parameters has to be made. Several bandwidth enhancement techniques exist in open literature. These can generally be classified into those involving the modification of the DR element, application of different feeding techniques, incorporation of additional structures and the excitation of higher-order modes for multimode operation.

#### 2.3.3.1 Modification of the DR element

The choice of the aspect ratios is significant in the determination of the bandwidth performance of an RDRA. DRs with large aspect ratios have been employed to reduce the Q-factor so as to obtain wider impedance bandwidths [59]. The use of different resonator geometries, such as conical, triangular, H-shape, inverted frustrum etc. have also been reported for bandwidth enhancement. By modifying the shape of the DR, the electric fields inside the DR may be controlled to achieve some bandwidth control. Other modifications involve the reshaping the resonator by way of removal of DR parts to create complex shapes or cause reduction in the volume to surface area ratio in the radiating structure. These include the carving out of a notch, well or slots, drilling of holes, multi-segment DRs, use of fractal geometries among other perforation designs. These techniques involve the introduction of structural discontinuities within the DR to create airgaps, leading to reduced effective permittivity of the resonator. They have the effect of lowering the Q-factor for bandwidth improvement. In addition, the discontinuities cause perturbation of the fields within the DR, leading to the effective radiation of the antenna. Slots and grooves may also be introduced in the DR to create an airgap between the ground plane (feeding slot) and the DR element. Bandwidth broadening is achieved by adjusting the coupling between the DR and the feeding structure through the variation of the thickness of this airgap.

#### 2.3.3.2 Use of different feed arrangements

The various feeding mechanisms for DRA excitations have been discussed in section 2.3.2 above. Different modes may be excited through the modification of these aforementioned feeding arrangements. One such possible arrangement is placing the coaxial probe adjacent to the DR element, instead of embedding it. However, this leads to reduced coupling, which affects the radiation characteristics of the antenna [67]. Modification of the feed line through the addition of parasitic stubs has been reported for performance enhancement [68]. Further improvement in impedance matching may be achieved through the modification of the coupling slots such as cross-slot feed [69], Meander slots [70], twin-apertures [71], arc shaped-apertures [72], multi-layered substrates [73] etc. Another feeding technique includes the differential feeding. In this arrangement, two microstrip lines with differential signals are used to excite the DRA so as to excite the desired mode [74].

#### 2.3.3.3 Incorporation of additional structures

The use of composite radiating structures significantly broadens the bandwidth of the DRA. These composite structures are formed through the integration of additional elements with the antenna. The additional structures are designed to induce additional resonance in the overall composite antenna. In its simplest form, the additional elements may take the form of parasitic elements. Hybrid designs involving the incorporation of other radiating structures such as the MPAs, monopoles, slot antennas [62], [75], [76] have been reported. Each radiator is designed to radiate in its own band, and may be individually tuned for wideband or multiband frequency response. The stacking of different DRAs of similar or dissimilar dielectric material and geometries have also been designed for different applications. Superstrates and other techniques commonly employed in MPAs, such as electronic bandgap structures, metasurfaces [77] and frequency selective surfaces have also been used in the design of wideband DRAs. Other approaches involve use of metallic loadings and coatings of other materials such as graphene etc. The limitation associated with this approach is the increase in the overall size and complexity. Besides, the induced resonances may make it difficult to tune the antenna.

#### 2.3.3.4 Excitation of higher-order modes (HOMs)

The modes of the DRA that can be excited depend on the feeding source and position as well as choice of aspect ratio of the radiator [53]. For a single-mode operation, the bandwidth performance of a DRA is often less that 10%, which is not sufficient for broadband applications [78]. A DR element can be designed to excite two or more modes simultaneously so as to exhibit multiple resonances. If these resonances associated with the fundamental/dominant and higher-order modes are close enough, adjacent bands can be merged to achieve wideband or multiband operation. An important requirement is that the radiation patterns of the individual modes to be merged should be similar. This aims at minimizing the effects of cross-polarized fields and distortion so as to ensure good antenna performance over the bandwidth of operation [79].

Designs based on combination of two or several techniques have also been proposed. A low-profile and broadband antenna is proposed in [80] for applications in the sub-6 GHz spectrum. The authors propose the use of two slots to excite the higher-order modes in an

RDRA. Different air regions are introduced in the RDRA structure to merge the multiple modes for bandwidth enhancement. The design achieves a bandwidth of 64%.

### 2.3.4 DRA gain enhancement

To effectively support the transmission of high data rates, an antenna must guarantee wide bandwidths and high gains. Different design methods have been proposed for gain enhancement of DRAs. One effective way to realize a high-gain antenna is to use of antenna arrays. These arrays usually require designs of power dividers. The extensive use of these power divider networks may increase the complexity and introduce losses in the feed network [81]. Some of the techniques employed for bandwidth enhancement may simultaneously be applied to enhance the gain of a DRA. This means that the DRA may achieve either enhanced gain, increased bandwidth or both depending on the design. Incorporation of horns, cavities, parasitic elements, superstrates among other structures have been proposed. The use of a surface-mounted short horn has been proposed in [82] to achieve a gain of 9 dBi, with improved side lobe levels. A hybrid DRA is presented in [83], for application in the 60 GHz frequency range. The gain of the antenna is enhanced by surrounding the antenna with a metallic dented cavity to achieve a high gain of 16.5 dB. SIW-backed cavities have also demonstrated higher antenna gains, and has been applied in [84] to achieve a peak gain of 11.3 dBi. Other techniques applicable for bandwidth and gain enhancement include stacking [85], excitation of higher-order modes [60], [86], incorporation of printed of electromagnetic bandgap (EBG) surfaces [87], use of metamaterial and frequency selective surface (FSS) superstrates [88], [89], parasitic DR elements [90] amongst other techniques.

## 2.4 Substrate integrated waveguides (SIW)

At high frequencies, the application of the classical metallic waveguide in the interconnection of planar circuit components is limited by its weight and volume. Planar interconnects made from the patch fabrication processes become attractive for the connection and integration of planar circuits. The conventional planar transmission lines such as the microstrip line, strip line or coplanar waveguide suffer from high loss, significant cross-talk and limited power handling capacity. The SIW which is also referred to as post-wall waveguide or laminated waveguide, is a low-loss waveguide that can be realized on a planar structure using PCB, LTCC or other planar fabrication processes. The SIW is synthesized by embedding two rows of metal vias (posts) on a dielectric laminate to form a dielectric-filled waveguide. Fig. 2.25 illustrates the configuration of the SIW. The two rows of vias form the lateral walls of the guide, which confine the fields in the lateral direction while the top and bottom conductors confine the fields in the vertical direction. One advantage of the SIW is that it can be fabricated alongside other circuit components for high-density integration.

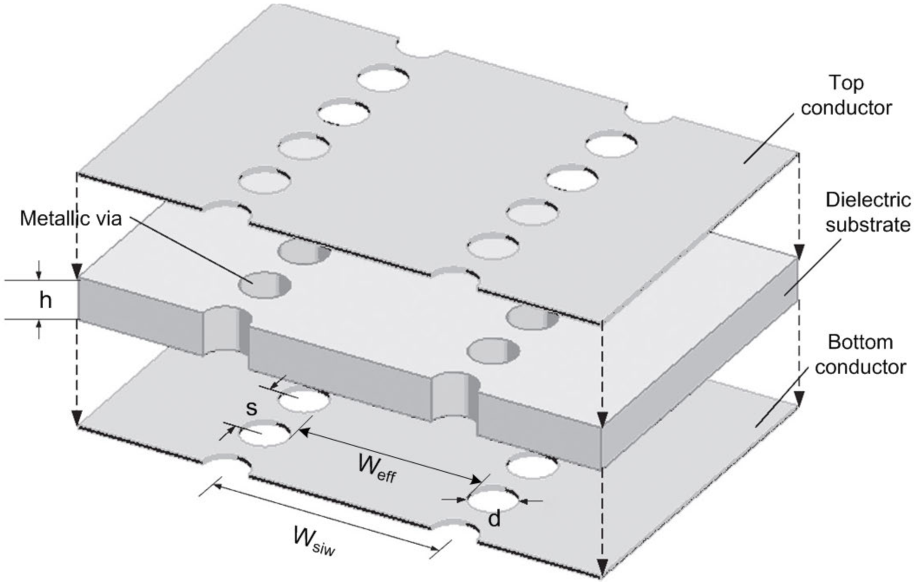

Figure 2.25: Configuration of the SIW

The spacing between the rows of via, $W_{siw}$, the diameter of the via holes, $d$ and the via pitch, $s$ are the critical parameters necessary for the design of the SIW. The pitch should be kept small enough to minimize the leakage losses along the walls of the guides. In designing the SIW, the following rules should be observed to keep the radiation loss at a minimum level and to avoid the bandgap effect [91]:

$$s \leq 2d \tag{2.24}$$

$$d \leq \lambda_g/5 \tag{2.25}$$

where $\lambda_g$ is the guided wavelength. These two rules are sufficient, but not always necessary. A properly designed SIW exhibits propagation behaviour similar to that of a conventional RWG. The SIW structure supports the propagation of $TE_{m0}$ modes ($m$, integer). This is because longitudinal lateral currents cannot flow because of the gaps created by the separation of the via. The cut-off frequency for the $(m, n)$ propagating modes in a rectangular waveguide of sides $a$ and $b$, $(a > b)$, filled with a material of permittivity $\epsilon_r$ is given by [92]:

$$f_{c,mn} = \frac{c}{2\sqrt{\epsilon_r}}\sqrt{\left(\frac{m}{a}\right)^2 + \left(\frac{n}{b}\right)^2} \tag{2.26}$$

The via-to-via dimensions of the SIW is obtained by mapping the dimensions of the RWG to achieve the lowest cut-off frequency for the lowest $TE_{10}$ mode, given by:

$$f_{c,10} = \frac{c}{2\sqrt{\epsilon_r}W_{eff}} \tag{2.27}$$

The effective width of the SIW, $W_{eff}$ is determined from the empirical relation given

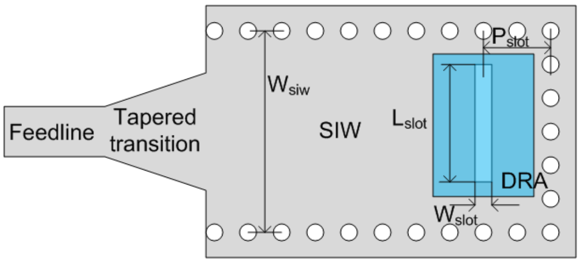

Figure 2.26: Layout of the SIW-fed RDRA

in [93]:

$$W_{eff} = W_{siw} - 1.08\frac{d^2}{s} + 0.1\frac{d^2}{W_{siw}} \tag{2.28}$$

An alternative empirical equation based on the method of lines (MOL), for the determination of the effective width of the SIW is presented in [94].

The SIW can easily be connected together with other planar circuits using simple transitions such as microstrip-to-SIW or coplanar-to-SIW transitions. These transitions act as impedance matching networks and also allow for wideband excitation of the SIW. The SIW is shorted at one end by a row of transverse via to form the feed cavity for the DRA. Energy from the feed cavity is coupled to the DR element through longitudinal or transverse slots on the top surface of SIW. The layout of a single element RDRA excited by a SIW through a rectangular slot is depicted in Fig. 2.26.

The slot dimensions, $L_{slot}$ and $W_{slot}$ together with its position, $P_{slot}$, control the excitation and amount of power coupled to the DR. For maximum coupling, the slot should be located at the peaks of the standing waves of the electromagnetic fields inside the cavity.

The design rules presented in equations (2.24) and (2.25) are based on the dominant $TE_{10}$ mode of the SIW. As the frequencies increase into the mm-wave and THz frequencies, scaling up the designs at lower frequencies inevitably encounters difficulties due to limitations in the fabrication processes [95]. One possible solution is the reduction of the number of vias while ensuring that the SIW performance is not degraded. The utilization of higher-order SIW modes has been investigated for various antenna designs and excitations. Higher-order mode excitations lead to the realization of a simplified SIW structure by way of reduced number of metal vias, with the advantage of reduced metallic losses and relaxed fabrication tolerance [96].

## 2.5 MIMO antennas

Multiple-input multiple-output (MIMO) systems enable transmission of data over multiple channel paths. This means that the transmitter employs multiple antennas to transmit multiple information signals in the same frequency band at the same time. Multiple antennas are used to detect the correlated signals, which undergo processing in the receiver to separate the different transmitted data streams, a diversity scheme that is used to combat the effects of multipath fading [97]. There is need for cellular communication equipment with enhanced data throughput, increased channel capacity and improved reliability [98]. To fulfill these requirements, MIMO antennas have found applications in modern wireless communication systems [99]. Technological advancements have led to the shrinking in the size of communication equipment thus posing challenges to the embedding and integration of antenna elements in limited space for MIMO applications. When antenna elements are closely spaced, they may be tightly coupled to each other leading to low isolation and reduced radiation efficiency. Decoupling structures together with diversity techniques have been employed to reduce the mutual coupling and improve the low level of isolation between the elements to minimize the degradation of the performance of the antenna [100]. The challenge in the design of MIMO antenna systems lies in the minimization of the overall MIMO antenna size as well as achieving high isolation between the antenna elements. The mutual reduction technique employed should not introduce impedance mismatches in the antenna elements. Moreover, compact antenna designs are desirable for ease of integration.

### 2.5.1 Concepts of MIMO technology

As mentioned above, MIMO systems employ multiple transmit and receive antennas to combat the effects of multipath fading to enhance spectral efficiency in wireless communication systems. Fig. 2.27 shows a block diagram of a MIMO system comprising of N transmit and M receive antennas. It is possible to transmit multiple data streams in parallel simultaneously over the same channel. The transmitted electromagnetic waves reach the receiving antennas through different propagation paths as directly transmitted waves as well as those due to reflection, scattering, refraction or diffraction by obstructing structures. At the receiver, each of the antenna receives the energy from all transmitted waves. The spatial nature of the channel may be exploited through the use of diversity and beamforming techniques to increase the spectral efficiency [101], to enable high-speed data transmission for future generations wireless networks.

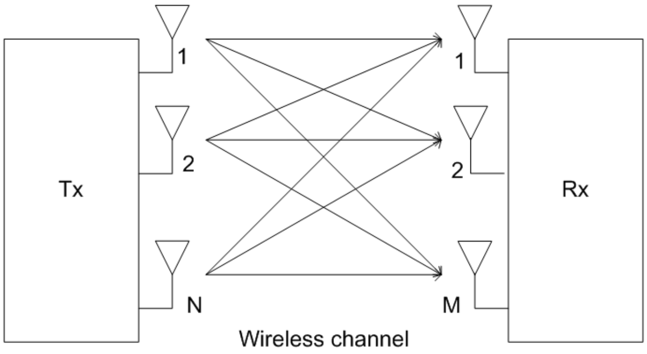

Figure 2.27: Block diagram of a MIMO system

There exists NM propagation paths between the N transmit and M receive antennas.

the discrete-time data model for a MIMO system can be expressed as [102]:

$$\mathbf{r} = \mathbf{H}\mathbf{u} + \mathbf{n} \tag{2.29}$$

$\mathbf{r} = [r_1, r_2, \cdots, r_M]^T$ is the received signal vector, $\mathbf{u} = [u_1, u_2, \cdots, u_N]^T$ is the transmitted signal vector, $\mathbf{n}$ is the M-dimensional additive Gaussian noise vector and the channel is described by the matrix [101].

$$\mathbf{H} = \begin{bmatrix} h_{11} & h_{12} & \cdots & h_{1N} \\ h_{21} & h_{22} & \cdots & h_{2N} \\ \vdots & \vdots & \ddots & \vdots \\ h_{M1} & h_{M2} & \cdots & h_{MN} \end{bmatrix} \tag{2.30}$$

The complex gains of the channel between the $j^{th}$ transmit antenna and the $i^{th}$ receive antenna are given by the elements of the matrix $h_{ij}$. Each transmit-antenna transmits a distinct data stream, leading to an increase in the link capacity provided that the propagation paths are independent of each other (spatially uncorrelated channels). The low correlation is achieved by the use of spatial, pattern or polarization diversity techniques.

### 2.5.2 Mutual coupling reduction in MIMO antennas

An increase in the number of antenna elements leads to an increase in the level of mutual coupling between the antenna elements due to the effects of electromagnetic interaction between them. This poses challenges in the design of MIMO antennas in portable communication equipment with limited physical space. A number of mutual coupling reduction techniques and decoupling structures have been reported. These techniques include the following [103], [104].

(i) Metamaterial structures such as electromagnetic bandgap structures, frequency selective surfaces, complementary split-ring resonators etc, which minimize the interference between the radiators.

(ii) Defected ground structures – Incorporation of different shapes of defects and slots on the ground plane (such as arc, rectangular, T-shape etc) for mutual coupling suppression

(iii) Slots on the radiating elements

(iv) Stub elements on the ground plane

(v) A neutralization line may be introduced between the antenna elements to counteract the inherent coupling in the radiating elements

(vii) Parasitic elements

(x) Polarization diversity

Some of these decoupling methods may not be suitable for SIW-DRAs and other antenna structures.

### 2.5.3 MIMO antennas for mm-wave communications

In this section, we review some of the different antenna structures proposed for MIMO applications. There exist vast amounts of literature reporting on low-frequency MIMO antenna designs for mutual coupling reduction. The recent past has seen an increase in research interests in antenna designs for wireless communications at higher frequencies. This is evident in the number of research publications emerging in the frequency ranges beyond 5G. Therefore, this section only considers MIMO designs proposed for mm-wave and sub-terahertz frequencies.

A co-planar waveguide fed MPA is proposed for application in the 60 GHz frequency regime in [105]. A rectangular stub is inserted at $45^o$ between two orthogonally placed radiators for isolation enhancement as shown in Fig. 2.28. The rectangular stub which is placed on the ground plane extends the effective current route, thereby enhancing isolation. The bandwidth performance of the proposed design is 7.6 GHz (54.5 GHz – 63.1 GHz), with an isolation $S_{21} <$ -15 dB in the entire band of operation. The use of a neutralization line is reported in [106] for mutual coupling reduction in a MPA operating between 20 GHz and 80 GHz. This technique has been extensively employed in low-frequency MIMO antennas and requires connecting a structure between the radiating elements to introduce a coupling cancellation path. Fig. 2.29 shows the geometry of two L-shaped patches printed on a substrate and oriented at $180^o$ with respect to each other with a neutralization line placed in between. Besides the mutual coupling reduction, the neutralization line is reported to enhance the fractional bandwidth of the antenna. The proposed design exhibits a bandwidth of 12.3% (57 GHz – 64 GHz) and -15 dB coupling between the elements. Another MPA based MIMO antenna has been reported by Singh *et al* in [107]. The authors propose the use of circular slots/ holes on the radiating elements together with defected ground structures (DGS) for bandwidth and isolation improvements of a $2 \times 2$ MIMO configuration shown in Fig. 2.30. An impedance bandwidth of 13.14% (60.4 GHz– 68.9 GHz) and isolation less than -15 dB is achieved. The use of artificial magnetic conductors (AMC) metamaterials have also been investigated for the enhancement of isolation performance in MPA based MIMO antennas. The researchers in [108] propose a quad-port linearly arranged elements, incorporating a high impedance surface AMC for 60 GHz mm-wave applications. The structure of the proposed MIMO antenna is depicted in Fig. 2.31, showing an AMC background reflector for gain and front-to-back ratio improvement. The AMC background has the multiple effects of improved gain, increased front-to-back ratio and an isolation below -20 dB across the antenna operating bandwidth range (59.3 to 63.6 GHz).

DRAs are increasingly gaining popularity in mm-wave and THz frequency applications.

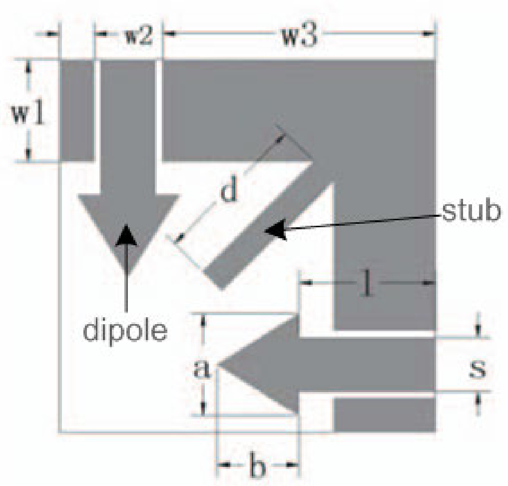

Figure 2.28: Configuration of the proposed 2 × 2 MIMO antenna with a rectangular stub for isolation enhancement [105]

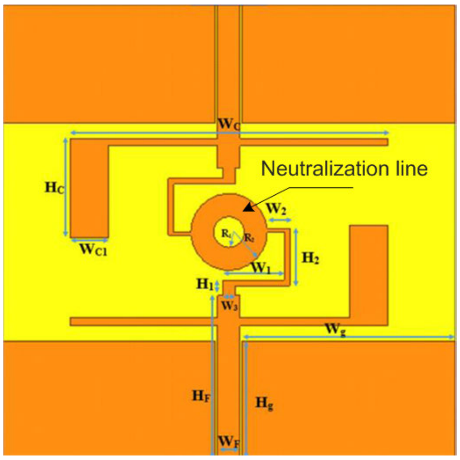

Figure 2.29: Configuration of the proposed 2 × 2 MIMO antenna using a neutralization line [106]

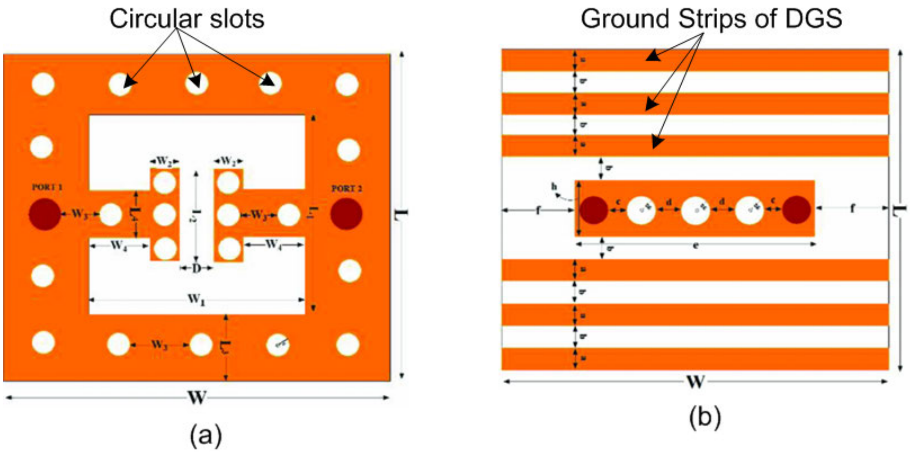

Figure 2.30: Geometry of the proposed MIMO antenna with patch holes and DGS (a) antenna top view and (b) bottom view [107]

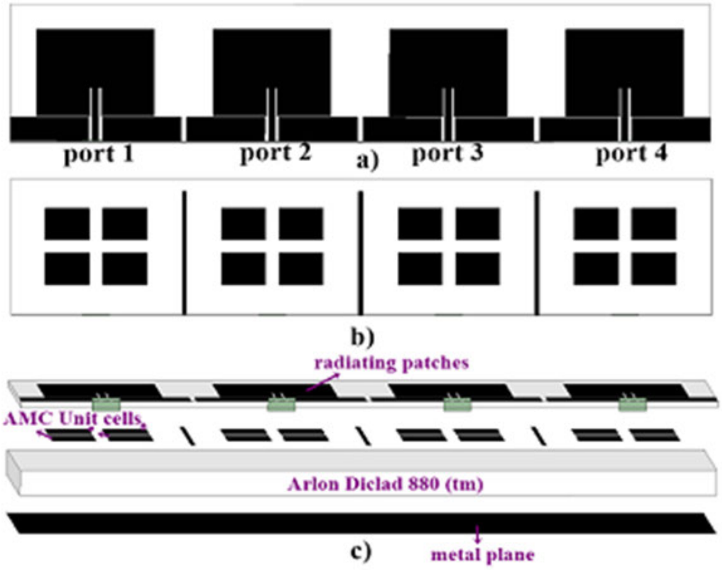

Figure 2.31: (a) Geometry of the quad-linearly arranged antenna elements (b) AMC configuration and (c) Quad-port MIMO antenna employing AMC [108]

These have been used in conjunction with metamaterial (MTM) structures in the design of high-isolation MIMO antennas at mm-wave frequencies. A FSS wall has been proposed for the minimization of spatial radiation fields between two DRA MIMO elements in [109] as depicted in Fig. 2.32. The FSS structure is designed to exhibit bandstop characteristics in the entire band of operation. The authors propose the use of a FSS structure in conjunction with etching of DGS slots on the common ground to achieve an isolation of -30 dB in the 57 GHz – 64 GHz band. Similar technique involving the use of metasurface shields has been applied in [110] to achieve -30 dB isolation between 56.6 GHz and 64.8 GHz frequencies (Fig. 2.33). A metasurface wall can rotate the polarization state of an electromagnetic wave after reflecting or transmitting it through. In this state, the metasurface behaves as a polarization-rotator wall. Metamaterial polarization-rotator (MTMPR) walls have been proposed in [111] to reduce the mutual coupling in a 2 × 2 DRA MIMO antenna. Fig. 2.34 shows the layout of the proposed DRA MIMO antenna operating in the 56 GHz – 65 GHz frequency band. MTM based superstrate structures have also been applied to enhance isolation, without degradation of the radiation pattern. Hagras *et al* [112] proposed a 2 × 2 microstrip fed MIMO DRA for application between 57 GHz – 65 GHz. Fig. 2.35 shows the structure of the proposed antenna. Isolation is achieved through the use of a metallic superstate in combination with ground slot.

At high frequencies, open microstrip feeds suffer increased radiation loss. Waveguide-based feeds can confine the electromagnetic fields to minimize these effects. A microstrip ridge gap waveguide (MRWG)-fed magneto-electric (ME) dipole antenna is proposed in [113] for 4 × 4 MIMO applications. Fig. 2.36 (a) shows the structure of the MRWG fed ME dipole antenna composed of a 2 × 2 array as a single element. The elements are rotated $90^o$ with respect to each other to form a 4 × 4 MIMO configuration shown in Fig. 2.36 (b) so as to achieve orthogonal polarization. The reported impedance bandwidth ranges

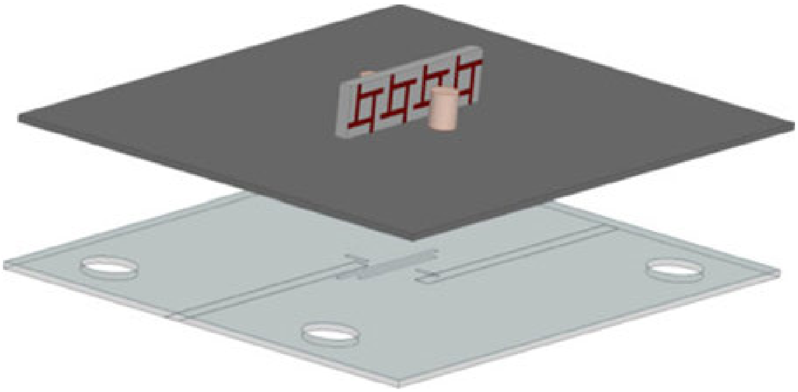

Figure 2.32: Configuration of the proposed MIMO antenna with a FSS wall [109]

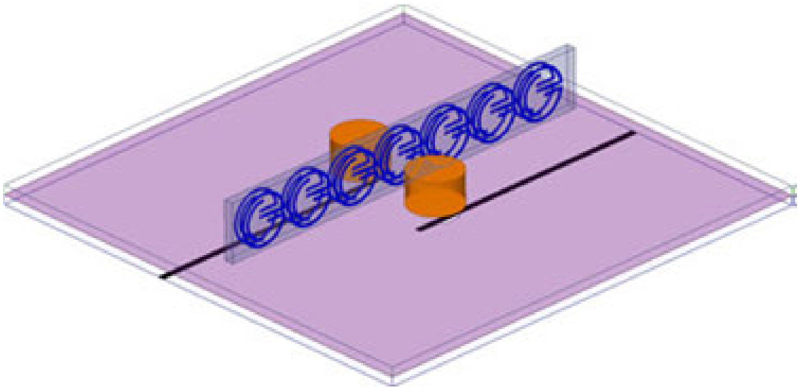

Figure 2.33: Illustration of the isolation improvement in DRA MIMO using MTM-based SRR [110]

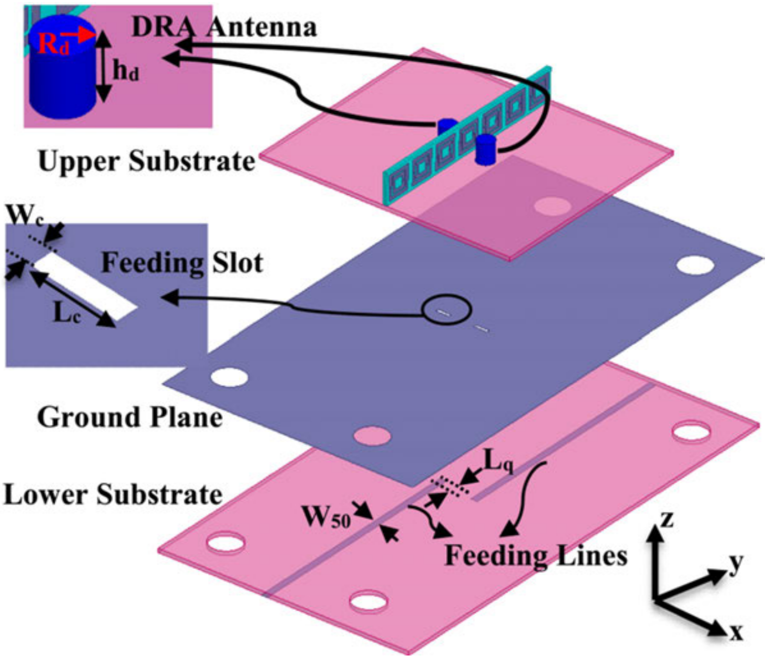

Figure 2.34: Layout of the 2 × 2 DRA MIMO antenna with the MTMPR wall proposed in [111]

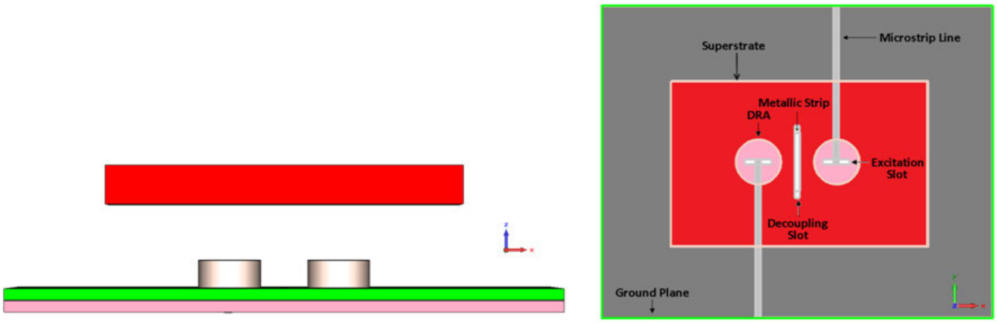

(a) (b)

Figure 2.35: Layout of the reduction of mutual coupling in MIMO antennas using MTM superstrate (a) front view and (b) top view [112]

from 51 GHz – 71 GHz, with an isolation of -30 dB. A 2 × 2 MIMO slot antenna based on a SIW is proposed for Q-band applications in [114]. Spatial and orthogonal polarization is applied to enhance isolation. The configuration of the proposed MIMO antenna is depicted in Fig. 2.37. The proposed design achieves a -10 dB impedance bandwidth of 5.38% (41.42 GHz – 43.78 GHz) and an isolation of -43.6 dB. Table 2.2 presents a summary of the MIMO antenna designs for mm-wave frequency described in this section. From the table, it is observed that most of the reported works on MIMO antenna designs at high frequencies are in the mm-wave bands and there is need for MIMO antenna designs for D-band frequencies. In addition, the use of MTM structures is attractive for MIMO antenna isolation improvements at high frequencies.

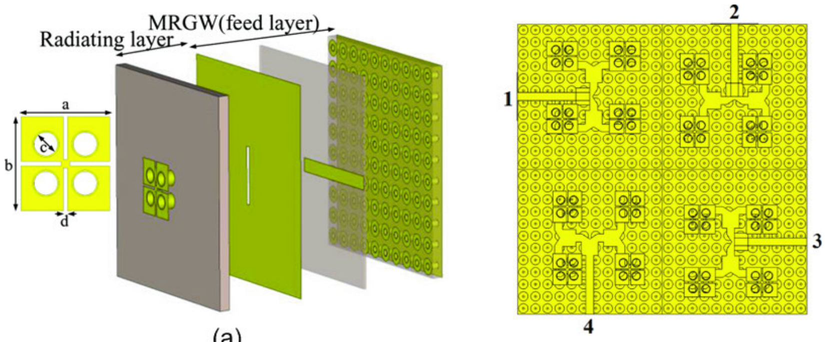

(a) (b)

Figure 2.36: Structure of the MRWG fed ME antenna (a) single element and (b) 4 × 4 MIMO arrangement with 2 × 2 subarray [113]

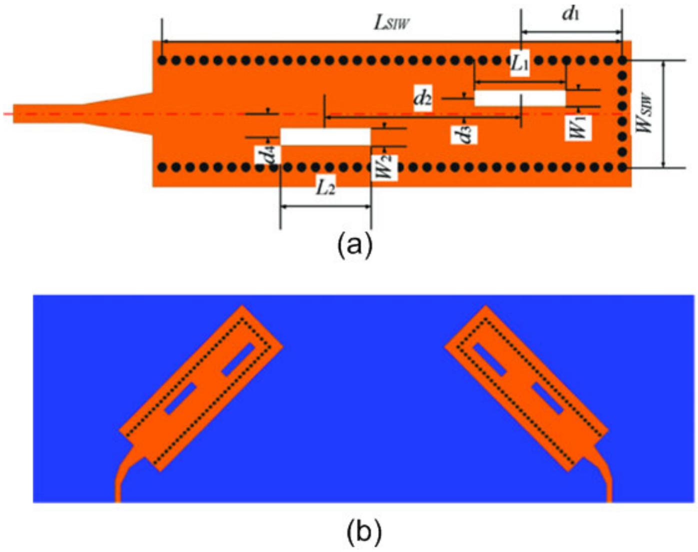

Figure 2.37: Structure of the proposed SIW slot antenna (a) single element and (b) Configuration of the 2 × 2 MIMO [114]

Table 2.2: Summary of the different MIMO antenna designs

| Ref | Type | $f_0$ (GHz) | Bandwidth | Gain | Efficiency | Isolation | Remarks |
|---|---|---|---|---|---|---|---|
| [105] | MPA | 60 | 14.6% | - | - | -15 | Antenna orientation and stub |
| [106] | MPA | 57-64 | 12.3% | - | 50%-60% | -15 | Antenna orientation and NL |
| [107] | MPA | 60.4-68.9 | 13.14% | 8.8 | 96.5%-98% | -15 | Antenna orientation, Patch holes and DGS |
| [108] | MPA | 60 | 7% | 7.5 | 94% | -20 | AMC reflector |
| [109] | DRA | 57-63 | 10% | - | 90% | -30 | Antenna orientation and FSS wall |
| [110] | DRA | 56.6–64.8 | 13.5% | 7.9 | 91% | -30 | Antenna orientation and Metasurface wall |
| [111] | DRA | 57-64 | 11.6% | - | 88% | -16 | Antenna orientation and MTMPR wall |
| [112] | DRA | 57-64 | 11.6% | - | - | -15 | Antenna orientation, superstrate and DGS |
| [113] | ME dipole | 57-71 | 21.9% | 14.5 | 82% | -30 | Antenna orientation and EBG |
| [114] | Slot | 41.44 - 43.74 | 5.47% | 7.8 | - | -43.6 | Orthogonal and spatial diversity |

Efficiency - radiation efficiency

## 2.6 Metamaterials

Metamaterials (MTMs') are artificial sub-wavelength composite materials which exhibit unusual electromagnetic properties that are not found in naturally occurring elements. Their unique characteristics such as the negative refractive index and negative phase velocity make these materials attractive for applications in the design of components with enhanced functionalities. These materials encompass engineered textured surfaces, artificial impedance surfaces, artificial magnetic conductors, double negative materials, frequency selective surfaces, Photonic Band-Gap (PBG) surfaces, Electromagnetic Band-Gap (EBG) structures, fractals and chirals [115].

Investigation on MTMs was theoretically carried out in 1968 by Veselago. However, it was not until 1996 when Pendry *et al* [116] demonstrated a practical MTM structure using an array of thin wires and split-ring resonators (SRRs) to achieve negative values of permittivity and permeability. Since then, the interest in the study of metamaterials has seen the investigation on various shapes and geometries. MTMs are commonly realized from periodic arrangement of these structures (also referred to as unit cells) printed on a dielectric substrate. When the period is smaller than the guided wavelength, the MTM structures exhibit negative permittivity, negative permeability or both. The electromagnetic response and functionalities of MTMs is dependent on the geometry of the unit cell and the associated structural dimensions.

When electromagnetic waves interact with MTMs, they exhibit unusual characteristics which may be used to manipulate the electromagnetic behavior of antennas. They have been applied in the design of antennas for the enhancement and optimization of different performance characteristics such as gain, bandwidth, directivity, isolation, antenna size reduction among others.

MTMs are designed to provide control of the reflected and transmitted electromagnetic waves and to possess different properties and functionalities. The different functionalities can be broadly categorized into frequency selective surfaces, high-impedance surfaces (HIS), perfect absorbers, polarization transformers, radiating surfaces, wavefront shaping surfaces, two-dimensional flat lenses and non-linear metasurfaces [117]. Fig. 2.38 shows the schematic illustrations of the functionalities of the MTMs commonly used in the manipulation of antenna characteristics. A brief description of these functionalities is presented below.

### 2.6.1 Frequency selective surfaces (FSS)

FSSs are made of periodic arrangement of metal patch elements or aperture arrays patterned on a dielectric substrate. The choice of the shape and dimensional parameters of the patch or aperture determines the filtering behavior of the MTM. FSSs are engineered to exhibit bandpass and bandstop characteristics on electromagnetic waves incident on their surfaces, within a narrow frequency band. Broadband or multiband FSS can be achieved by use of complex-shaped unit cells. FSS structures have been applied as superstrates for antenna bandwidth enhancement [77] and gain improvement [88], [89] or as metasurface walls/shields [109], [110] for the improvement of isolation in DRA MIMO antennas.

### 2.6.2 High impedance surfaces (HIS)

HISs is a class of MTMs with the property that an incident wave is totally reflected in phase, without supporting bounded surface waves. If the surface impedance $|Z_s|$ is very high, the reflection coefficient at the surface approaches $+1$, and the tangential magnetic field has a null in the metasurface plane inducing zero surface electric currents. Total

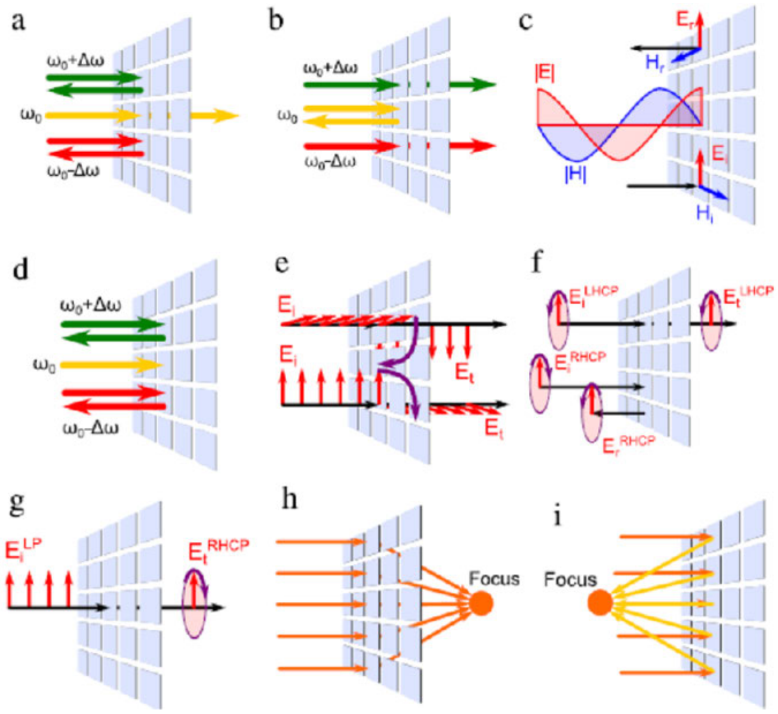

Figure 2.38: Different functionalities of metamaterials (a) bandpass FSS (b) bandstop FSS (c) HIS (d) narrowband perfect absorber (e) $90^o$ polarization rotator (f) RHCP FSS (g) LP-to-CP converter (h) focusing transmitarray and (i) focusing reflectarray [117]

reflection occurs only due to the non-zero effective magnetic currents [117]. In this state, the surface is referred to as a perfect magnetic conductor (PMC). Magnetic currents do not exist in nature, and a surface exhibiting such reflection behavior is achieved from engineered periodic structures and is referred to as an AMC. PMCs can be realized on grounded dielectric substrate as arrays of mushroom structures or simply as periodic arrays of uniplanar flat metal elements (without vias). PMCs can be used to design low-profile antennas with high radiation and high gains because the surface supports constructive interference. A HIS can also be used to suppress the propagation of surface waves. The periodic patterning produces EBG MTM which may be employed for the decoupling of low-profile antennas printed on the same grounded dielectric substrate. An EBG surface is proposed in [87] for gain improvement in a DRA. A high impedance AMC surface is also presented in [108] for the improvement of isolation in linearly arranged quad-port MPA elements at 60 GHz.

### 2.6.3 Perfect absorbing metasurfaces

A perfect absorber absorbs 100% of the incident electromagnetic power under a specified angle of incidence at a single frequency. Historically, frequency selective absorbers were designed as lossy and non-reflective coatings on conducting metal sheets to prevent back scattering on radar targets. Perfect absorbers can be designed from thin metasurfaces as metal patches, mushroom-type, split-ring resonators etc. on thin dielectric layers. It is possible to design microwave absorbers which are optically transparent beyond the absorption frequency region. A MTM based electromagnetic absorber is presented in [118] for radar applications.

### 2.6.4 Polarization transformers

Polarization transformers are used to manipulate the polarization state of an incident electromagnetic wave. These manipulations include the conversion of linear polarization (LP) to dual-polarizations or circular polarizations (CP), rotation of the polarization plane as well as polarization selectivity which is the capability of a MTM to transmit or reflect electromagnetic waves depending on their polarization states. These generally comprise of a number of stacked metal-dielectric layers, with each layer comprising of an array of complementary split-ring resonators (CSRR). The rotation provided by a single layer is limited, necessitating the use of multiple layers. Polarization rotation can also be achieved using a two-layered surface of chiral MTM of unit cells (with no mirror symmetry) such as an array of Gammadions. Other MTM transformers is the circular-polarization selective surface (CPSS) which transmits CP waves for one handedness while totally reflecting CP waves of the opposite one. MTMs have been applied for conversion of LP to CP [119] and to minimize mutual coupling in MIMO antennas [111].

### 2.6.5 Leaky-wave metasurfaces

MTMs are designed for the manipulation of electromagnetic waves incident on their surfaces. However, they can also be designed to radiate electromagnetic power into free space. MTM based leaky wave antennas radiate electromagnetic energy as they travel down the surface.

### 2.6.6 Wavefront shaping with MTMs

Sometimes, it may be necessary to manipulate the wavefront to achieve beam focusing, de-focusing, reflection or refraction of the propagating wave through some medium. Conventional reflectarrays are used to totally reflect an incident wave while changing the shape of the wavefront. Transmitarrays modify the wavefront shape without reflection. MTMs can be designed to manipulate the wavefront by controlling the reflection or transmission phase of the wave.

## 2.7 Chapter summary

This chapter provides the theoretical background for the design of high-frequency dielectric resonator antennas. The chapter begins with a survey of the different types of antenna structures and topologies existing in literature for mm-wave and sub-THz frequencies and the various design techniques employed for improvement of bandwidth, gain, directivity and radiation efficiency characteristics. The different technologies used in the fabrication and packaging of the miniaturized antennas at high frequencies is discussed. Special emphasis is given to the SIW-DRA designs due to its low Ohmic and interconnection losses as well as its desirable attributes of small size and low-profile required for miniaturization and integration with other circuit elements.

Basic parameters such as radiation patterns, impedance bandwidth, gain, directivity and radiation efficiency are often used to characterize and evaluate the performance of antennas. Descriptions and expressions for the determination of these parameters are presented. The understanding of these parameters is necessary to describe the antenna performance.

This chapter discusses the radiation characteristics of dielectric resonators and its applications as antenna elements. The theory on the design of a DR element, the associated feeding arrangements and the various optimization approaches for performance enhancements is outlined. The chapter further introduces the concept of MIMO technology and a survey of the MIMO antenna designs for mm-wave and sub-THz antennas.

This chapter also introduces MTM structures and describes the different functionalities of MTM surfaces. The ability of these MTMs to manipulate electromagnetic waves incident on them renders them attractive for improvement of antenna performances. This chapter illustrates the different applications of MTMs for bandwidth, gain and isolation improvement as well as size miniaturization in antennas. MTMs are continuing to draw great interests and may be considered potential solution in the design of high performance MTM-based antennas at sub-THz frequencies.

# Chapter 3

# DESIGN OF WIDEBAND SIW-FED DRA USING HIGHER-ORDER MODES

## 3.1 Introduction

This chapter presents the design of a wideband SIW-fed DRA antenna using the excitation of higher-order modes. In the previous chapters, the fundamentals of the DRA design and the improvements in the DRA bandwidth performance were outlined. These bandwidth enhancement techniques may broadly be categorized as those involving the modification of the DR element, incorporation of additional structures, modification of the feed structure and the excitation of higher-order modes.

At mm-wave frequencies, the size of the DR element is small in size, with dimensions in the order of $\lambda_0/\sqrt{\epsilon_r}$. Techniques involving the modification of the DR to create perforations and fractal geometries may pose challenges in shaping the DR. The hardness of the materials that make up the DR, together with the manufacturing tolerances for small-sized objects make it difficult to re-shape the DR element with precision. The incorporation of additional structures such as stacking and superstrates introduce additional complexities, such as high profiles and increase in physical size, which may render the design lack the compactness required for ease of integration.

The RDRA offers practical advantages in the design of antennas for different applications. The challenge associated with the practical realization of small mm-wave DRAs may be mitigated by the use of large-size DR elements. Large size DR elements can be excited in their fundamental and higher-order modes to produce multiple resonances. These multiple resonances can be merged together to produce multiband or broadband antenna designs. This is achieved through the application of impedance matching schemes to improve the antenna input impedance, thereby causing the merging together of the closely lying resonant bands. Compared to the aforementioned techniques, the advantage of the use of higher-order modes is that it does not increase the complexity of the manufacturing process. This chapter proposes a wideband antenna design based on the excitation of higher-order modes. The design philosophy of the antenna together with the applied impedance matching techniques is presented and analyzed.

## 3.2 Antenna design

The proposed design of the antenna involves the designs of both the feed structure and the radiating element. The details of the designs are presented in this section:

### 3.2.1 SIW design

Fig. 3.1 shows the geometry of a DR element fed from a SIW through an aperture slot. The SIW feed is designed from RT Duroid 5880 substrate material of dielectric constant $\epsilon_r$=2.2, a loss tangent of $\tan\delta$=0.0009 and a substrate height of $h$=0.254 $mm$. This substrate has a low dielectric constant and a low dielectric loss, which make it suitable for high frequency and broadband applications [120]. The thin substrate is chosen to ensure low loss and wider bandwidth of operation [121]. The SIW guides the electromagnetic waves by confining it between the two rows of metalized via posts. Due to lack of longitudinal surface currents as a result of the gaps formed by the vias, the structure supports $TE_{m0}$ modes ($m$ is an integer).

The via-to-via width of the SIW is initially determined by mapping the dimensions of a D – band rectangular WR-6 metallic waveguide to achieve the same cut-off frequency $f_c$ at the lowest $TE_{10}$ mode. The cut-off frequency for propagating modes in a rectangular waveguide is determined from equation (2.26) [92]. The effective width of a SIW ($W_{siw}$) of via diameter, $d$ and pitch, $s$ is calculated using the empirical equation (2.28) [93].

This effective width ensures the waveguide operates in the fundamental $TE_{10}$ mode in this frequency range. To enable the cavity operate in a higher-order mode, this width of the SIW is scaled by an integer factor. Furthermore, to ensure confinement of the $TE$ fields and minimize the radiation along the walls, as well as minimize bandgap effects, $d$ and $s$ are selected according to the guidelines presented in [91]. The value of $s$ and $d$ is chosen large enough with their upper bounds defined by equations (2.24) and (2.25). One end of the SIW is terminated in a short circuit by use of via while the opposite end is connected to the feed-line.

A linearly tapered microstrip transition of length $L_t$ and width $W_t$ is used to match the resonator structure to the 50Ω feeding line. The dimensions of this taper are optimized over the operating frequency to achieve broadband matching.

A rectangular-shaped slot of sides $L_{slot}$ and $W_{slot}$ is etched from the top conductor of the SIW cavity. This aperture forms a central feeding slot for the DR element. The position from the short-circuited end of the resonator to the center of the slot is initially determined from $P_s = n\lambda_g/4$, ($n$ odd). This point corresponds to the maximum standing wave field intensity and thus the slot achieves good energy coupling.

A DGS of length $L_{dgs}$ and width $W_{dgs}$ is etched out from the ground plane of the SIW cavity at a position $P_{dgs}$. DGSs have the effect of altering the shield current distribution. Due to these defect(s), the transmission line characteristics (capacitance

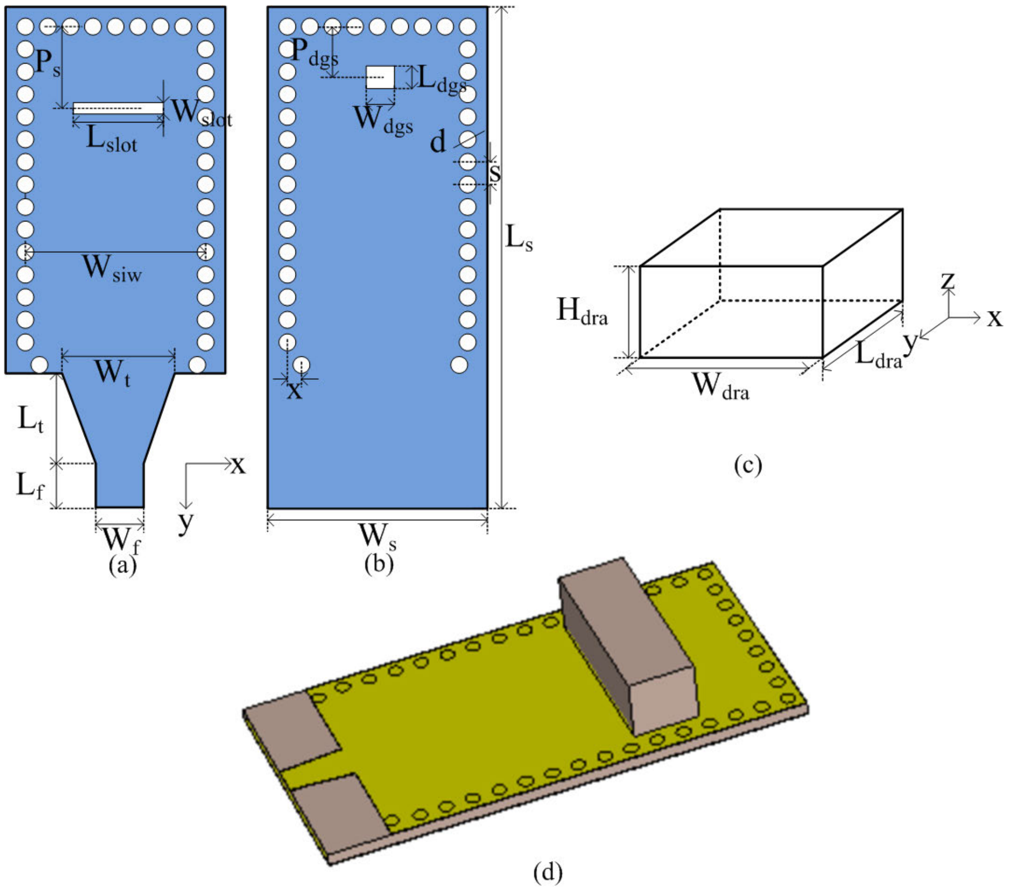

Figure 3.1: The geometry of the proposed SIW-fed DRA showing (a) the top view (b) the ground plane (c) the DRA element and (d) 3-D model

and inductance) of the structure are altered [122]. DGSs have been used in conventional MPAs to enhance gain, suppress cross-polarization to improve polarization purity and broaden the bandwidth, through improved impedance matching. In the proposed design, we apply the use of the DGS technique on a SIW cavity to increase the bandwidth of the antenna.

In addition to the DGS, an iris type discontinuity is also introduced into the SIW cavity. This improves further the impedance matching in this frequency band and enhances the impedance bandwidth. This is achieved through the offset of two vias with respect to the row of vias by a distance $x$.

### 3.2.2 DRA design

The DR element is chosen from 99.5% alumina dielectric material with a dielectric constant of $\epsilon_{rd} = 9.9$. A rectangular-shaped DR is preferred because of the higher degree of choice of the aspect ratio desirable for bandwidth control and to achieve desirable radiation characteristics. The physical dimensions of this element $L_{dra}$, $W_{dra}$ and $H_{dra}$ are selected to ensure higher mode operation of the DR. The resonant frequency of the DR element is determined by solving the transcendental equation given by the dielectric waveguide model (DWM) given by equations (2.19) - (2.23) [60].

This element is placed atop the resonator structure to form the desired SIW-fed DRA. The antenna is simulated and its parameters optimized to achieve better performance.

To simulate the proposed SIW-DRA, the structure was modeled in CST Microwave Studio. The different antenna parameters were selected according to section 3.2 above. These parameters were optimized for better antenna performance. Table 3.1 shows the optimized parameters of the proposed antenna.

Table 3.1: Optimized antenna parameters

| Parameter | Description | Value | Parameter | Description | Value |
|---|---|---|---|---|---|
| $d$ | Via diameter | 0.29 | $P_{dgs}$ | DGS position | 0.94 |
| $h$ | Substrate height | 0.254 | $s$ | Via pitch | 0.56 |
| $H_{dra}$ | Resonator height | 1.29 | $W_{dgs}$ | DGS width | 0.42 |
| $L_{dgs}$ | DGS length | 0.4 | $W_{dra}$ | Resonator width | 3.89 |
| $L_{dra}$ | Resonator length | 1.39 | $W_f$ | Feed width | 0.67 |
| $L_f$ | Feed length | 0.3 | $W_s$ | Substrate width | 5.08 |
| $L_s$ | Substrate length | 10.18 | $W_{SIW}$ | Effective SIW width | 4.5 |
| $L_{slot}$ | Slot length | 1.8 | $W_{slot}$ | Slot width | 0.35 |
| $L_t$ | Taper length | 1.045 | $W_t$ | Taper width | 0.85 |
| $P_s$ | Slot position | 2.48 | $x$ | Via offset position | 0.1 |

All dimensions in are in $mm$ units

## 3.3 Simulation results and performance analysis

The slot is centrally placed with respect to the DR element to couple maximum energy from the cavity to excite higher-order resonance in the DR element. Fig. 3.2 shows the simulated $S_{11}$ performance of the SIW-DRA. The proposed design exhibits a multi-mode behavior operating in six distinct but closely lying resonant frequencies at 123.64 GHz, 125.76 GHz, 127.4 GHz, 129.9 GHz, 134.9 GHz and 137.7 GHz. An isolated DR element was simulated using the eigenmode solver of the CST to determine the modes that are excited in the DR. The modes of a rectangular resonator can be determined by observing the number of half-wave variations of the $E$ and $H$ fields along the three orthogonal directions. To determine the modes excited in the DR, we briefly illustrate the analysis of the modes. For a rectangular-shaped DR shown in Fig. 3.1, only $TE$ modes can be excited. These modes are identified by checking the electric and magnetic field patterns [123]. The modes supported are designated $TE^x_{m,n,p}$, $TE^y_{m,n,p}$ or $TE^z_{m,n,p}$ where the superscript indicates the direction of the orientation of the magnetic dipole and $m, n, p$ are the mode indices, representing the number of half-wave field variations in the three directions. For geometries of the DR shorter than half wavelength, the mode indices may be written as $m+\delta$ or $n+\delta$ $(m, n = 0, 1, 2\cdots)$ where $0 < \delta \leq 1$. When the DR element is placed on top of a ground plane, the even modes in the $z-$ direction are extinguished [60]. In addition, the numerical value of $\delta$ is seldom needed, therefore, these modes may simply be denoted as $TE_{\delta np}$ and $TE_{m\delta p}$ ($p$=odd) for $x-$ and $y-$ directed short dipoles.

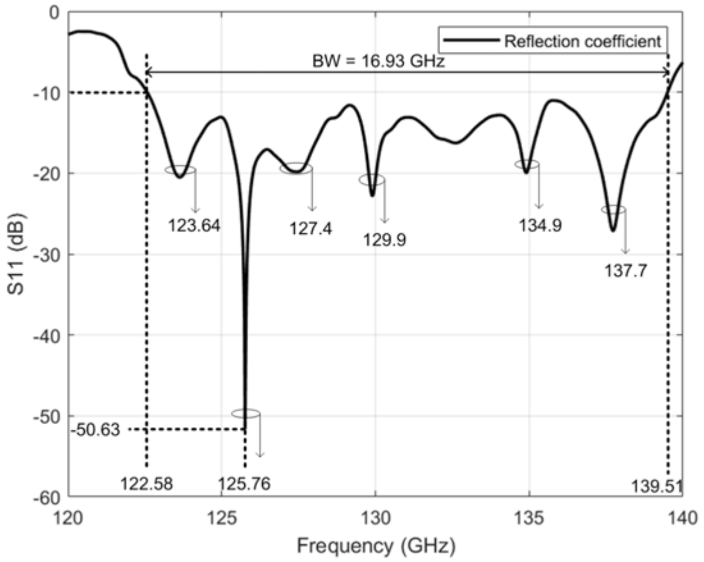

Figure 3.2: Simulated reflection coefficient of the SIW - DRA

Eigenmode simulation of an isolated DR element is used to determine the resonant modes of the DR. These modes are matched to the resonating frequencies to determine the excited modes. Fig. 3.3 shows the simulated $H-$ fields showing the different modes excited in the DR element. The half-wave variations of the $H-$ fields in the $x-$, $y-$ and $z-$ directions indicate the excited modes at different resonant frequencies. The $H-$ fields show that at these frequencies, the excited modes of the resonator are identified as $TE_{10\delta 1}$, $TE_{7\delta 5}$, $TE_{\delta 31}$, $TE_{\delta 25}$, $TE_{\delta 31}$ and $TE_{\delta 35}$, respectively. However, there is some slight frequency shifts between the resonant frequencies of the proposed design and those of the resonant modes of the DR element simulated using the eigenmode solver. Whereas the DWM model assumes an infinite ground plane for an isolated DR element, the effects of finite ground plane and that of the slot loading may cause the slight frequency shifts [124]. Simulated results show that the proposed antenna achieves a -10 dB bandwidth ranging from 122.58 GHz to 139.51 GHz, representing 13.4% at the center frequency of 125.76 GHz. This wideband operation is attributed to the merging together of the higher-order resonances as a result of the judicious selection of the DR aspect ratios and improved impedance matching between the feed line and the SIW-DRA. To achieve the improved impedance matching, two techniques have been employed, viz use of a DGS on the ground plane conductor and offsetting of the vias at the resonator–taper interface.

The far-field radiation patterns of higher mode antenna can be predicted using short magnetic dipoles and have been shown to be broadband in nature [60]. The radiation patterns of the individual resonant frequencies associated with each resonant mode is thus investigated. Each mode excited in the DR is defined by a unique field pattern. Therefore, each mode exhibits different radiation characteristics. Figs. 3.4 and 3.5 show the simulated radiation characteristics for the $E$- and $H$- planes at 123.64 GHz, 125.76 GHz, 127.4 GHz, 129.9 GHz, 134.9 GHz and 137.7 GHz resonant frequencies, respectively.

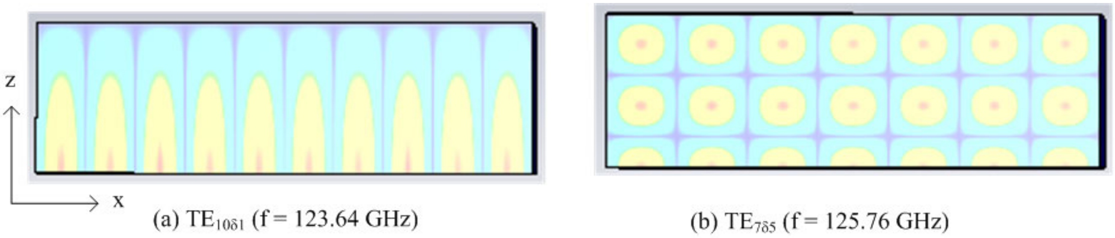

(a) $TE_{10\delta 1}$ (f = 123.64 GHz) (b) $TE_{7\delta 5}$ (f = 125.76 GHz)

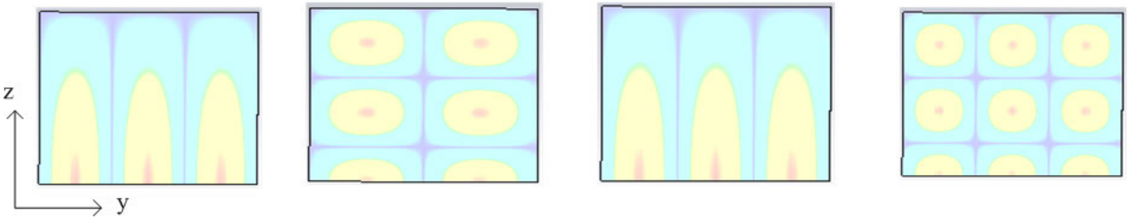

(c) $TE_{\delta 31}$ (f = 127.4 GHz) (d) $TE_{\delta 25}$ (f = 129.9 GHz) (e) $TE_{\delta 31}$ (f = 134.9 GHz) (f) $TE_{\delta 35}$ (f = 137.7 GHz)

Figure 3.3: H-field distributions of the rectangular DRA element showing different modes excited at different resonant frequencies

It is observed that the radiation patterns are generally broadband with deviations in the direction of their main lobe maxima. For the $H-$plane $\phi = 90^o$, these angles are given as $36^o$, $0^o$, $0^o$, $39^o$, $61^o$ and $0^o$ in the order of increasing resonant frequencies respectively. This difference in the direction of antenna main lobe magnitudes is attributed to the multi-mode nature of the antenna operation. Table 3.2 lists the far-field characteristics of the antenna at different resonant frequencies. It can be observed that the contribution of the "off-boresight" resonances to the overall antenna performance has been suppressed, as the resonance at these frequencies is not deep. This is explained from the reduced gains of 6.54 dBi at 123.64 GHz, 3.88 dBi at 129.9 GHz and 4.48 dBi at 134.9 GHz (as compared to 10.3 dBi at 125.76 dBi, 7.18 dBi at 127.4 GHz and 11.0 dBi at 137.7 GHz). Because of these similar broadband radiation characteristics, and the suppression of the otherwise degenerate modes, the resulting broadband response and the antenna performance is not significantly distorted but remain stable in the frequency band of operation.

Table 3.2: Far-field characteristics of the proposed antenna at different resonant frequencies

| f (GHz) | MLD | 3 dB BMW | Main Lobe Magnitude (dBi) | | | | |
|---|---|---|---|---|---|---|---|
| | ABS | ABS | ABS | Co-polar levels (dB) | | Cross polar levels (dB) | |
| GHz | Deg | Deg | H-plane | H-plane | E-plane | H-plane | E-plane |
| 123.64 | $36^o$ | $30^o$ | 6.54 | 6.37 | 9.22.4 | -5.0 | -92.0 |
| 125.76 | $0^o$ | $25.8^o$ | 10.3 | 10.3 | 11.9 | -2.69 | -88.3 |
| 127.4 | $0^o$ | $46.5^o$ | 7.18 | 7.18 | 11.8 | -2.58 | -97.3 |
| 129.9 | $39^o$ | $121.4^o$ | 3.88 | 3.71 | 8.76 | -0.28 | -90.6 |
| 134.9 | $61^o$ | $34.4^o$ | 4.48 | 3.68 | 6.28 | -0.0736 | -91.4 |
| 137.7 | $0^o$ | $31.5^o$ | 11.0 | 11.0 | 11.2 | -5.19 | -96.8 |

ABS - Absolute, BMW - Beamwidth, MLD - main lobe direction

The levels of co-polarized and cross-polarized components of the radiated fields are important in determining the polarization loss of the antenna. In particular, increase in cross-polarization fields leads to the degradation in the radiation performance of the antenna. The use of higher-order modes to achieve higher bandwidth has been attributed to increase in cross-polarized radiation in patch antennas [125] and dielectric resonators [126]. The radiation performance of the proposed design is further investigated through the observation of these fields. The levels of the co-polarized and cross-polarized fields for $H$- plane is shown in Fig. 3.5 for the different resonant frequencies.

From the plot, the main lobe magnitudes for the cross-polarized fields in the $H$-plane are -5.0 dBi, -2.69 dBi, -2.58 dBi, 0.28 dBi, -0.0736 dBi and -5.19 dBi in the direction of increasing resonant frequencies respectively, while in the $E$-plane, these field magnitudes are -92 dBi, -88.3 dBi, -97.3 dBi,-90.6 dBi, -91.4 dBi and -96.8 dBi respectively. It can be observed that while the level of cross-polarized field component in the $E$- plane is greatly minimized with respect to the co-polarized fields, the contrary is true for the $H$- plane. In the $E$- plane, there is suppression of the degenerate modes with radiation patterns that would increase the level of cross-polarization, and distort the overall antenna radiation pattern. This is attributed to the similar radiation characteristics of the slot and that of the DR, which minimizes the cross-polarized fields [53]. The proposed design offers a poor cross-polarization performance in the $H$- plane, compared to that of the $E$- plane.

The increase in the level of the cross-polarization in the H- plane has been explained by [127] and [128] for a circular patch antenna and SIW-fed slot antenna respectively. In [127], there is evidence of experimental existence of orthogonally polarized $E$-fields (cross-polarization). This field is typically lower than the co-polarized fields while significantly increases in the H-plane. This phenomenon has been attributed to first higher-order modes. Theoretical analysis has shown absolute absence of cross-polarized fields for an infinite ground plane. Therefore, low level of the cross-polarized field is as a result of the finite ground plane. Yi *et al* [128] have endeared to explain the phenomenon of increased co-polarized fields by observing the $E$ and $H$-fields for an open slot antenna. Using a similar intuition, we analyze the electric and magnetic fields on the SIW section of the antenna. Fig. 3.6 shows these $E$ and $H$-field distributions. The electric field is always vertical in the SIW section of the antenna. For a wave propagating down the waveguide, the direction of this field changes from vertical to horizontal at the slot. From Fig. 3.6, it can be observed that near the slot, the $E$-field is not purely horizontal while the $H$-field is not parallel to the open slot. These effects lead to cross-polarized fields.

The enhancement in the bandwidth is attributed to the merging of higher-order mode resonances. This is attributed to the improved impedance matching between the feeding line and the general antenna structure. To understand the contribution of these impedance matching techniques in broadening of the bandwidth, we describe the evolution of the antenna design stages. We define four different radiating structures. Antenna I is the initial design of the SIW-DRA formed as a result of optimizing the antenna parameters. The intermediate structure of the antenna with a DGS loaded on the ground plane is designated antenna II. Antenna III is formed by offsetting the vias from antenna I. Finally,

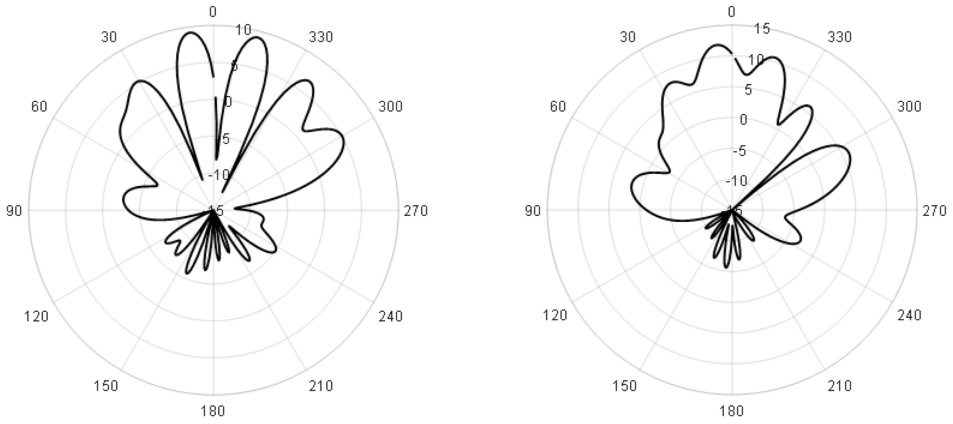

(a) f=123.64GHz (b) f=125.76 GHz

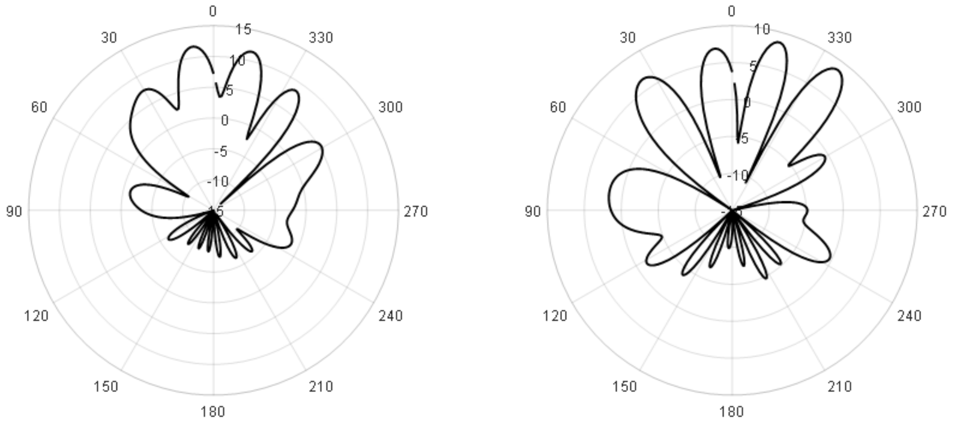

(c) f=127.4 GHz (d) f=129.9 GHz

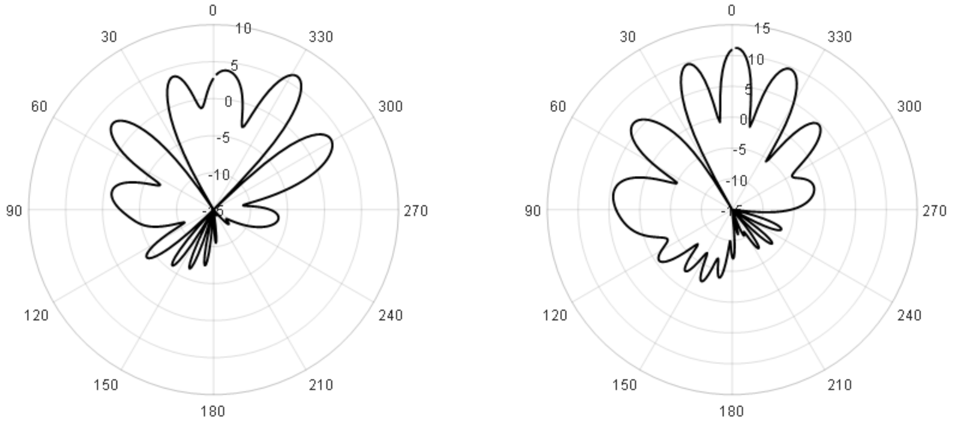

(e) f=134.9 GHz (f) f=137.7 GHz

Figure 3.4: Simulated radiation patterns showing the co-polarized fields in the *E*- plane at 123.64 GHz, 125.76 GHz, 127.4 GHz, 129.9 GHz, 134.9 GHz and 137.7 GHz. The cross-polarized fields are negligible.

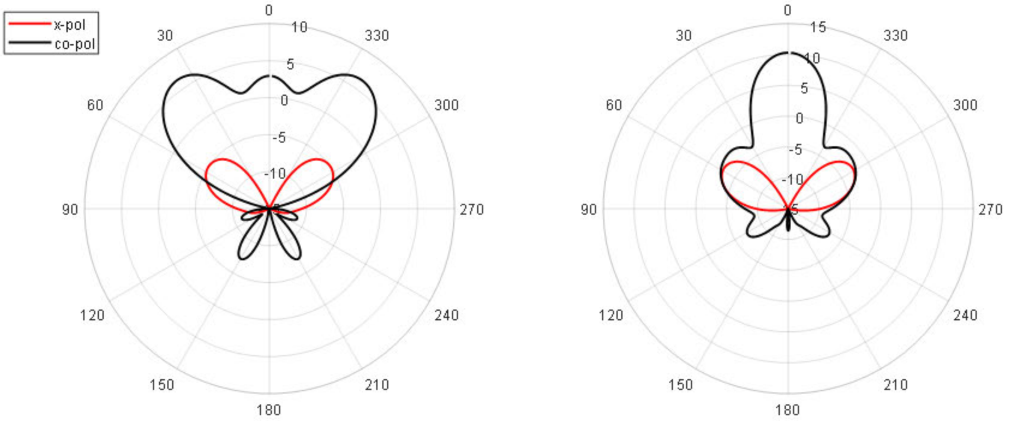

(a) f=123.64GHz (b) f=125.76 GHz

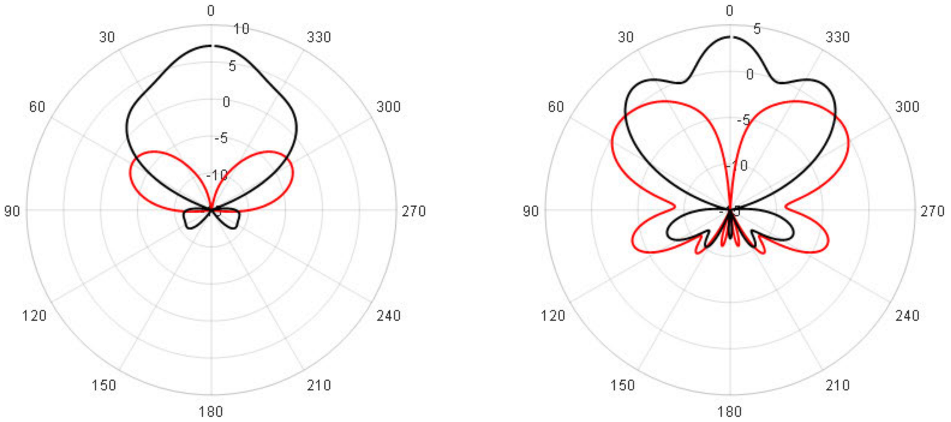

(c) f=127.4 GHz (d) f=129.9 GHz

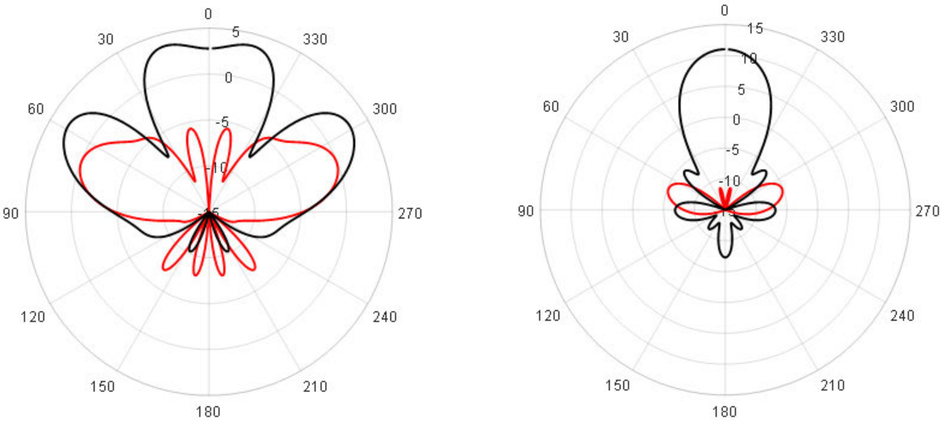

(e) f=134.9 GHz (f) f=137.7 GHz

Figure 3.5: Simulated radiation patterns showing the co-polarized and cross-polarized fields in the $H$- plane at 123.64 GHz, 125.76 GHz, 127.4 GHz, 129.9 GHz, 134.9 GHz and 137.7 GHz.

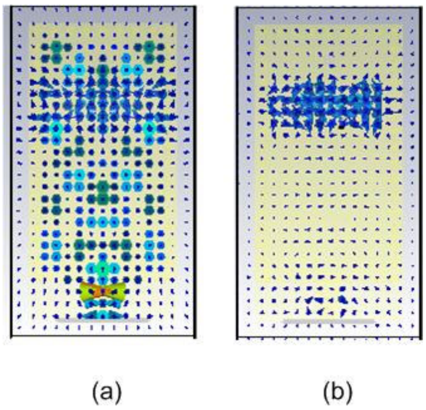

Figure 3.6: Simulated (a) E - field and (b) H - field of the proposed antenna at 125.76 GHz.

by incorporating both techniques, the resulting radiation structure is designated antenna IV. These different antenna structures were simulated and their $S_{11}$ performance compared. Fig. 3.7 shows the simulated reflection coefficients of the different radiating structures. It is observed that before the application of the impedance matching techniques, the antenna I operates in three different frequency bands (Band I - 122.29-123.84 GHz, band II - 124.53-134.65 GHz and band III - 137.1-140 GHz). It is noted that the effect of the offset via is to merge bands I and II, while the DGS is used to merge bands II and III.

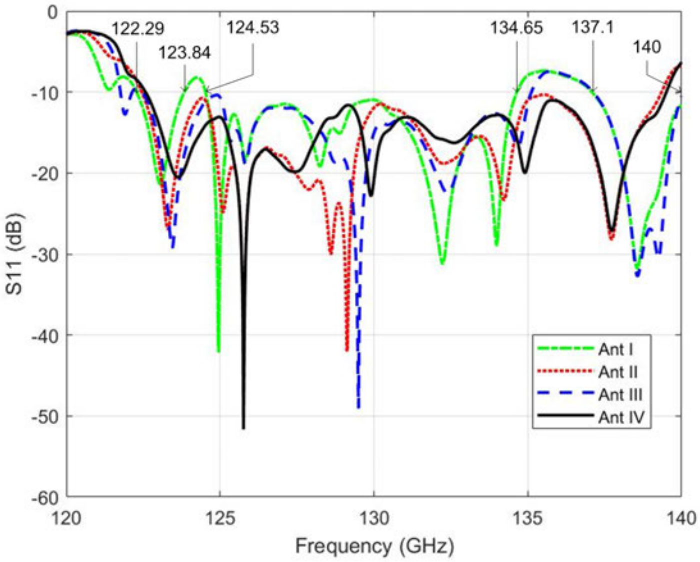

Figure 3.7: Simulated reflection coefficients for the different radiating structures.

As pointed out, the DGS disturbs the shield current distribution in the ground plane, altering the propagation of electromagnetic waves through the substrate layer. The slot has an effect of changing transmission line characteristics - capacitance and inductance of the antenna. This causes a change in the antenna input impedance for improved matching. On the other hand, the offset via causes the narrowing of the broad wall of the SIW at its input. This action is similar to the inductive iris type of discontinuity of metal waveguides.

These discontinuities have been used for impedance matching. The offset vias behave like a reactive energy storage elements. The vias excite higher-order propagating modes in the waveguide. However, these modes are evanescent and are localized within the vicinity of the vias. This effect introduces a phase shift in the wave propagating in the SIW and causes impedance transformation to achieve improved impedance matching [129]. These have the effect of improving the impedance matching within this frequency band, therefore broadening the bandwidth to achieve a wideband antenna.

The contribution of the DGS and via offset to the antenna improvement can be observed by use of a smith chart. Fig. 3.8 shows the simulated plot of the loci of the reflection coefficients of the different antenna structures at different frequencies. Fig. 3.8(a) compares the loci of antenna I and antenna II between frequencies 134.6 GHz (points A and A') and 137.2 GHz (points B and B'). This is the range of frequencies separating bands II and III of antenna I, as evident in Fig. 3.7. Etching out of the DGS on the ground place transforms the impedance in this frequency range, thus merging of bands II and III. From the plot, it is seen that the locus of antenna II (B-B') shrinks as compared to that of antenna I (A-A'), with a shift towards point $(1 + j0)$ on the chart, in the direction of the arrow. This shrinkage is associated with a reduction in the magnitude of reflection coefficients, indicating improved impedance matching. Similarly, Fig. 3.8(b) compares antenna I and antenna III between the high frequency of band I (123.8 GHz – points A-A') and the lower frequency of band II (124.6 – points B-B'). From Fig. 3.8(b), the locus of B-B' shows a reduction in the magnitude of the reflection coefficient for antenna III compared to antenna I. However, there is a counterclockwise rotation, indicating a phase shift in the reflection coefficient. This can be attributed to the reactance of the offset via.

The effects of the improved impedance matching on the radiation characteristics is further analyzed in terms of the main lobe magnitude and the side lobe levels (SLL) at the center frequency, for both the co-polarized and cross-polarized fields. The main lobe magnitudes are observed to be 9.94 dBi, 10.1 dBi, 10 dBi and 10.3 dBi for the co-polarized $H$-plane fields and 0.437 dBi, -2.85 dBi, -3.36 dBi and -2.69 dBi for the cross-polarized fields for the four radiating structures respectively. It is observed that both techniques enhances the co-polarized fields while suppressing the magnitudes of the cross-polarized fields. The SLLs are given as -12.1 dB, -11.7 dB, -12.7 dB and -12.1 dB for the co-polarized fields and -24 dB, -24.2 dB, -24.5 dB and -25.6 dB for cross-polarized fields for the different antenna structures. For the co-polarized fields, antenna II indicates a poor SLL performance as opposed to antenna III indicating the unsuitability of the DGS on SLL performance for the co-polarized fields. However, the application of both the DGS and via offset improves the overall SLL. For the cross-polarized fields, antenna II and antenna III show a reduction in the SLLs. In conclusion, we note that the applied impedance matching techniques offer improved antenna performance, and as such are appropriate.

Fig. 3.9 shows the simulated plot of the variation of the voltage standing wave ratio (VSWR) against frequency. The VSWR is less than 2.0 within the band of operation, reaching a minimum of 1.006 at the resonant frequency of 125.76 GHz. The simulated

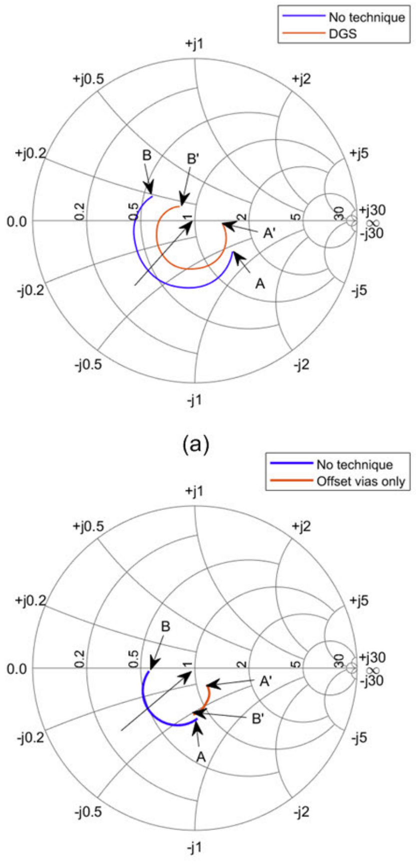

(a)

(b)

Figure 3.8: Simulated reflection coefficients of (a) antennas I and II at 134.6 GHz – 137.2 GHz and (b) antenna I and III at 123.8 GHz -124.6 GHz

gain of the antenna across the entire frequency of operation is also depicted in Fig. 3.10. The antenna achieves a peak gain of 12.3 dBi at a frequency of 126 GHz.

Besides the gain, the directivity of the antenna is presented. Fig. 3.11 shows the 3D plot of the directivity of the antenna at 126 GHz. The antenna achieves a maximum directivity of 13.14 dBi at the frequency corresponding to maximum gain. The corresponding peak radiation efficiency is 84% at the same frequency, as depicted in Fig. 3.12. The inherently high radiation efficiency is attributed to minimal conductor losses in DRA radiators.

To validate the proposed design, the antenna was modelled and simulated in Ansys HFSS software. These two softwares use different computational techniques whereby CST is a time-domain solver, whereas HFSS is a frequency-domain solver. Fig. 3.13 is a plot of the reflection coefficient generated from CST and HFSS. These are plotted on the same axes for performance comparison. The curves show agreement in terms of impedance bandwidth performance (122.58 GHz - 139.51 GHz for CST and 122.71 GHz - 139.69 GHz for HFSS) with the HFSS plot slightly shifted to the right. There is a shift in the center resonance frequency from 127.76 GHz to 130 GHz and a corresponding decrease in the minimum reflection coefficient at resonance from -50.63 dB to -32.84 dB for CST and HFSS results respectively. We further note that using HFSS, higher-order resonances

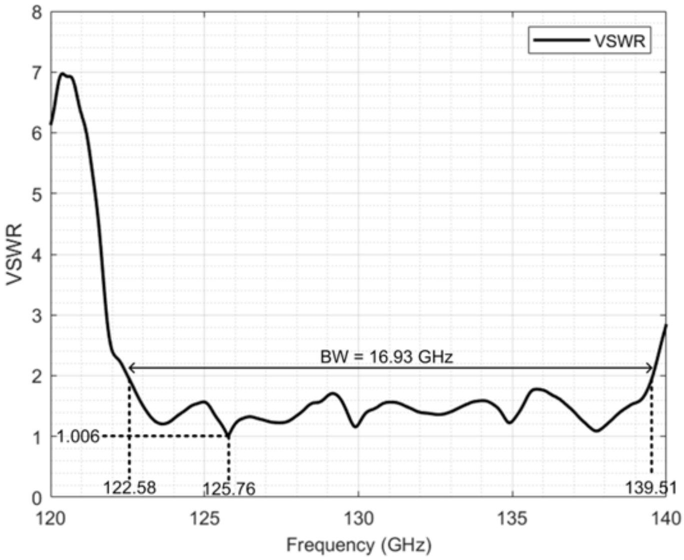

Figure 3.9: Graphs showing the simulated antenna VSWR against frequency .

occur at frequencies close to those of the CST, with a slight upward shift. This difference is attributed to the different computational techniques employed.

Fig. 3.14 compares the simulated E- and H-plane radiation pattern at the selected resonances of 125.76 GHz. 129.9 GHz and 137.7 GHz using CST and HFSS. From the figure, we observe that the radiation plots are similar in shape, with slight variations in the gains of the patterns.

Table 3.3 compares the results of the proposed design to the earlier works presented in [14], [45], [130], [69], [131], [132], [133] and [134]. Antennas with similar feeding and radiation structures are compared so as to make inferences on the proposed design. It is observed that the proposed antenna offers the same impedance bandwidth as the antenna presented in [14] which operates in the same frequency range. Despite antennas [132] and [45] offering an improved bandwidth and radiation efficiency performance, its frequency of operation is lower than the proposed design. The performance of this design, in terms of antenna gain, is superior to all the other earlier works.

Table 3.3: Performance comparison of the proposed antenna with other published works

| Reference,(year) | Type | Feeding | Technique | $f_0$,(GHz) | Bandwidth | Gain | Efficiency |
|---|---|---|---|---|---|---|---|
| [45],(2010) | CDRA | HMSIW | Cross slot feeding | 60 | 24.2% | 5.5 dB | 92% |
| [133],(2014) | RDRA | SIW | Modification of DRA | 35 | 12% | 5 dBi | 94% |
| [14],(Ant 3, 2014) | On-chip RDRA | HWSIW | HOM | 135 | 13% | 23.7 dBi | 62% |
| [69],(2016) | CDRA | SIW | Cross slot feeding | 6.56 | 8.8% | 3.7 dB | - |
| [131],(2017) | RDRA | SIW | Differential $TE_{20}$ feeding | 27.5-28.4 | 3.2% | 4.2 dBi | 86% |
| [134],(2018) | CDRA | SIW | HOM | 25.8 | 2.15% | 10.8 dBi | 87% |
| [132],(2021)-Band I | RDRA | SIW | HOM | 24.5-27.5 | 24% | 9.9 dB | 96% |
| [132],(2021)-Band II | RDRA | SIW | HOM | 33-37 | 12% | 9.9 dB | 96% |
| [130],(2021) | RDRA | SIW | Fractal geometry + HOM | 5.74 | 19.5% | 5.96 dBi | - |
| This work | RDRA | SIW | HOM | 125.67 | 13.4% | 12.3 dBi | 84% |

CDRA – Cylindrical DRA, Efficiency - radiation efficiency, HMSIW – Half Mode SIW, HOM – Higher-Order Mode, RDRA – Rectangular DRA

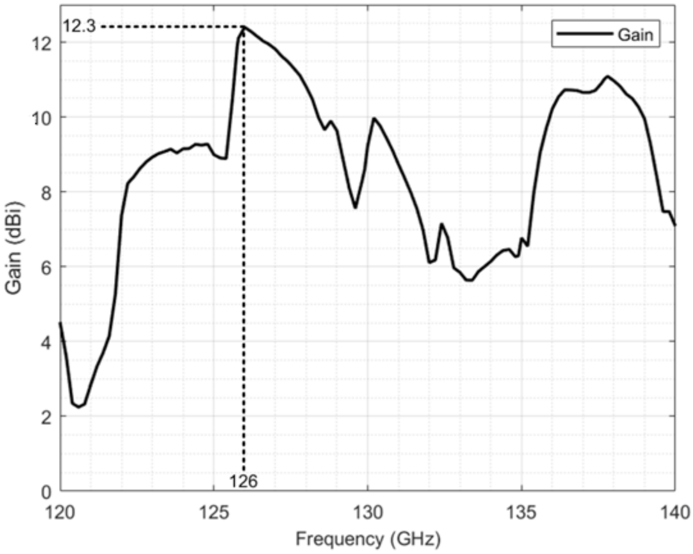

Figure 3.10: Graphs showing the simulated antenna gain against frequency.

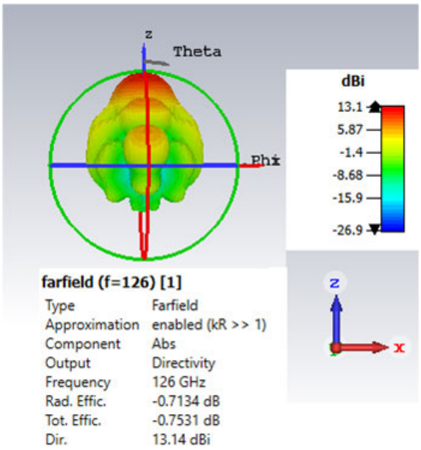

**farfield (f=126) [1]**

| | |
|---|---|
| Type | Farfield |
| Approximation | enabled (kR >> 1) |
| Component | Abs |
| Output | Directivity |
| Frequency | 126 GHz |
| Rad. Effic. | -0.7134 dB |
| Tot. Effic. | -0.7531 dB |
| Dir. | 13.14 dBi |

Figure 3.11: A 3D plot of the simulated directivity of the antenna at 126 GHz.

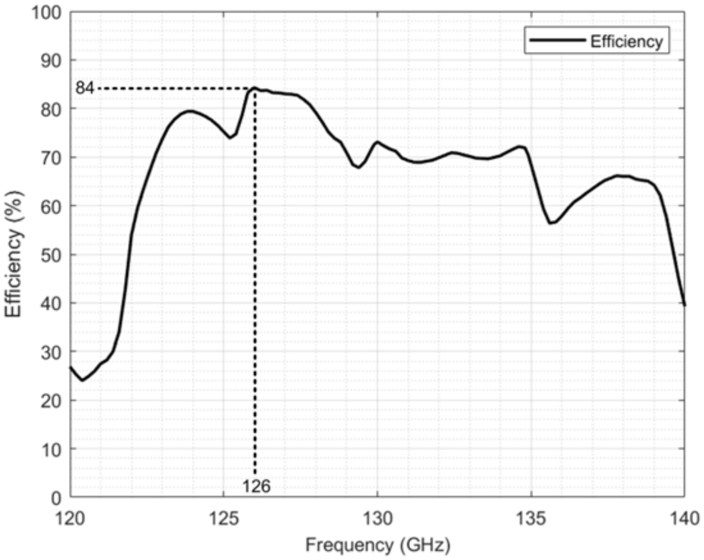

Figure 3.12: Graphs showing the simulated antenna radiation efficiency against frequency.

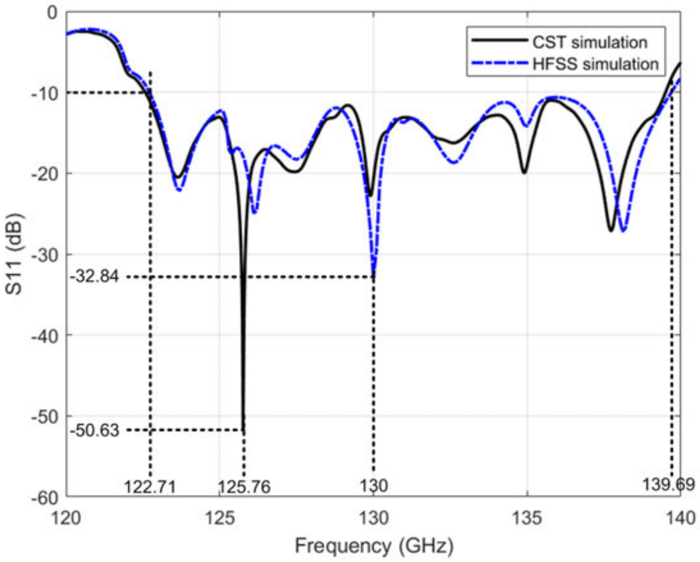

Figure 3.13: Performance comparison of the simulated reflection coefficients of the proposed design in CST and HFSS.

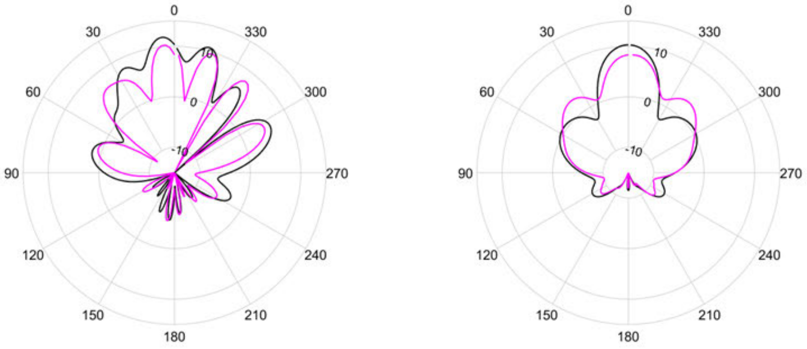

(a) E-plane (f=125.76 GHz) (b) H-plane (f=125.76 GHz)

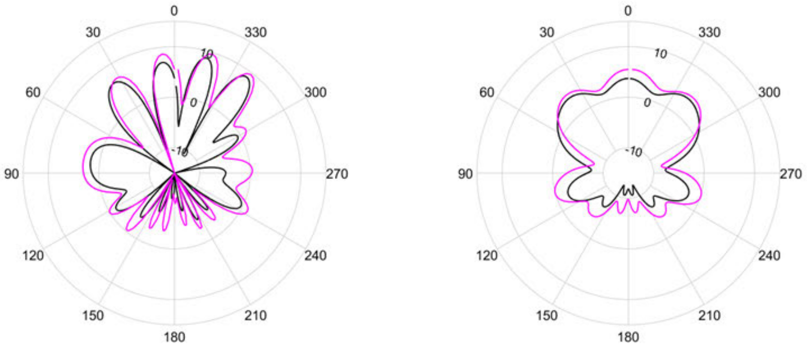

(c) E-plane (f = 129.9 GHz) (d) H-plane (f = 129.9 GHz)

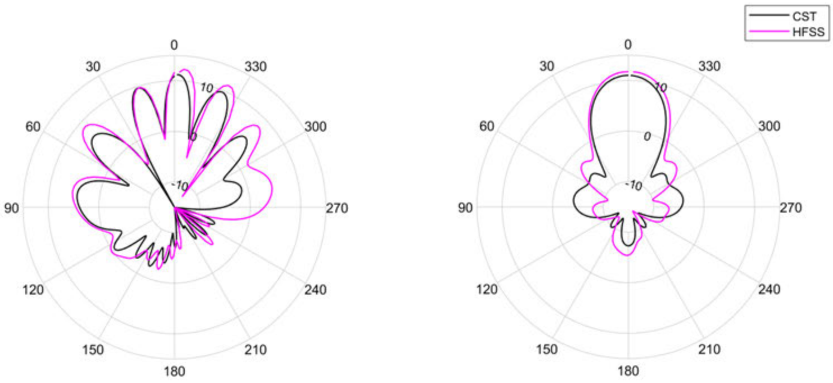

(e) E-plane (f=137.7 GHz) (g) H-plane (f=137.7 GHz)

Figure 3.14: Performance comparison of the simulated E- and H-plane radiation patterns for the proposed design using CST and HFSS.

## 3.4 Chapter summary

In this chapter, the design of a wideband SIW-DRA is presented for application in the D – band frequency regime. The antenna operates from 122.58 GHz to 139.51 GHz equivalent to a -10 dB impedance bandwidth of 13.4%. The wideband operation results from merging together of the higher-order $TE_{10\delta1}$, $TE_{7\delta5}$, $TE_{\delta31}$, $TE_{\delta25}$, $TE_{\delta31}$ and $TE_{\delta35}$ resonant modes of the DR. The wideband response is achieved through the use of a DGS and via offset techniques which improves the impedance matching of the antenna. Moreover, the antenna exhibits desirable attributes of high gain and radiation efficiency suitable for application in this frequency band.

# Chapter 4

# DESIGN OF HIGH-GAIN AND WIDEBAND SIW-FED DRA

## 4.1 Introduction

A wideband SIW-fed DRA was presented in the previous chapter. The wide bandwidth is achieved as a result of merging together of higher-order resonant modes of the DR. The judicious selection of the DR aspect ratios together with the use of a DGS and via offsetting on the SIW feed structure cause the merging together of adjacent bands for bandwidth broadening. In this chapter, we extend the excitation of higher-order modes to design a high-gain and wideband antenna for D-band applications. In the design of wideband antennas, adjacent bands of closely lying resonances are merged together through the application of impedance matching techniques. When the adjacent resonances are not close enough, the resulting antenna design is often a dual-band or multi-band antenna. These multi-band antennas are characterized by relatively narrow bandwidths in their passbands. To realize the high data rate potential of the D-band frequencies, there is a need for broadband and high-gain antennas, as outlined in Chapter 1. Therefore, the main motivation of this chapter is the need to merge together adjacent bands of a dual-band antenna.

In this chapter, three antenna designs are presented in the development of a systematic approach to merging the passbands of a dual-band antenna. The demerits of reshaping the DR element and the incorporation of additional structures as bandwidth enhancement techniques have been explained in Chapter 2. Therefore, modifications of the feeding structure become an attractive approach in the merging together of the resonances due to higher-order excitations of the DR element. In this research, we embedded inductive vias in the SIW feed to merge the resonances of a DRA for bandwidth enhancement. Section 4.2 presents the first design, which investigates the application of the inductive vias for bandwidth enhancement in SIW-fed antennas. In the second design in section 4.3, a dual-band SIW-fed DRA antenna is presented. The third design in section 4.4 proposes a systematic application of impedance matching techniques to merge the passbands of the dual-band antenna presented in section 4.3.

## 4.2 Investigations on the use of inductive vias for DRA bandwidth enhancement.

### 4.2.1 Antenna geometry

Fig. 4.1 presents the geometry of the proposed design. The antenna is designed from 0.254 $mm$ thick low dielectric constant RT Duroid substrate material, having a dielectric constant $\epsilon_r = 2.2$ and a loss tangent of $\delta = 0.0009$. The SIW structure comprises two rows of metallic vias, separated by a center-to-center distance of $W_{SIW}$ to form the boundary of the waveguide. The design equations (2.27) and (2.28) ensure that the SIW operates in the fundamental $TE_{10}$ mode. In the proposed design, the width of the SIW is chosen so that the SIW operates in higher-order mode cavity. The diameter, $d$ and pitch, $s$ of the via are selected according to the rules in equations (2.24) and (2.25) so as to minimize radiation losses along the walls of the guide. The waveguide is fed from a $50\Omega$ microstrip feed line, through a linearly tapered microstrip section for improved impedance matching. A set of transverse via joining the two rows forms a short circuit termination at the opposite end of the waveguide.

The radiating element is a rectangular-shaped DR element selected from 99.5% alumina dielectric material with a dielectric constant of $\epsilon_{rd} = 9.9$. The rectangular shape is preferred because it offers a higher degree of bandwidth control. By proper selection of the aspect ratios of the DR element, different resonant frequencies and radiation characteristics can be achieved. The DR element is fed from a slot of length, $L_{slot}$ and width, $W_{slot}$ etched on the broad wall of the SIW beneath it. This slot couples energy from the SIW to the DR element.

To improve the impedance bandwidth of the proposed antenna, a set of inductive metal shorts between the upper and lower plates of the SIW are employed. Inductive vias can be placed either individually or in pairs. The effect of an inductive post on the impedance of the network is such that it creates an electric response similar to the introduction of a shunt inductance across its electrical equivalent model. A single via is placed at a distance $y_1$ from the short-circuited end, while a pair of symmetric vias separated by $x_2$ is placed at a position $y_2$. Besides these vias, a ring-shaped DGS slot is etched from the ground plane around the single via. The inner and outer radii of the ring are $r_1$ and $r_2$ respectively. The positions of the slot $P_{slot}$ and the vias are optimized for improved return loss performance of the antenna.

### 4.2.2 Simulation results

The proposed antenna structure was modeled and simulated using CST Microwave Studio. The parameters were optimized to improve the $S_{11}$ performance of the antenna in this frequency range. The optimized antenna parameters are presented in Table 4.1. The performance of the antenna is analyzed in terms of the bandwidth, radiation

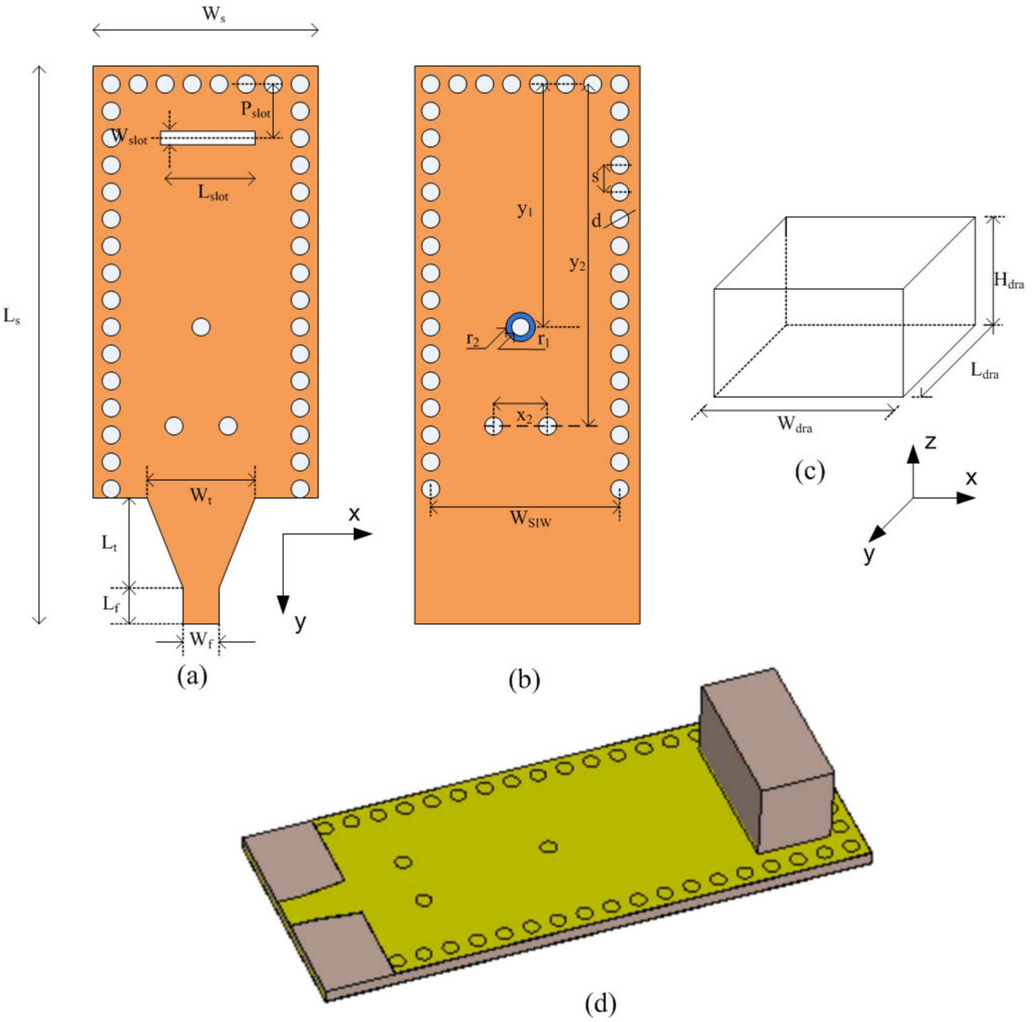

Figure 4.1: Geometry of the proposed antenna structure showing (a) the top view, (b) ground plane (c) DRA element and (d) 3-D view.

characteristics, gain and radiation efficiency.

Fig. 4.2 shows the plot of the simulated reflection coefficient, $S_{11}$ of the antenna against frequency. From the figure, it is observed that the proposed antenna is multi-resonant, operating at 139.4 GHz, 141 GHz, 144.7 GHz, 146 GHz, 147.5 GHz and 150.1 GHz frequencies. These resonances correspond to higher-order modes excited in the DRs and are characterized by narrow passbands. The individual higher order resonances are merged together to achieve a wider impedance bandwidth. It is observed that the reflection coefficient is below -10 dB between the frequencies 138.27 GHz and 150.95 GHz, with the lowest reflection coefficient of -33.96 dB at 141 GHz. This represents a -10 dB impedance bandwidth of 9%. Each of these resonant frequencies is associated with a unique field configuration, that represents the different radiation modes of the DR element.

To investigate the effects of the inductive vias on the enhancement of the antenna bandwidth, different $S_{11}$ plots describing the evolutionary design stages of the antenna are presented. These are plotted on the same axis for comparison and inference. The $S_{11}$ curves for the different design stages as depicted in Fig. 4.3 are described below.

Table 4.1: Optimized Antenna Parameters

| Parameter | Description | Value | Parameter | Description | Value |
|---|---|---|---|---|---|
| $d$ | Via diameter | 0.3 | $s$ | Via pitch | 0.54 |
| $h$ | Substrate height | 0.254 | $W_{dra}$ | Resonator width | 3.0 |
| $H_{dra}$ | Resonator height | 1.66 | $W_f$ | Feed width | 0.67 |
| $L_{dra}$ | Resonator length | 1.48 | $W_s$ | Substrate width | 4.36 |
| $L_f$ | Feed length | 0.5 | $W_{SIW}$ | Effective SIW width | 3.76 |
| $L_s$ | Substrate length | 11.02 | $W_{slot}$ | Slot width | 0.33 |
| $L_{slot}$ | Slot length | 1.7 | $W_t$ | Taper width | 0.9 |
| $L_t$ | Taper length | 0.89 | $x_2$ | $x$ distance between $2^{nd}$ via pair | 1.08 |
| $P_{slot}$ | Slot position | 1.0 | $y_1$ | $y$ position of the $1^{st}$ vias | 5.39 |
| $r_1$ | Inner radius of DGS ring | 0.15 | $y_2$ | $y$ position of the $2^{nd}$ vias | 8.12 |
| $r_2$ | Outer radius of DGS ring | 0.35 | | | |

All dimensions are in $mm$ units

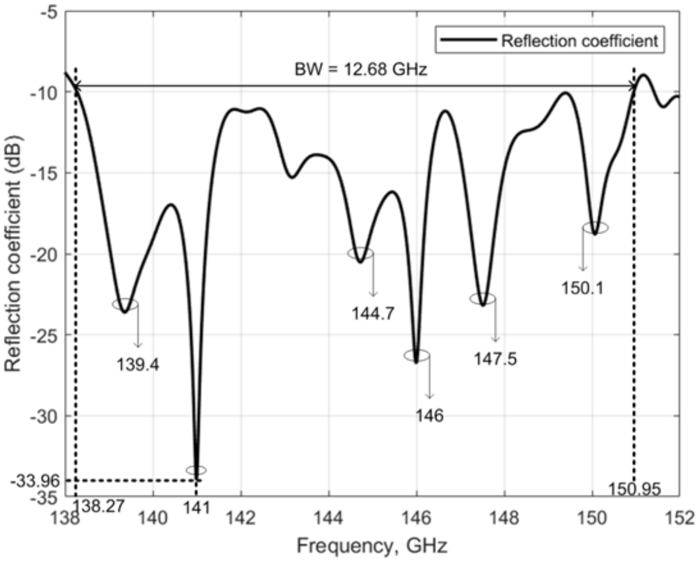

Figure 4.2: Simulated antenna $S_{11}$ performance.

#### 4.2.2.1 Antenna with neither inductive vias nor DGS applied

The $S_{11}$ curve for the antenna with neither the inductive vias nor DGS applied is labelled ”I - No technique”. The antenna exhibits a dual-band response with passbands between 140.82 GHz - 145.24 GHz and 147.27 GHz - 151.02 GHz for the lower and upper bands respectively. A narrow stop band of 2.03 GHz separates the two bands.

#### 4.2.2.2 Antenna with only inductive vias applied

The curve labelled ”II - Via only” presents the antenna $S_{11}$ performance when the antenna design stage embeds the inductive vias into the SIW feed. When compared to the case where no technique is applied, the $S_{11}$ performance shows that the mismatch at 145.24 GHz

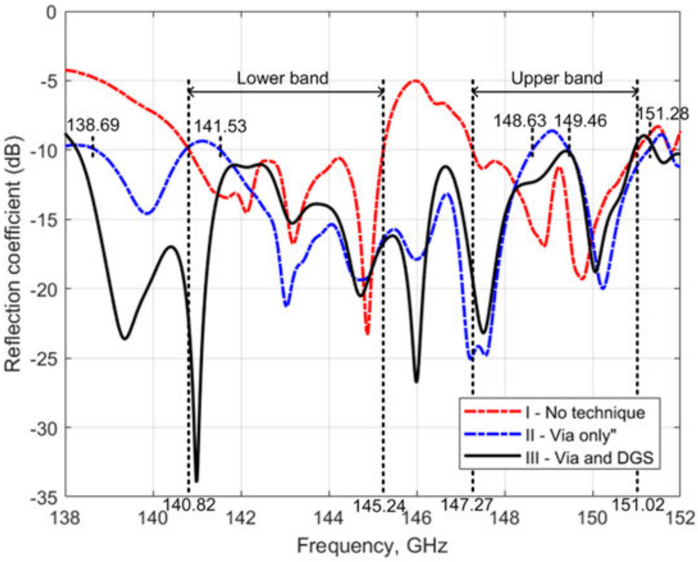

Figure 4.3: $S_{11}$ performance comparison for the different antennas under different impedance matching techniques.

- 147.27 GHz due to the stop band is eliminated. However, the vias introduce mismatches in the lower and upper frequencies. This raises the lower cut-off frequency to 141.53 GHz and lowers the upper cutoff frequency to 148.63 GHz.

#### 4.2.2.3 Antenna with both inductive vias and the DGS loaded

With the application of the inductive vias technique, the $S_{11}$ response depicts a tri-band antenna between 138.69 GHz and 151.28 GHz, with two very narrow stop bands of 0.79 GHz (140.74 GHz - 141.53 GHz) and 0.83 GHz (148.63 GHz - 149.46 GHz). The impedance mismatches at these frequencies are eliminated using a circular DGS on the ground plane. The $S_{11}$ performance of curve ”III - Via and DGS” exhibits an enhanced bandwidth between 138.27 GHz and 150.95 GHz as indicated in Fig. 4.2.

The radiation characteristics of the antenna should be stable in the frequency band of operation to minimize distortion and guarantee good antenna performance. This requires that the individual resonances should possess similar radiation characteristics. The radiation characteristics of the distinct resonant frequencies are examined. Figs. 4.4 and 4.5 show the simulated polar plots of the $E$- and $H$-plane far-field radiation patterns of the proposed design. It is observed that the radiation characteristics of the individual resonant frequencies is in the broadband direction.

The performance of the antenna is further analyzed in terms of antenna gain and radiation efficiency. Figs. 4.6 and 4.7 shows the simulation plots for antenna gain and radiation efficiency against frequency respectively. The proposed antenna has a maximum gain of 8.79 dBi and radiation efficiency of 81% at 144.7GHz

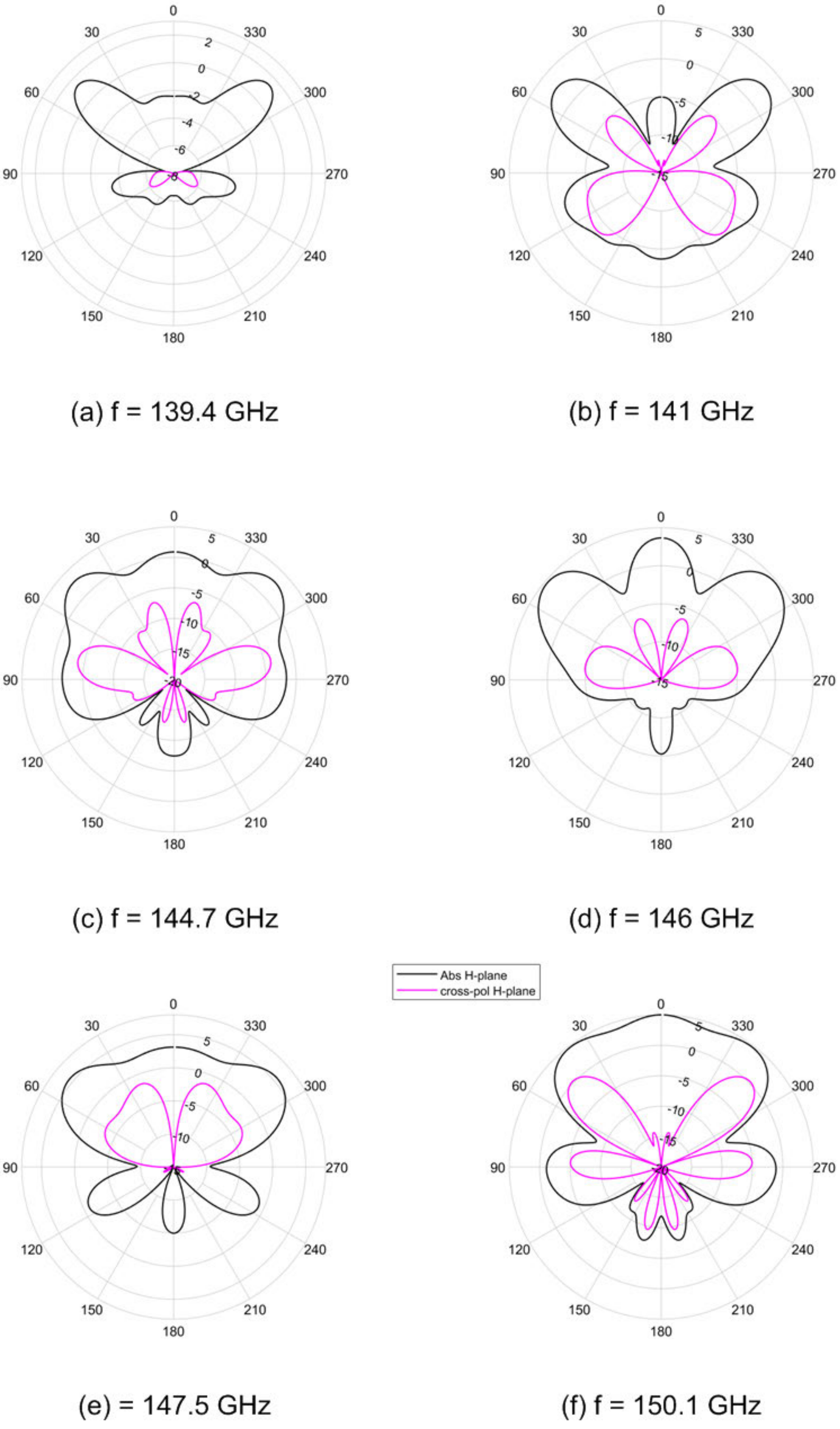

(a) f = 139.4 GHz

(b) f = 141 GHz

(c) f = 144.7 GHz

(d) f = 146 GHz

(e) = 147.5 GHz

(f) f = 150.1 GHz

Figure 4.4: Simulated H-plane radiation pattern of the proposed design showing the total H-field and cross-polarized fields at 139.4 GHz, 141 GHz, 144.7 GHz, 146 GHz, 147.5 GHz and 150.1 GHz frequencies.

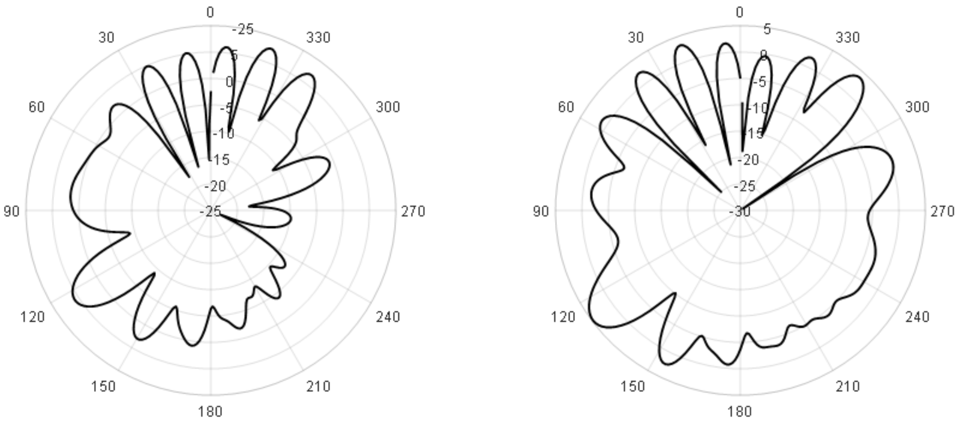

(a) f = 139.4 GHz

(a) f = 141 GHz

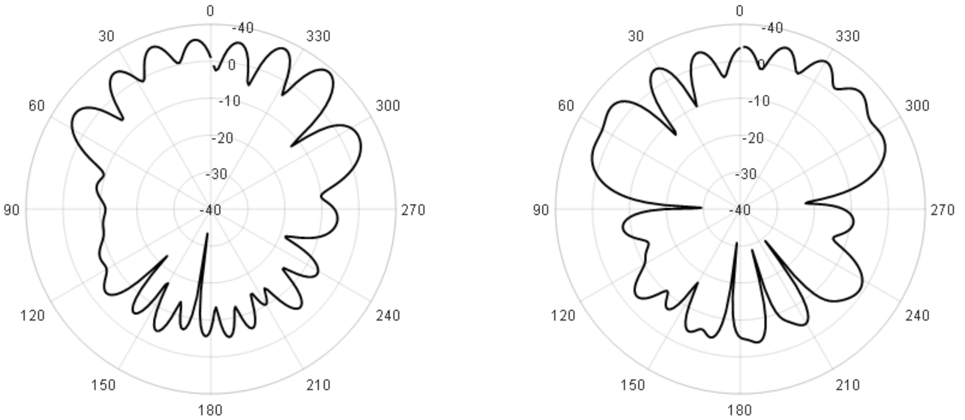

(c) f = 144.7 GHz

(d) f = 146 GHz

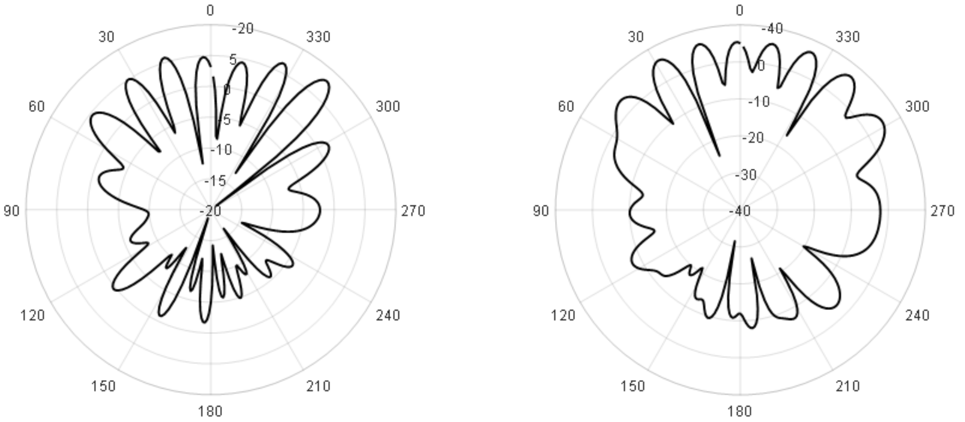

(e) f = 147.5 GHz

(f) f = 150.1 GHz

Figure 4.5: Simulated E-plane radiation pattern of the proposed design at 139.4 GHz, 141 GHz, 144.7 GHz, 146 GHz, 147.5 GHz and 150.1 GHz frequencies. The cross-polarized fields are negligible.

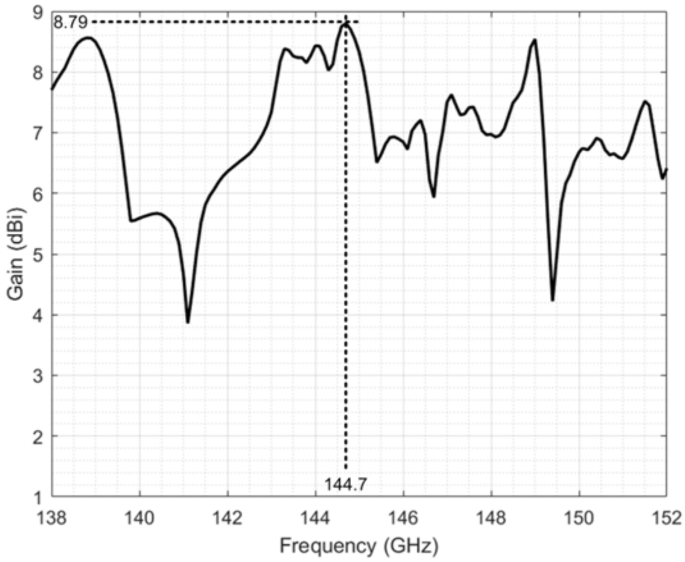

Figure 4.6: Simulated gain of the antenna.

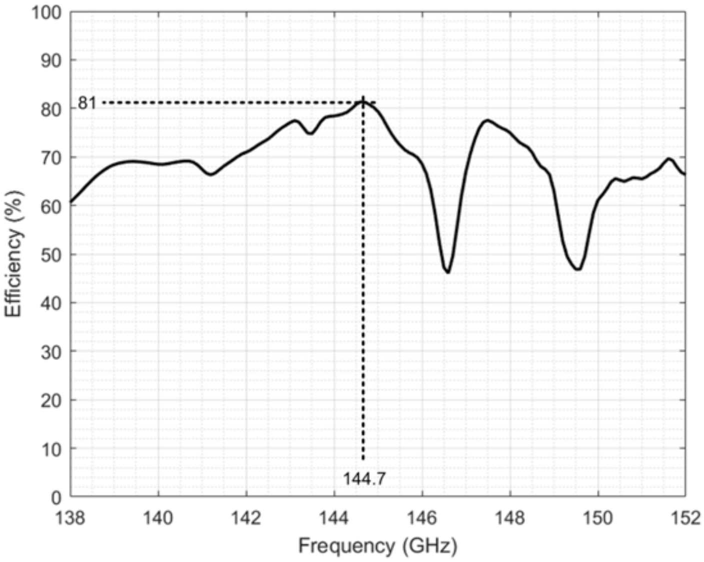

Figure 4.7: Simulated radiation efficiency of the antenna.

## 4.3 Design of a dual-band SIW-fed DRA

### 4.3.1 Antenna design

The structural geometries of the SIW cavity together with the radiating element are presented in Fig. 4.8. The SIW structure is designed on a thin dielectric laminate, to have a propagation behaviour similar to the conventional metallic waveguide. The choice of the substrate is Rogers RT/Duroid® 5880 substrate material of thickness $h = 0.254$ $mm$, with a permittivity of $\epsilon_r = 2.2$ and a loss tangent $\tan\delta$=0.0009. The SIW cavity is realized by two rows of metallized via that form the walls of the planar waveguide. The key design parameters that are important in mapping the SIW to the rectangular waveguide are the width of the SIW, $W_{SIW}$, the diameter of the via, $d$ and the via pitch, $s$. The cutoff frequency for a dielectric-filled rectangular waveguide of width, $W_{eff}$ and the width, $W_{SIW}$ are determined from equations (2.27) and (2.28). The diameter and the pitch of the via are chosen according to the rules $s \leq 2d$ and $d < \lambda_g/5$ to ensure that there is negligible leakage of electromagnetic energy through the walls of the SIW. The limitations in the fabrication processes at high frequencies is mitigated through the use of higher-order propagating modes in the SIW guide. The width $W_{SIW}$ is chosen so that the SIW operates in higher-order mode cavity. One end is terminated with a transverse row of metal via to form a short circuit. A 50Ω microstrip line feeds the cavity through a tapered transition section of length $L_t$ and width $W_t$, whose dimensions are optimized for good impedance matching.

A high permittivity material comprising of 99.5% alumina with relative permittivity $\epsilon_{rd} = 9.9$ is selected for the design of the DR element. The dimensions of the rectangular DR element $H_{dra}$, $L_{dra}$ and $W_{dra}$ are chosen for higher-order mode excitation. The resonant frequencies of these higher-order $m$, $n$ modes are determined from the transcendental equation in equation (2.19). This element is placed on top of the SIW cavity, symmetrically with respect to the aperture etched out on the top conductor of the waveguide. The DR element is excited through this I-shaped aperture beneath it. The position and the dimensions of the slot are optimized for improved impedance matching to achieve dual-band operation. The proposed topology exploits the advantages of both the DR and the SIW feed for a high-performance antenna at high frequencies.

### 4.3.2 Simulation results

The proposed dual-band antenna is designed and simulated using CST MWS commercial software for performance evaluation. Parametric optimization is performed to optimize its dimensional parameters. Table 4.2 shows the dimension details of the proposed dual-band antenna design. The performance analysis is carried out in terms of its reflection coefficients and radiation characteristics. Fig. 4.9 is a plot of the simulated reflection coefficients of the proposed dual-band design.

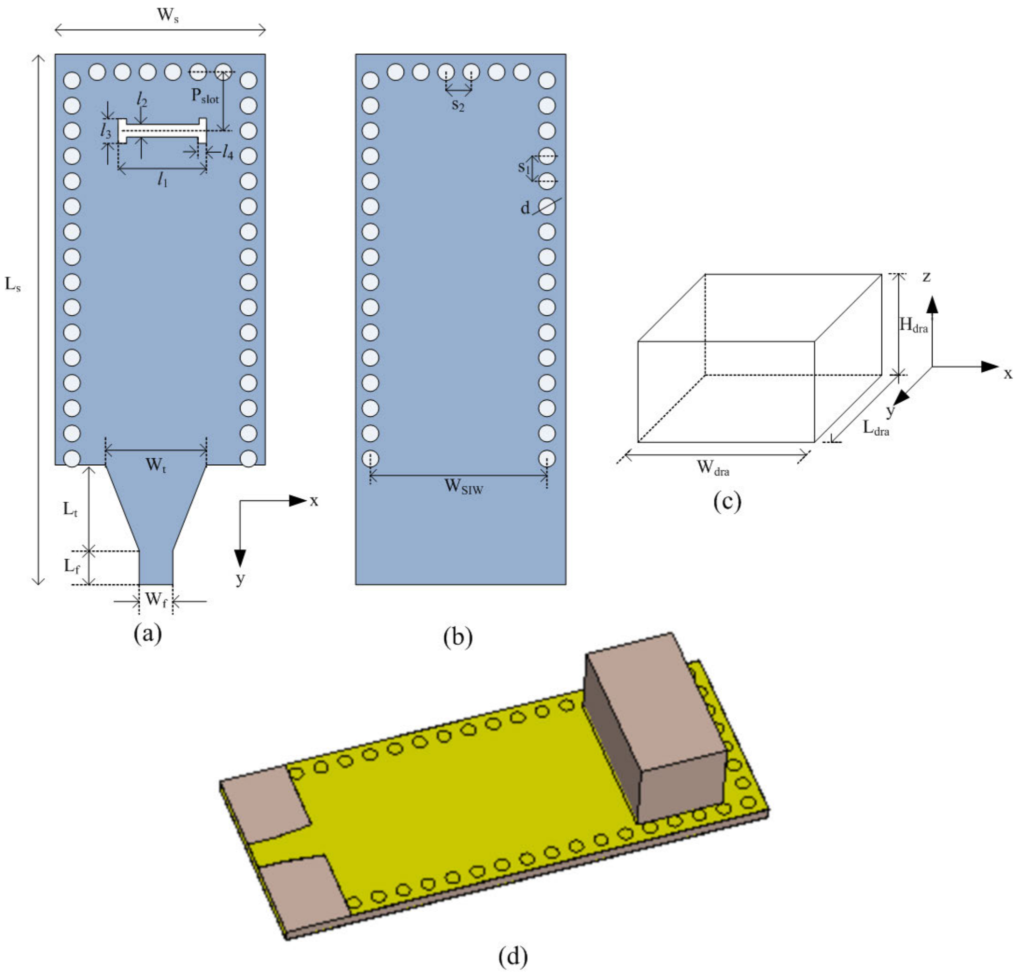

Figure 4.8: Design structure of the proposed dual-band SIW-fed DRA antenna showing (a) & (b) upper and lower conducting surfaces of the waveguide (c) the rectangular DR element and (d) 3-D view

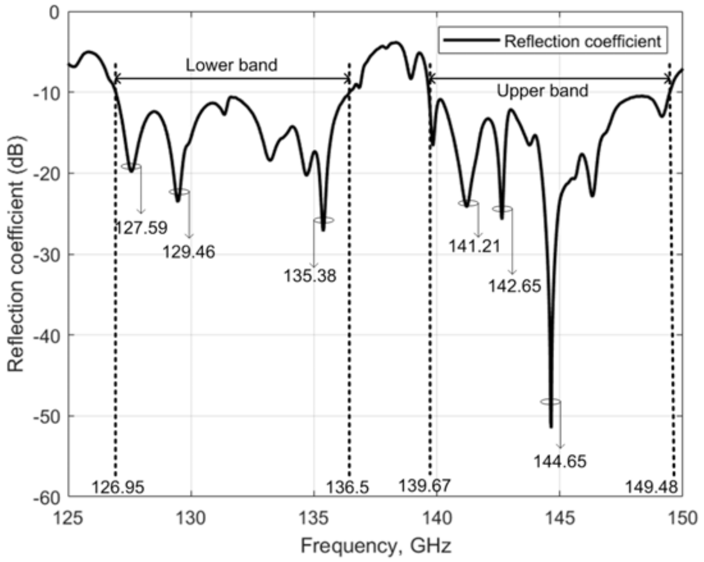

Figure 4.9: Simulated $S_{11}$ performance curve of the proposed dual-band antenna

Table 4.2: Detailed dimensions of the dual-band antenna design

| Parameter | Description | Value | Parameter | Description | Value |
|---|---|---|---|---|---|
| $d$ | Via diameter | 0.3 | $L_t$ | Taper length | 0.87 |
| $h$ | Substrate height | 0.254 | $P_{slot}$ | Slot position | 1.57 |
| $H_{dra}$ | Resonator height | 1.80 | $s_1$ | Lateral via pitch | 0.56 |
| $l_1$ | Main slot length | 1.75 | $s_2$ | Terminating via pitch | 0.53 |
| $l_2$ | Main slot width | 0.35 | $W_{dra}$ | Resonator width | 3.4 |
| $l_3$ | Minor slot length | 0.55 | $W_f$ | Feed width | 0.67 |
| $l_4$ | Minor slot width | 0.12 | $W_s$ | Substrate width | 4.31 |
| $L_{dra}$ | Resonator length | 1.95 | $W_{SIW}$ | SIW effective width | 3.71 |
| $L_f$ | Feed length | 0.6 | $W_t$ | Taper length | 0.87 |
| $L_s$ | Substrate length | 10.94 | | | |

All dimensions are in *mm* units

The $S_{11}$ curve shows the dual-band operation of the SIW-DRA with bandwidths 9.55 GHz (126.95 GHz - 136.5 GHz) and 9.81 GHz (139.67 GHz - 149.48 GHz). These represent fractional bandwidths of 7.2% and 6.78% respectively. The curve further depicts the multiple resonances. The major resonances occur at 127.59 GHz, 129.46 GHz and 135.38 GHz for the low-frequency band while the higher band resonates at 141.21 GHz, 142.65 GHz and 144.65 GHz. The physical dimensions of the DR were selected such that there is excitation of higher-order modes in the DR element. Each of these resonances corresponds to a different mode, characterized by distinct internal field distributions.

The different modes excited in a DR element are associated with different radiation characteristics [18]. The radiation characteristics of the dual-band antenna is analyzed at the different resonances. Figs. 4.10 and 4.11 show the polar plots for the simulated far-field radiation patterns in the principal planes. The far-field characteristics and details for the different resonances are shown in Table 4.3. The simulated radiation patterns at the different resonances show broadband radiation characteristics. This is expected because the radiation pattern of higher-order DR modes has been shown to be broadband [60]. Because of the similar radiation patterns, the performance of the proposed design is not degraded and the antenna exhibits stable radiation characteristics across both the bands of operation. The gain of the proposed SIW-DRA is also analyzed for evaluation of its gain performance. Fig. 4.12 shows plots of the gain against frequency while Fig. 4.13 shows the radiation efficiency as a function of frequency. The antenna achieves a realized gain of 10.69 dB with a peak radiation efficiency of 87%.

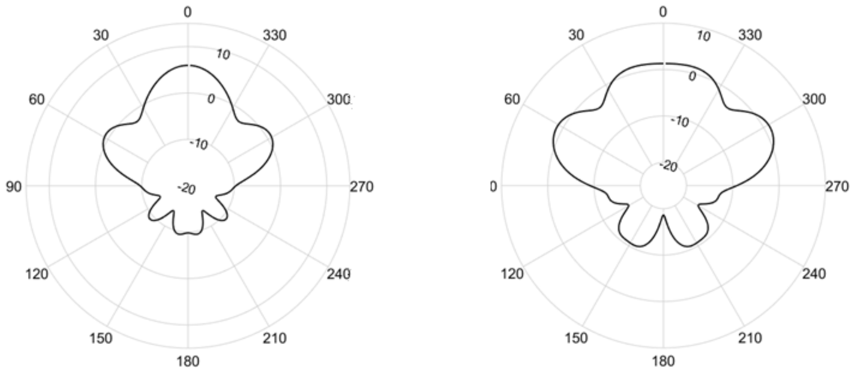

(a) f = 127.59 GHz (a) f = 129.46 GHz

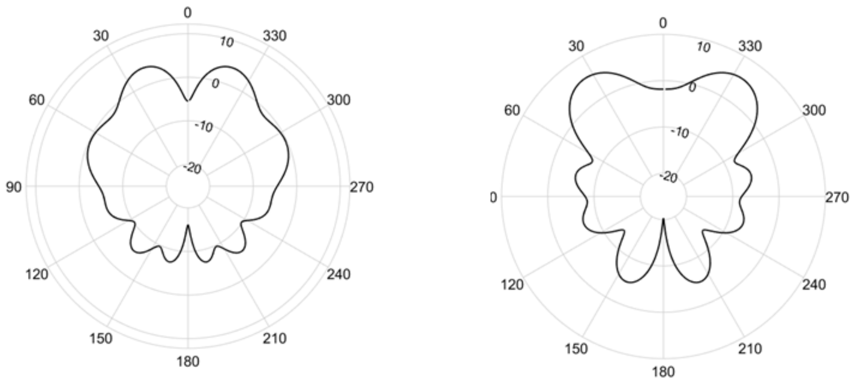

(c) f = 135.38 GHz (d) f = 141.21 GHz

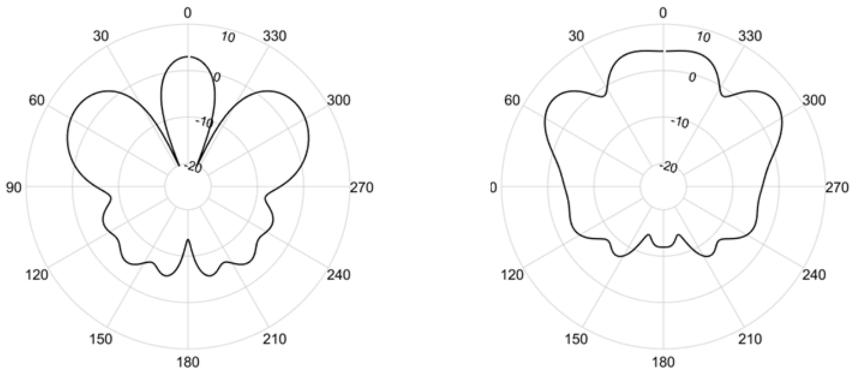

(e) f = 142.65 GHz (f) f = 144.65 GHz

Figure 4.10: Polar plots showing the simulated radiation patterns of the proposed dual-band antenna in the principal H-plane at 127.59 GHz, 129.46 GHz, 135.38 GHz, 141.21 GHz, 142.65 GHz and 144.65 GHz.

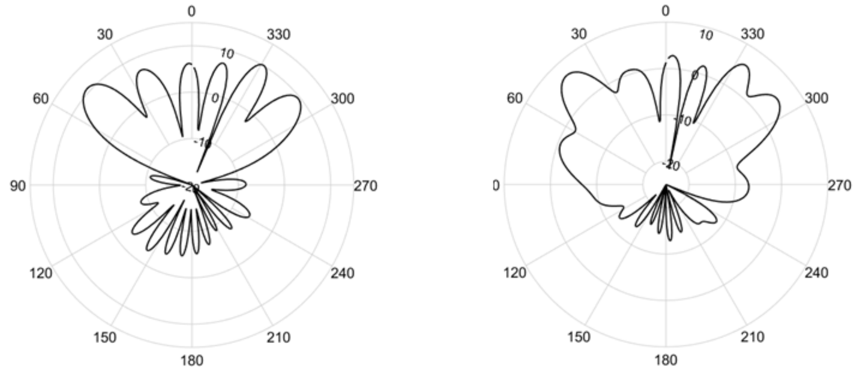

(a) f = 127.59 GHz (a) f = 129.46 GHz

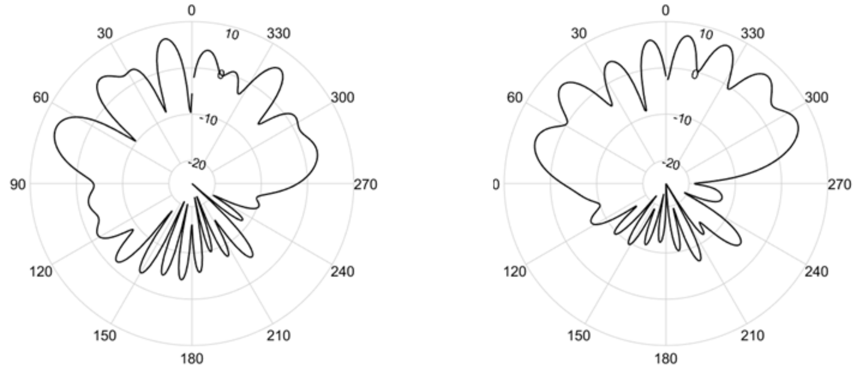

(c) f = 135.38 GHz (d) f = 141.21 GHz

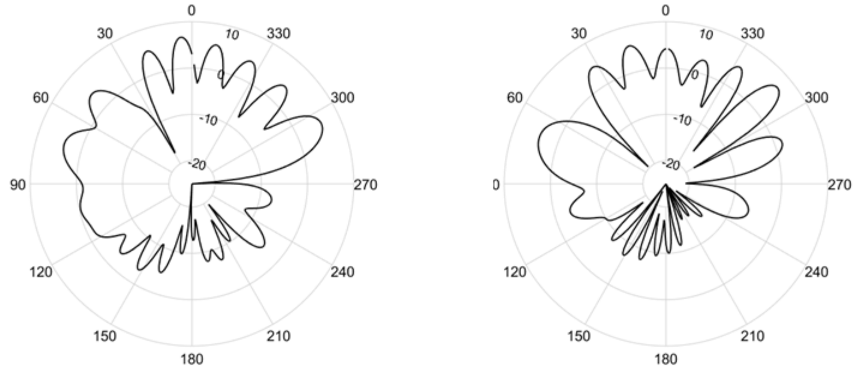

(e) f = 142.65 GHz (f) f = 144.65 GHz

Figure 4.11: Polar plots showing the simulated radiation patterns of the proposed dual-band antenna in the principal E-plane at 127.59 GHz, 129.46 GHz, 135.38 GHz, 141.21 GHz, 142.65 GHz and 144.65 GHz.

Table 4.3: Simulated radiation parameters of the proposed dual-band antenna

| E-plane | | | | | | |
|---|---|---|---|---|---|---|
| | Lower band | | | Upper band | | |
| f (GHz) | 127.59 | 129.46 | 135.38 | 141.21 | 142.65 | 144.65 |
| Main Lobe Magnitude (dBi) | 10.7 | 6.83 | 6.80 | 7.64 | 6.74 | 6.82 |
| Main Lobe Direction | $47.0^o$ | $43.0^o$ | $11.0^o$ | $24.0^o$ | $4.0^o$ | $49.0^o$ |
| 3 dB Angular width | $15.5^o$ | $15.3^o$ | $9.1^o$ | $9.6^o$ | 7.6 | $9.7^o$ |
| Side Lobe Level (dB) | -0.7 | -0.9 | -0.6 | -0.7 | -0.9 | -1.0 |
| H-plane | | | | | | |
| | Lower band | | | Upper band | | |
| f (GHz) | 127.59 | 129.46 | 135.38 | 141.21 | 142.65 | 144.65 |
| Main Lobe Magnitude (dBi) | 5.95 | 1.39 | 4.03 | 5.6 | 4.45 | 5.38 |
| Main Lobe Direction | $0.0^o$ | $12.0^o$ | $21.0^o$ | $34.0^o$ | $55.0^o$ | $53.0^o$ |
| 3 dB Angular width | $36.5^o$ | $63.3^o$ | $26.6^o$ | $28.2^o$ | 35.9 | $25.5^o$ |
| Side Lobe Level (dB) | -5.0 | -12.0 | -4.4 | -10.5 | -1.5 | -0.7 |

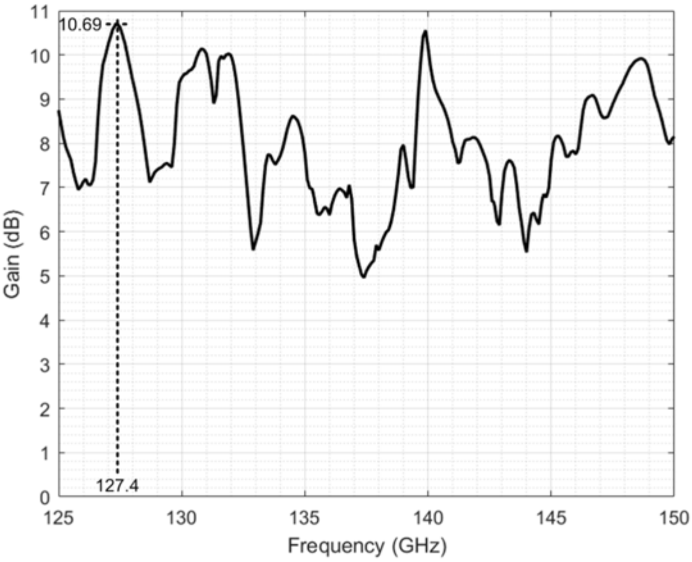

Figure 4.12: Simulated gain of the proposed dual-band antenna

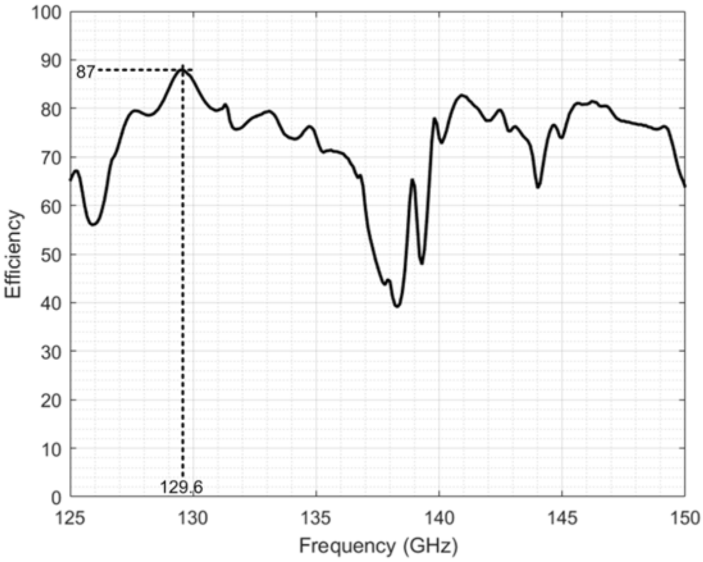

Figure 4.13: Simulated radiation efficiency of the proposed dual-band antenna

## 4.4 Design of a high-gain and wideband SIW-fed DRA

A dual-band antenna design was presented in section 4.3. The design exhibits a stop band of 3.17 GHz between the lower and upper passbands. This stop band indicates poor input impedance of the antenna between 136.5 GHz and 139.67 GHz. This section proposes the modification of the dual-band antenna through the use of impedance matching techniques and parameter optimization to improve the matching in this stop band. This way, the lower and upper passbands of the dual-band antenna are merged together to achieve a wideband operation. The design process involves the systematic and sequential application of impedance matching techniques in order to transform the dual-band antenna into a wideband antenna design.

### 4.4.1 Antenna design

In this section, we describe the design details of the proposed antenna, composed of the SIW feed network and the DR element. Fig. 4.14 shows the geometry of the SIW-fed DRA. The SIW feed is preferred because of its low-loss, high-power handling and its ability to minimize radiation by confining the electromagnetic wave within the waveguide. The laminate is chosen from RT Duroid 5880 material of relative permittivity $\epsilon_r = 2.2$, loss tangent $\delta = 0.0009$ and substrate height $h = 0.254\ mm$. Two rows of metal via separated by a center-to-center distance of $W_{SIW}$ form the lateral walls of the guiding structure for the propagating electromagnetic wave. The via diameter $d$ and pitch $s$ are bounded by the relations: $s \leq 2d$ and $d \leq \lambda_g/5$, where $\lambda_g$ is the guided wavelength. These conditions are sufficient to minimize radiation loss along the walls and to avoid the bandgap effect [91]. The SIW is fed from a 50Ω microstrip line through a linearly tapered section of length $L_t$ and width $W_t$. This tapered transition realizes the conversion of the quasi-TEM wave in the microstrip line to the $\mathrm{TE}_{10}$ mode in the waveguide [121], [135]. This length and width are optimized to minimize reflection [130]. The far end of the SIW is terminated by equally spaced vias, to form the feeding cavity. A rectangular slot is etched on the top conductor of the SIW. This slot couples energy from the cavity to excite the DR element.

A rectangular-shaped DR element is chosen from 99.5% alumina dielectric material of dielectric constant $\epsilon_{rd} = 9.9$. The physical dimensions $L_{dra}$, $W_{dra}$ and $H_{dra}$ are selected such that the DR operates in higher-order modes. The resonant frequencies can be predicted from the equation of the dielectric waveguide model given by equations (2.19) - (2.23) [60].

A pair of inductive vias of diameter $d_2$ is embedded in the SIW feeding structure along the axis of longitudinal symmetry, at positions $y_1$ and $y_2$ from the waveport feed. These create discontinuities in the waveguide for impedance matching. In addition, a thin microstrip strip spanning a length of $L_{stub}$ and width $W_{stub}$ is symmetrically etched at the base of the tapered transition to form a dual-stub. Further improvement is achieved by placing the DRA at an offset distance $x_d$ with respect to the slot axis.

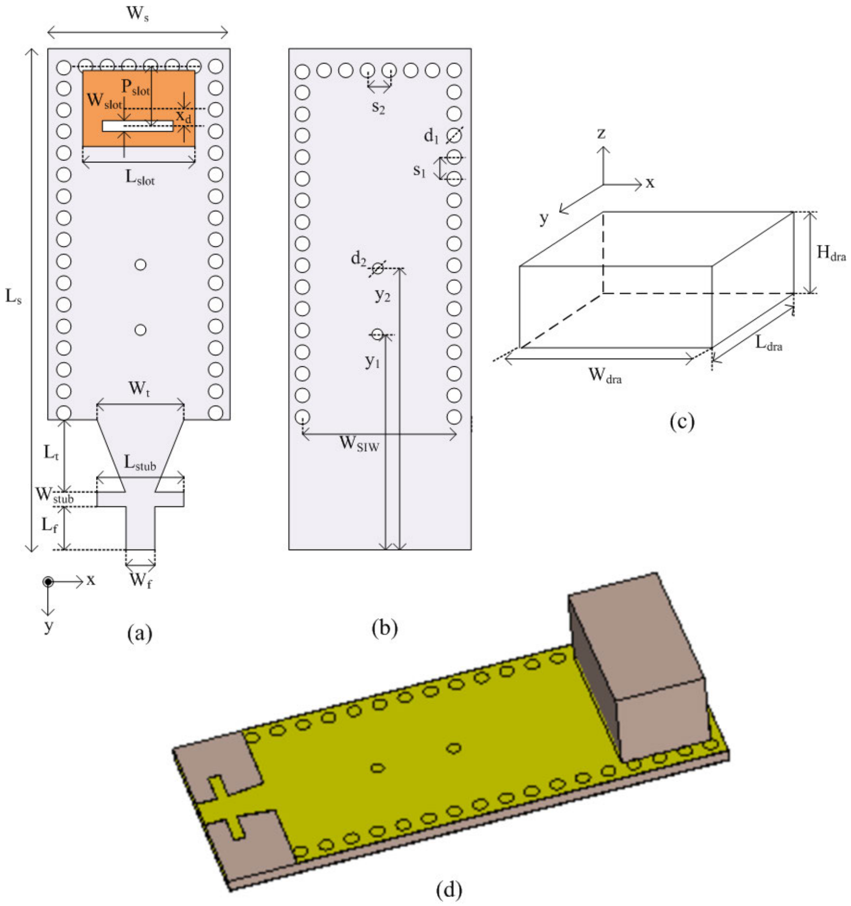

Figure 4.14: Geometry of the proposed wideband SIW-DRA antenna showing (a) top plane (b) ground plane (c) the DR element and (d) 3-D model

### 4.4.2 Simulated results and performance analysis

The proposed antenna structure is modeled in CST Microwave Studio and simulated for optimum performance. Table 4.4 shows the dimensional parameters of the proposed SIW-DRA. The simulated $S_{11}$ performance of the proposed design is depicted in Fig. 4.15. The antenna operates between 123.97 GHz and 152.13 GHz. This represents an impedance bandwidth of 20.39% at the center frequency of 138.05 GHz. The $S_{11}$ plot shows eight distinct resonances within this frequency band. Each of these resonant frequencies is associated with a mode defined by a unique field pattern.

Electromagnetic energy in the SIW cavity is coupled to the DR element through the slot opening beneath it. The slot behaves like a magnetic current source, which excites the fields inside the DR. The excited field distributions inside the DR constitute the different excited modes, each of which is associated with a frequency of resonance. The different modes that can be excited depend on the feeding method employed as well as the point of application of the excitation. These modes may be approximated using the field distribution of the modes of an isolated DR element. These modes can be determined from the eigenmode simulation of an isolated DR element in CST MWS. The excited modes are identified from the orientation of the equivalent magnetic dipole and the number of

Table 4.4: Dimensional parameters of the proposed SIW-DRA

| Parameter | Description | Value | Parameter | Description | Value |
|---|---|---|---|---|---|
| $d_1$ | SIW via diameter | 0.3 | $s_2$ | Terminating via pitch | 0.53 |
| $d_2$ | Inductive via diameter | 0.27 | $W_{dra}$ | Resonator width | 3.455 |
| $h$ | Substrate height | 0.254 | $W_f$ | Feed width | 0.67 |
| $H_{dra}$ | Resonator height | 1.795 | $W_s$ | Substrate width | 4.3 |
| $L_{dra}$ | Resonator length | 1.945 | $W_{SIW}$ | Effective SIW width | 3.7 |
| $L_f$ | Feed length | 0.45 | $W_{slot}$ | Slot width | 0.35 |
| $L_s$ | Substrate length | 10.91 | $W_{stub}$ | Stub width | 0.25 |
| $L_{slot}$ | Slot length | 1.8 | $W_t$ | Taper width | 0.88 |
| $L_{stub}$ | Stub length | 2.0 | $x_d$ | DRA offset position | 0.61 |
| $L_t$ | Taper length | 0.8 | $y_1$ | Position of inductive Via1 | 3.86 |
| $P_{slot}$ | Slot position | 1.55 | $y_2$ | Position of inductive Via2 | 5.53 |
| $s_1$ | Via pitch | 0.56 | | | |

All dimensions are in *mm* units

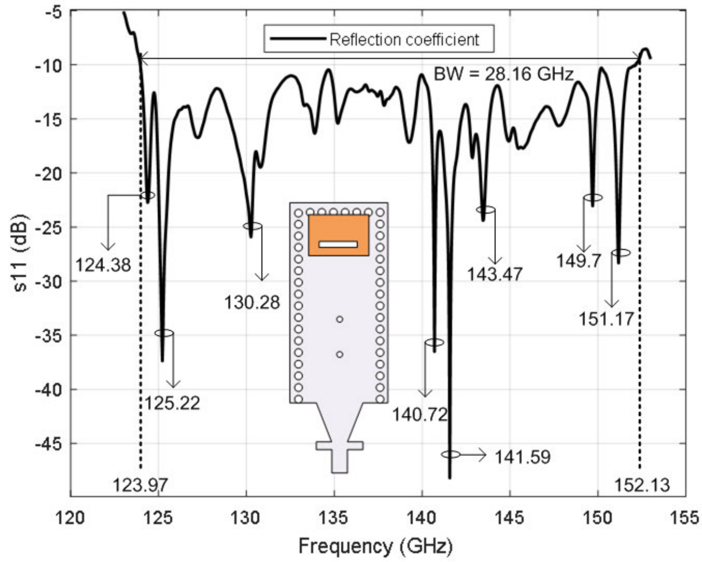

Figure 4.15: Simulated reflection coefficient of the proposed SIW-DRA antenna

half-wave variations of the $E$- and $H$-fields in the orthogonal coordinate system. Because of the presence of the ground plane, it is observed that even modes in the $z$-direction are not excited [60]. Fig. 4.16 shows the $E$-fields of the modes of the isolated DRA at different frequencies, corresponding to the resonating frequencies of the proposed antenna. The excited modes are identified as $TE_{\delta 19}$ at 124.38 GHz, $TE_{5\delta 7}$ at 125.22 GHz, $TE_{\delta 37}$ at 130.28 GHz, $TE_{3\delta 7}$ at 140.72 GHz, $TE_{\delta 55}$ at 141.59 GHz, $TE_{8\delta 7}$ at 143.47 GHz, $TE_{\delta 1-11}$ at 149.7 GHz and $TE_{5\delta 7}$ at 151.17 GHz.

The wideband response observed in Fig. 4.15 is due to the merging of individual resonant frequencies of the higher-order modes. Besides the optimization of the feed structure and DR parameters, the use of inductive metal vias, tuning stub and offsetting of the DR element are employed to improve impedance matching. These techniques are

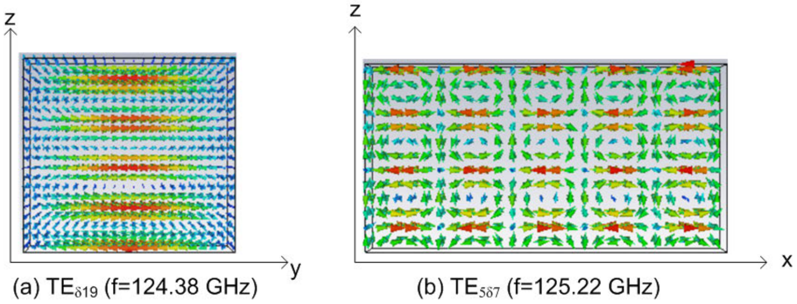

(a) $TE_{\delta 19}$ (f=124.38 GHz) (b) $TE_{5\delta 7}$ (f=125.22 GHz)

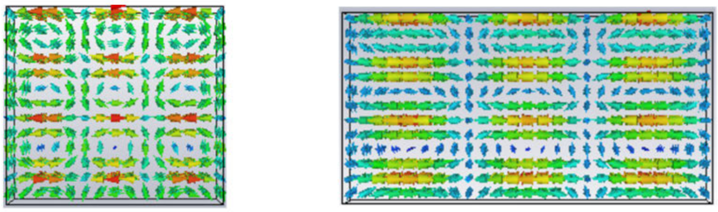

(c) $TE_{\delta 37}$ (f=130.28 GHz) (d) $TE_{3\delta 7}$ (f=140.72 GHz)

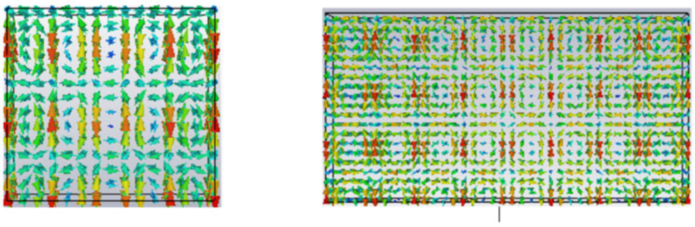

(e) $TE_{\delta 55}$ (f=141.59 GHz) (f) $TE_{8\delta 7}$ (f=143.47 GHz)

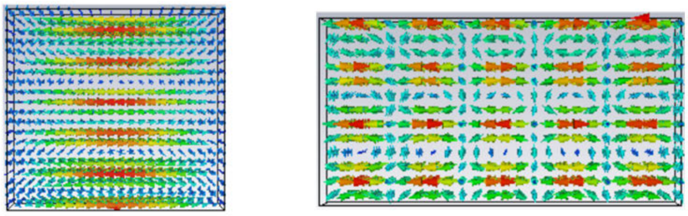

(g) $TE_{\delta 1\text{-}11}$ (f=149.7 GHz) (h) $TE_{5\delta 7}$ (f=151.17 GHz)

Figure 4.16: Simulated $E$-field distributions of the rectangular DRA element showing different modes excited at different resonant frequencies

progressively applied to the design process so as to merge the bands of a dual-band antenna. Therefore, we define intermediate structures representing the evolutionary stages of the antenna design.

Fig. 4.17 shows the top view configurations of these different radiating structures. For convenience, we refer to these structures as Ant. I, Ant. II, Ant. III and Ant. IV respectively. Electromagnetic simulations of these structures are carried out to understand the contribution of the applied impedance matching techniques. Fig. 4.18 shows the reflection coefficients performance comparison of the different radiating structures. $S_{11}$ plots of successive structures are plotted on the same axes to accentuate the contribution of the applied technique.

Fig. 4.18 (a) shows the reflection coefficients of Ant. I, whose structure is the conventional SIW-DRA. The $S_{11}$ parameters show that the antenna can be optimized

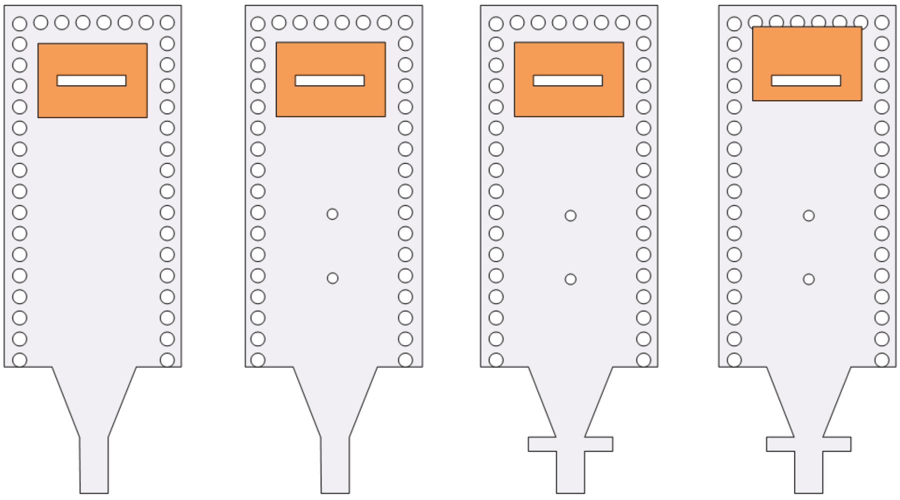

(a) (b) (c) (d)

Figure 4.17: Top view of the different configurations of the antenna showing (a) Ant. I – the conventional SIW-DRA antenna, (b) Ant. II – inductive shorting vias embedded, (c) Ant. III – incorporation of a matching stub and (d) Ant. IV – displacement of the DRA axis

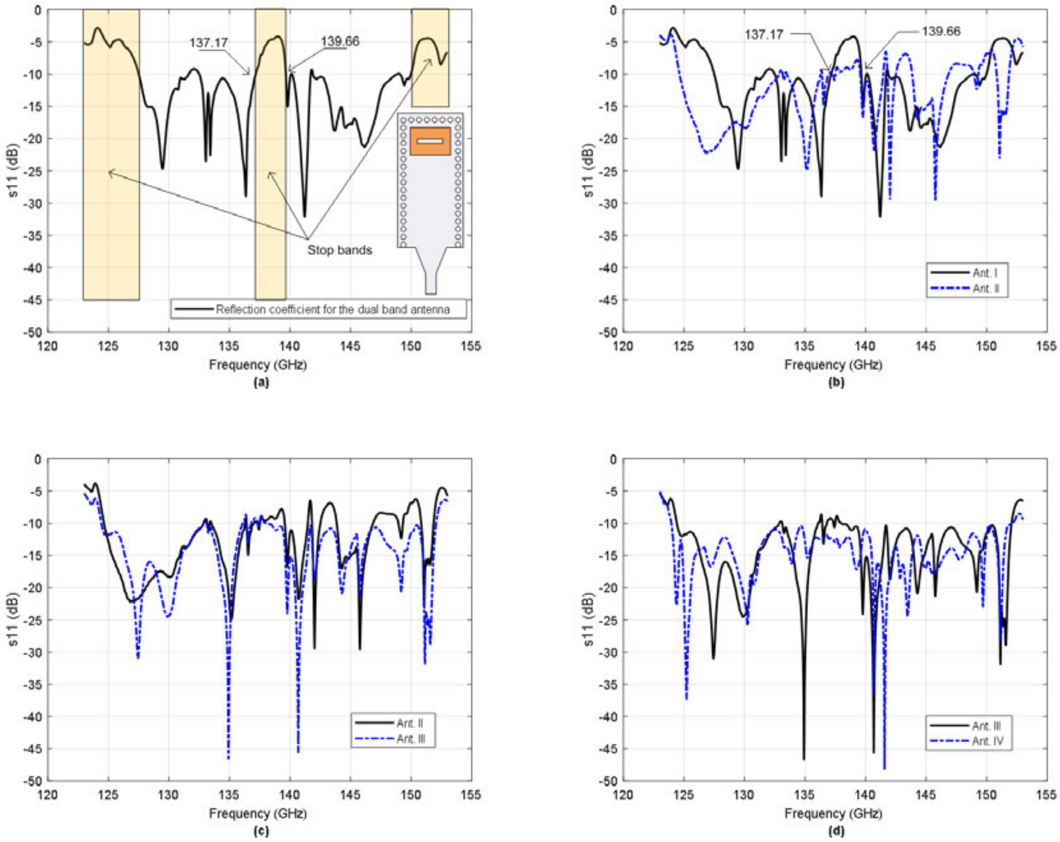

Figure 4.18: Simulated reflection coefficients showing the evolution and performance comparison for different radiating structures (a) dual-band nature of Ant. I with the stopbands highlighted (b) Ant. I and Ant. II (c) Ant. II and Ant. III and (d) Ant. III and Ant. IV

for dual-band applications. The limits of the operating bandwidth and the stop bands are highlighted in the figure. In this work, rather than optimizing the antenna for dual-band applications, we propose to merge the two bands for wideband operation. Ant. I presents a severe impedance mismatch between 137.17 GHz and 139.66 GHz, for which we propose to employ different impedance matching techniques. In the ensuing analysis, we define the lower frequency range of the antenna as $f < 140$ GHz while the higher frequency range as $f > 140$ GHz. We describe the sequential approach to impedance enhancement of the proposed antenna.

#### 4.4.2.1 Effects of the inductive shorting vias

The use of inductive metallic posts and other discontinuities have been employed in conventional metallic waveguides to achieve impedance matching. SIW exhibits propagation characteristics similar to the conventional metallic waveguides, thus the use of inductive vias for impedance matching is extended to SIW structures. Early works in literature [136] reported the application of this technique in the design of a SIW amplifier. Subsequently, it found extensive use in SIW devices for impedance matching. We introduce inductive vias into the SIW structure to merge the dual bands of Ant. I to enhance its bandwidth. The vias may be placed individually or in pairs in the SIW structure. Impedance matching is achieved by proper positioning of the vias, with symmetrical structures showing a wider impedance matching region compared to the asymmetrical structures [137]. Simulations show that the use of two vias offers a better impedance response in the lower frequency range of the antenna compared to a single vias. Fig. 4.18 (b) compares the performance of Ant. I and Ant. II, showing that the via pair cause improvement in impedance matching in the lower frequency range, especially in the desired 137.17 GHz - 139.66 GHz frequency band. This also lowers the lower cutoff frequency of the antenna for broader bandwidth. In addition, there is increased resonance in the higher frequency range, with a slight shift in frequency compared to that of Ant. I. However, we observe that the increased resonance introduces impedance mismatches in the vicinity of these resonances in the higher frequency range. This is indicated by the worsening of the $S_{11}$ performance in the higher frequency range.

Inductive vias discontinuities act like reactive elements along the waveguide. Their presence in the waveguide gives rise to a reflected wave and storage of reactive energy because of the excitation of higher-order propagating modes in the waveguide. However, these modes are evanescent and are localized within the discontinuity, decaying rapidly with distance [138]. The early works of Schwinger and Marcuvitz provided the analysis and modelling of discontinuities in waveguiding structures. In particular, inductive shorting vias can be modelled as a shunt inductor across an equivalent transmission line model [139]. The effect of the inductive via to the input impedance of the proposed design can be observed in Fig. 4.19. In the low-frequency range, it can be observed that the input reactance of the antenna tends to zero, while there is a considerable increase in the inductive reactance in the higher frequency range for Ant. II compared to Ant. I respectively. Similar observations can be made on the resistance plot with reference to 50Ω. In the lower frequency range, the input resistance envelope for Ant. II is close to 50Ω compared to that of Ant. I while it increases in the higher frequency range. This shows an improvement in the antenna impedance match in this lower frequency.

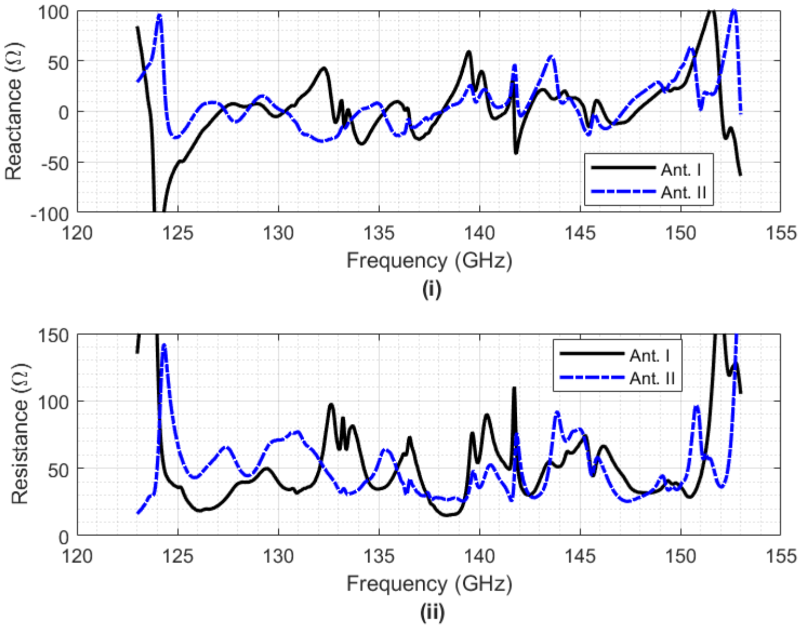

(i)

(ii)

Figure 4.19: Comparison of the simulated input reactance and input resistance for Ant. I and Ant. II

Results of the parametric investigations on the position and diameter size of the inductive metal vias are presented. To distinguish the pair, the vias close to the feed point is designated via 1 while the one close to the DR element as via 2. In Figs. 4.20 (a) and (b), the positions of via 1 and via 2 are varied and its effects on the reflection coefficient analyzed. Parametric results show variations of the reflection coefficient in the lower frequency range. For via 1, the via position $y_1 = 3.81\ mm$ causes a mismatch at 132.8 GHz and $y_1 = 3.91\ mm$ at 126.7 GHz and 137.6 GHz respectively. Similarly for via 2, via position $y_2 = 5.58\ mm$ increases the reflection coefficients beyond -10 dB at 134.7 GHz while $y_2 = 5.48\ mm$ deteriorates the impedance matching performance at 126.7 GHz and 137.6 GHz. The location of the two via-pair affects both the impedance matching in the lower frequency range and the merging of the two bands. Their effects are similar, indicating that the distance of separation of the two vias should be maintained. In Fig. 4.20 (c), an increase in the via diameter $d_2 = 0.3\ mm$ introduces mismatches at 126.7 GHz, 132.7 GHz and 137.7 GHz while a smaller diameter $d_2 = 0.24\ mm$ deteriorates the proposed antenna performance at 127.8 GHz and 140 GHz. Variations of via parameters have a great effect on the merging of the two bands, with increased impedance mismatches being observed in the lower frequencies. The higher frequency range largely remains unaffected.

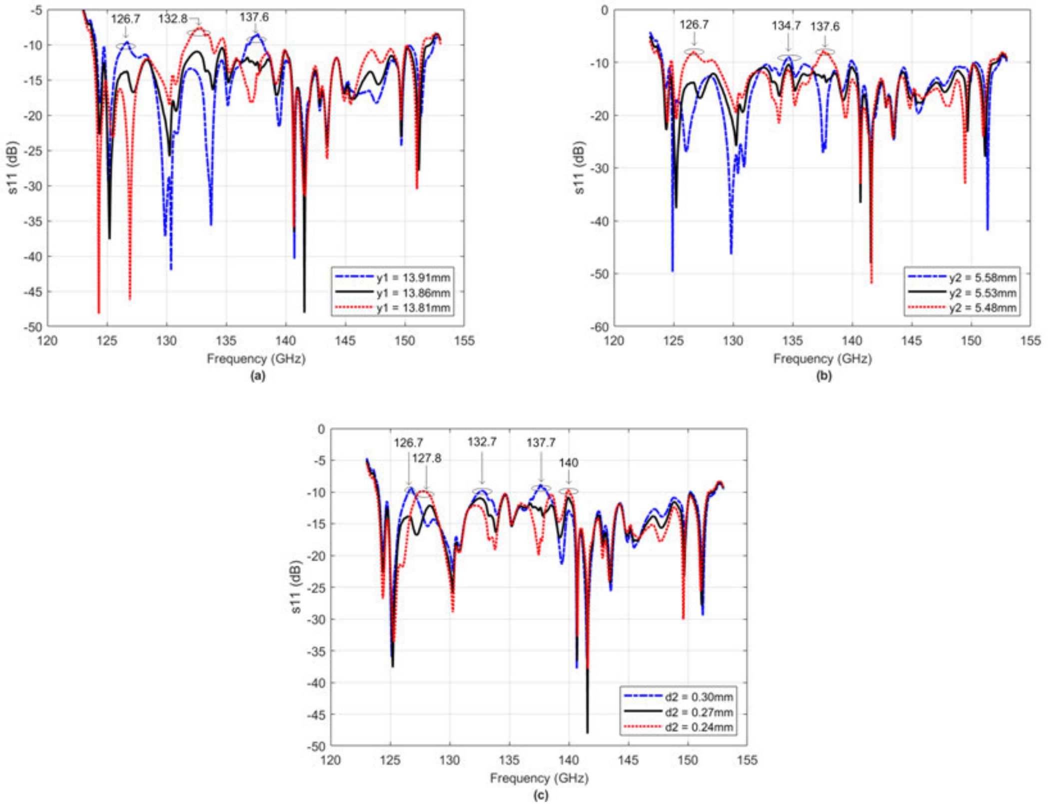

Figure 4.20: Simulated $S_{11}$ plots showing the effects of variation of the different via parameters (a) via 1 position (b) via 2 position and (c) via diameter

#### 4.4.2.2 Effect of the matching stub

Inductive vias cause an increased mismatch in the higher frequency range of the proposed antenna. Fig. 4.18 (c) shows the $S_{11}$ comparison of Ant. II and Ant. III plotted on the same axes. It is seen that the use of a microstrip stub significantly improves the matching in the higher frequency band, without introducing a mismatch in the lower frequency range. Fig. 4.21 shows a plot of input impedance against frequency for Ant. II and Ant. III. It can be observed that there is a reduction in the input inductance of Ant. III compared to Ant. II. The introduction of the matching stub causes a reduction of the input reactance across all the frequencies, indicating the capacitive loading of the stub.

The length and width of the matching stub were varied to determine its effects on the merging of the two bands as well as the impedance bandwidth. Fig. 4.22 (a) shows the $S_{11}$ plots for stub lengths $L_{stub} = 2.1\ mm$, $2\ mm$ and $1.9\ mm$. From the simulated plots, we observe that the stub length does not significantly affect the bandwidth performance of the proposed design. Moreover, there is no shift in the resonant frequencies, except for the poor resonances observed. In Fig. 4.22 (b), the stub width is varied from $0.2\ mm$ to $0.3\ mm$. Reduction of the stub width deteriorates the $S_{11}$ performance at 134.7 GHz in the lower frequency range as well as at 150.2 GHz in the higher frequency range. A wide stub of width $W_{stub} = 0.3\ mm$ does not affect the impedance bandwidth but causes poor resonance at the center frequency. The merging of the two bands is not affected.

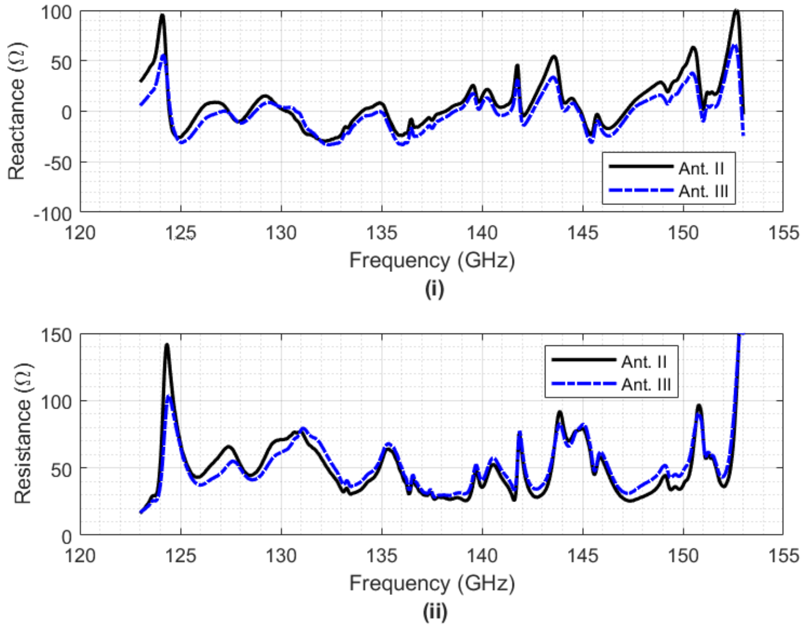

(i)

(ii)

Figure 4.21: Comparison of the simulated input reactance and input resistance for Ant. II and Ant. III

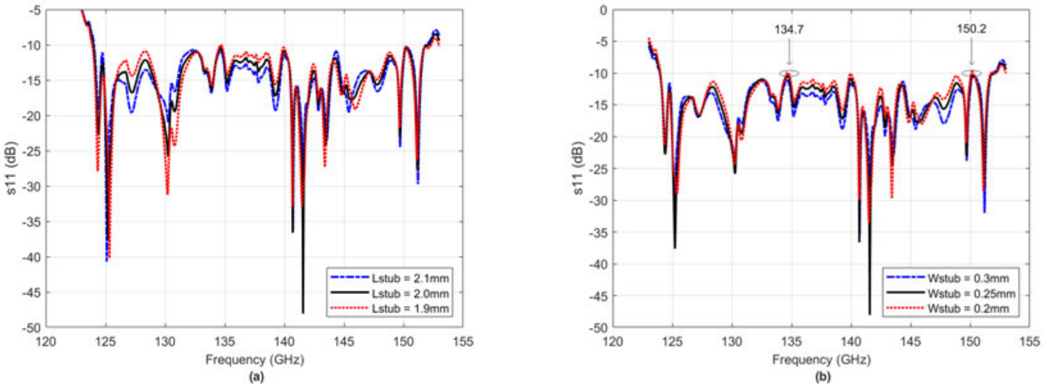

(a)

(b)

Figure 4.22: Simulated $S_{11}$ plots showing the effects of variation of the different stub parameters (a) stub length (b) stub width

#### 4.4.2.3 Effect of the DRA offset position

The slot coupling behaves like a magnetic current source [130]. The level of coupling is adjusted by offsetting the DRA axis with respect to that of the slot. This way, impedance tuning is achieved for better matching. Ant. IV presents the proposed antenna design. The offset DRA further improves the reflection coefficient in the lower frequency band. Fig. 4.18 (d) compares the $S_{11}$ performance of Ant. III and Ant. IV. It is observed that Ant. IV achieves a -10 dB bandwidth from 123.97 GHz and 152.14 GHz. The impedance plots in Fig. 4.23 show that the reactance further approaches zero, indicating improvement in impedance matching of Ant. IV compared to Ant. III. This justifies the offsetting of the DR as a bandwidth enhancement technique.

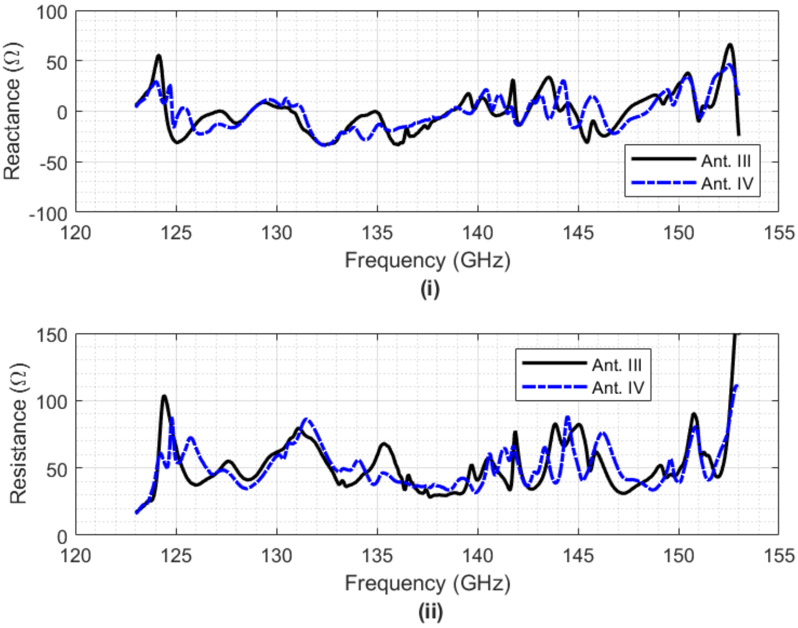

Figure 4.23: Comparison of the simulated input reactance and input resistance for Ant. III and Ant. IV

The DRA offset position affects the coupling of the energy to the DR element. The offset position is varied and simulation results for $x_d = 0.56\ mm$, 0.61 $mm$ and 0.66 $mm$ presented. The parametric variations are presented in Fig. 4.24. A DRA offset position of 0.66 $mm$ introduces a mismatch in both the lower and upper frequency ranges around 135 GHz and 150 GHz respectively. Similarly, for $x_d = 0.56\ mm$ deteriorates the bandwidth performance at 144.4 GHz.

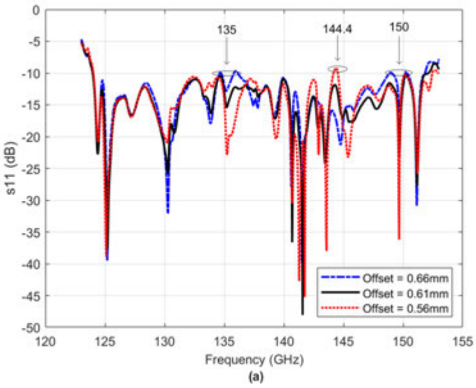

Figure 4.24: Simulated $S_{11}$ plots showing the effects of variation of the DRA offset position with respect to the slot axis

#### 4.4.2.4 Effect of variations of the slot length, slot width and slot position

The use of inductive via, matching stub and offset feeding techniques are applied to the dual-band Ant. I to achieve broadband operation. In addition, the slot also contributes to the bandwidth performance of the antenna. In this section, we analyze the influence of the slot design parameters on the bandwidth response of the antenna. Parametric studies are conducted for optimal parameter selection.

The effects of slot size and position are studied to determine the best coupling to the DR. Fig. 4.25 (a) presents the variation of the reflection coefficient for different slot lengths. Results for the case of $L_{slot} = 1.9$ $mm$, 1.8 $mm$ and 1.7 $mm$ are presented. An increase in the slot length introduces a mismatch in the upper-frequency range, at around 144.2 GHz while a decrease in the length is observed to deteriorate the $S_{11}$ performance of the lower frequency band at 134.7 GHz. The slot length variation causes a change in the magnitude of the reflection coefficient as well as a shift in resonant frequency in the upper-frequency range. The merging together of the two bands remains unaffected. Fig. 4.25 (b) shows the variations in the slot width for $W_{slot} = 0.37$ $mm$, 0.35 $mm$ and 0.33 $mm$. It is noted that the slot width does not significantly affect the impedance bandwidth of the proposed design. We observe an increase in the magnitude of the reflection coefficients at different resonant frequencies for the different values of slot width. However, larger variations in the slot width may introduce mismatches at different frequencies as well as affect the upper cutoff frequency. The variations of the slot position for fixed length and width are shown in Fig. 4.25 (c). The magnitude of $S_{11}$ shows increased impedance mismatch at 134.7 GHz, 140 GHz and 150.2 GHz for $P_{slot} = 1.6$ $mm$, while position $P_{slot} = 1.5$ $mm$ increases the lower cutoff frequency from 123.97 GHz to 124.84 GHz indicating a reduction in impedance bandwidth. Changes in slot position affect the reflection coefficients at the different resonant frequencies, with the best matching at $P_{slot} = 1.55$ $mm$ giving the lowest reflection coefficient of -48.07 dB at 141.59 GHz

The multimode behaviour of the proposed antenna necessitates the study of the antenna radiation characteristics. The radiated fields of the DR can be determined from equivalent currents $\vec{J}_s$ and $\vec{M}_s$ at the surface of the DR element. These current densities may be determined from the knowledge of the fields distribution using Huygens' field equivalence principle [47]. Different modes possess different field distributions which exhibit different radiation characteristics. Merging modes with different radiation characteristics may significantly degrade the antenna radiation pattern in the frequency band of operation. Besides, the excitation of higher-order modes and the use of a finite ground plane cause increase in the cross-polarization of the antenna. The level of cross-polarization is an important figure of merit in the design of antennas because it also leads to the degradation of antenna radiation performance. Simulated 2-D plots of the radiation pattern of the proposed design are presented in Figs. 4.26 and 4.27, for the different resonant frequencies. The observed main lobe directions are $41^o$, $40^o$, $47^o$, $2^o$, $1^o$, $4^o$, $33^o$ and $50^o$ for the $E$-plane and $13^o$, $0^o$, $0^o$, $0^o$, $9^o$, $0^o$, $26^o$ and $0^o$ for the $H$ - plane in the increasing order of resonant frequencies respectively. Therefore, the proposed design exhibits stable broadside radiation pattern in the frequency band of operation. This is expected because a higher-order DR radiates like a magnetic multipole, whose radiation pattern has been shown to be broadband in nature [60]. Table 4.5 lists the radiation

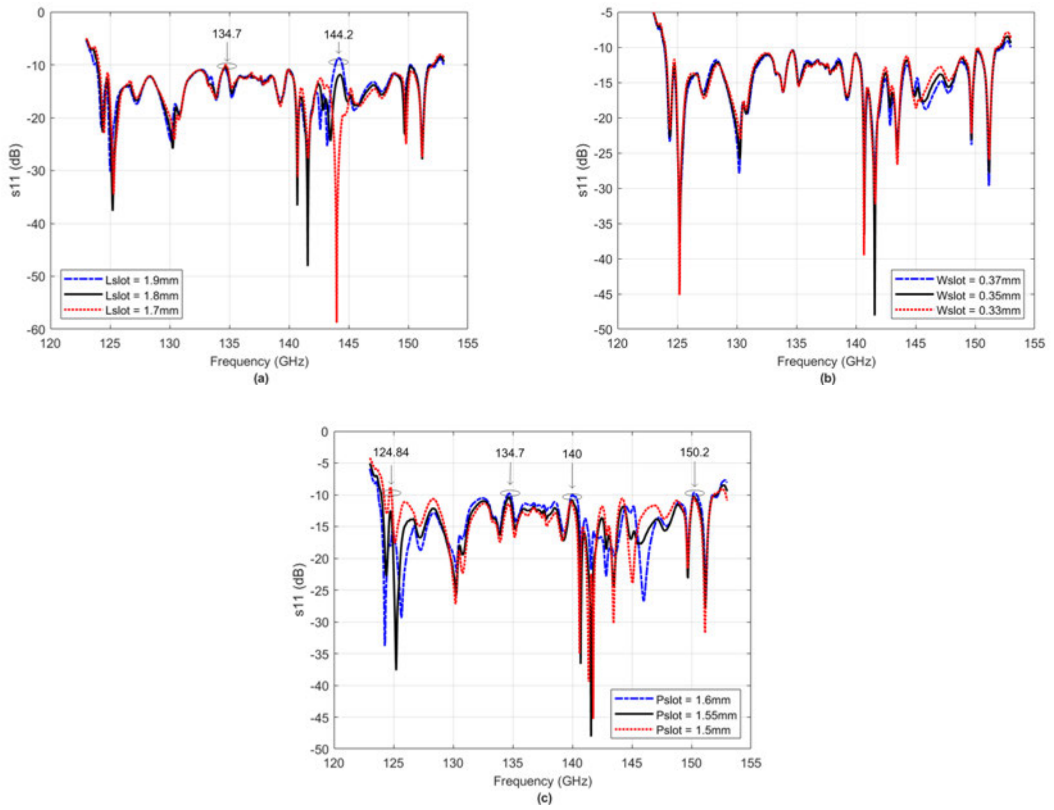

Figure 4.25: Simulated $S_{11}$ plots showing the effects of variation of the different slot parameters (a) slot length (b) slot width and (c) slot position

characteristics of the proposed antenna.

Table 4.5: Radiation pattern characteristics of the proposed SIW-DRA

| f (GHz) | Main Lobe Direction | | Co-polar levels (dB) | | Cross polar levels (dB) | |
|---|---|---|---|---|---|---|
| | E-plane | H-plane | E-plane | H-plane | E-plane | H-plane |
| 124.38 | $41^o$ | $13^o$ | 4.61 | 2 | -95.4 | -8.43 |
| 125.22 | $40^o$ | $0^o$ | 8.96 | 3.29 | -94.6 | -2.3 |
| 130.28 | $47^o$ | $0^o$ | 7.99 | 2.53 | -93.1 | -3.88 |
| 140.72 | $2^o$ | $0^o$ | 9.81 | 8.96 | -90.2 | -0.338 |
| 141.59 | $1^o$ | $9^o$ | 5.96 | 5.77 | -90.5 | -1.46 |
| 143.47 | $4^o$ | $0^o$ | 7.56 | 4.86 | -89.6 | -2.54 |
| 149.7 | $33^o$ | $26^o$ | 5.73 | 2.42 | -88.2 | -1.86 |
| 151.17 | $50^o$ | $0^o$ | 6.85 | 5.55 | -89.1 | 0.534 |

Peak cross-polarized fields are at least 93.93 dBi and 4.28 dBi lower than the co-polarized fields for the E- and H- planes respectively. Low cross-polarization levels can be achieved with the slot axis centered with respect to that of the DRA, because this would suppress modes responsible for increased co-polarization [54]. We would expect the antenna to maintain low levels of cross-polarization, owing to the slot and DRA exhibiting similar magnetic dipole-like radiation characteristics. However, we observe that the levels of the cross-polarization fields are more suppressed in the E-plane while there is poor cross-

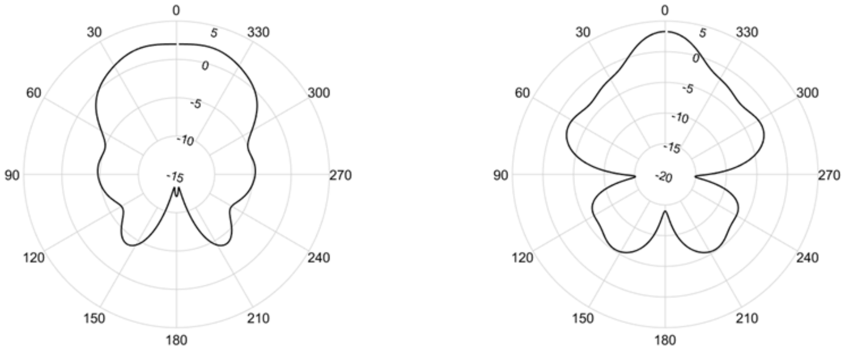

(a) f = 124.38 GHz

(b) f = 125.22 GHz

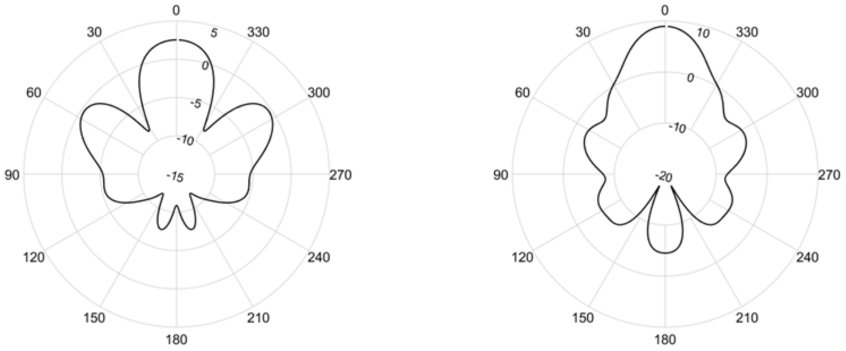

(c) f = 130.28 GHz

(d) f = 140.72 GHz

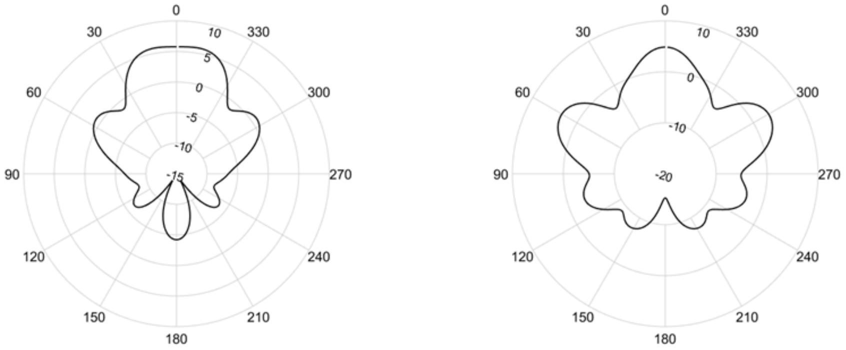

(e) f = 141.59 GHz

(f) f = 143.47 GHz

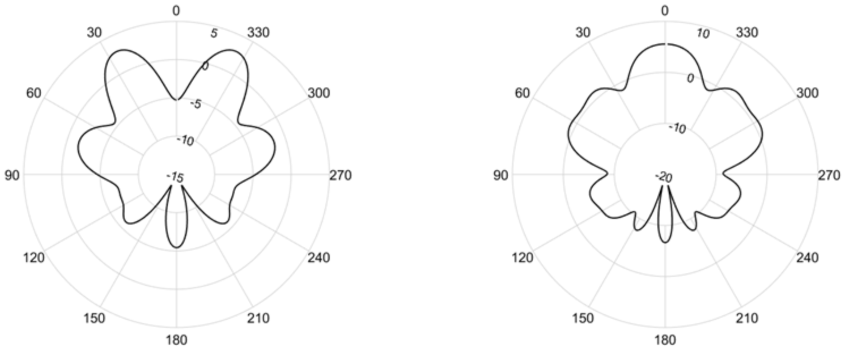

(g) f = 149.7 GHz

(h) f = 151.17 GHz

Figure 4.26: Simulated $H$-plane radiation patterns of the different DR modes at (a) 124.38 GHz, (b) 125.22 GHz (c) 130.28 GHz, (d) 140.72 GHz, (e) 141.59 GHz, (f) 143.47 GHz, (g) 149.70 GHz and (h) 151.17 GHz resonant frequencies

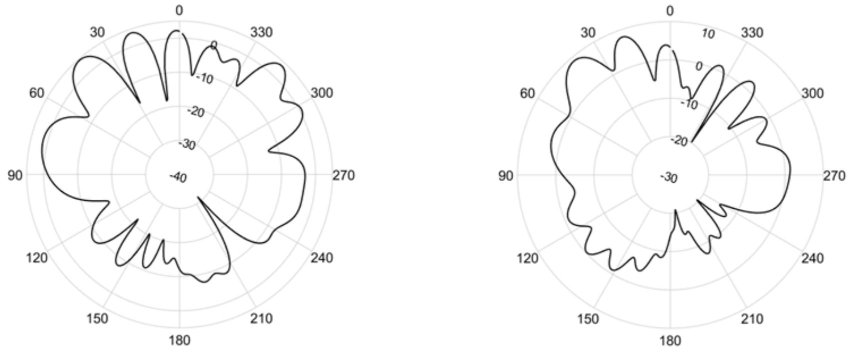

(a) f = 124.38 GHz

(b) f = 125.22 GHz

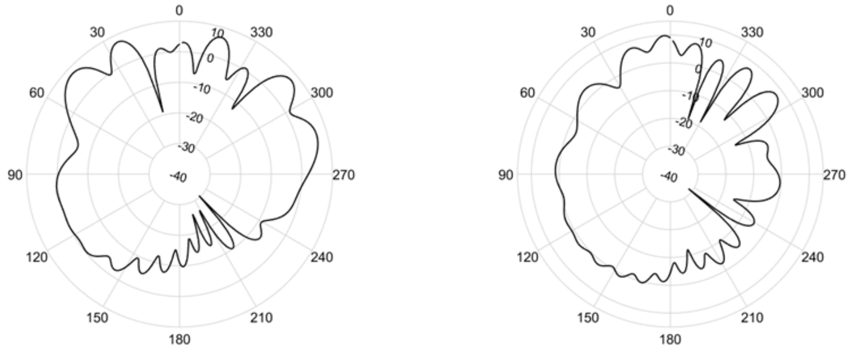

(c) f = 130.28 GHz

(d) f = 140.72 GHz

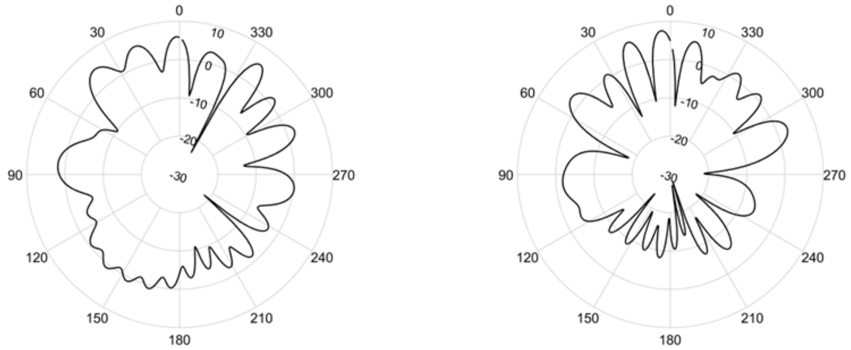

(e) f = 141.59 GHz

(f) f = 143.47 GHz

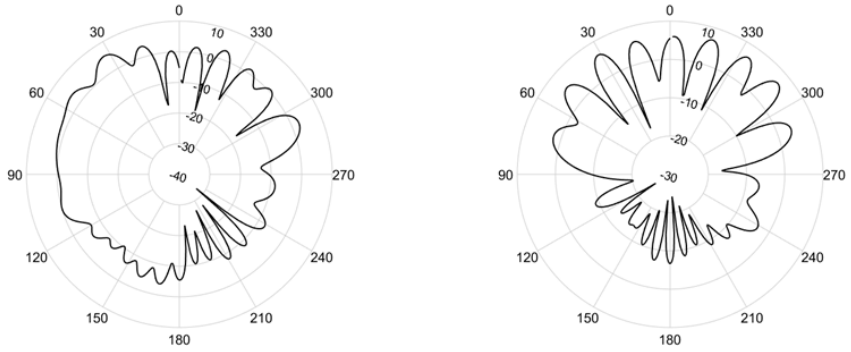

(g) f = 149.7 GHz

(h) f = 151.17 GHz

Figure 4.27: Simulated $E$-plane radiation patterns of the different DR modes at (a) 124.38 GHz, (b) 125.22 GHz (c) 130.28 GHz, (d) 140.72 GHz, (e) 141.59 GHz, (f) 143.47 GHz, (g) 149.70 GHz and (h) 151.17 GHz resonant frequencies

polarization performance in the H-plane. This may be attributed to finite plane effects [127], excitation of higher-order modes of the DR [126] as well as the possible presence of degenerate modes owing to the DRA offset [54]. Fig. 4.28 shows the simulated gain and radiation efficiency of the antenna over frequency. The antenna achieves a simulated peak gain of 11.67 dBi and a directivity of 13.36 dBi at a frequency of 134.2 GHz. The proposed design has a maximum total radiation efficiency of 79% depicted in Fig. 4.29.

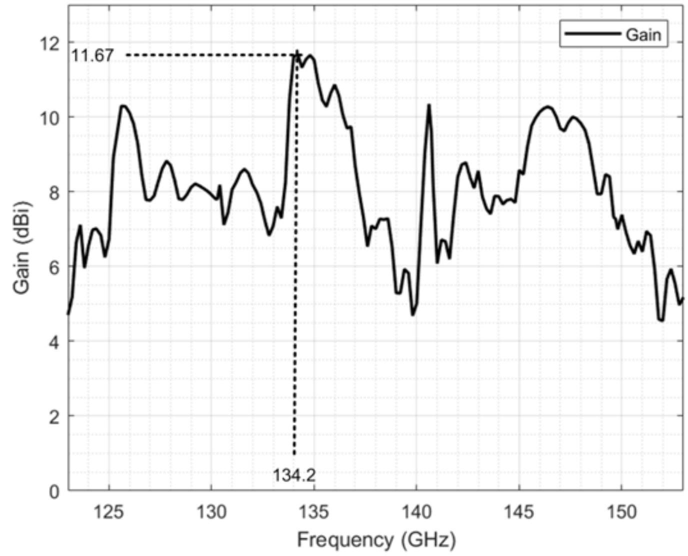

Figure 4.28: Graphs showing simulated gain against frequency

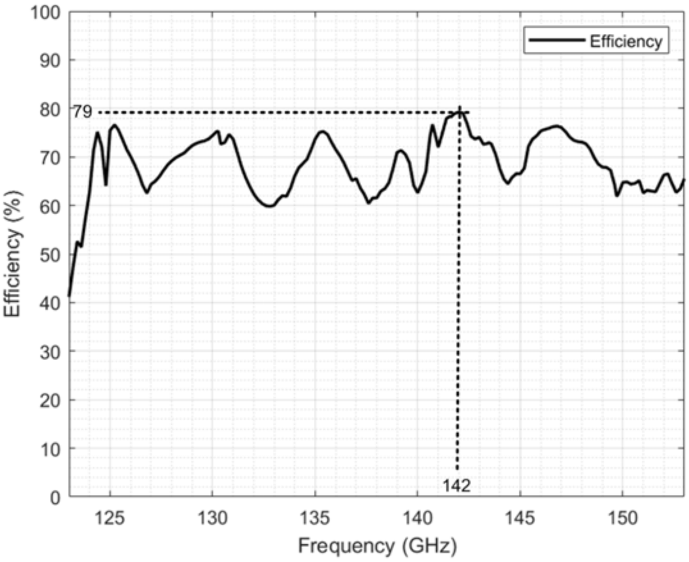

Figure 4.29: Graphs showing simulated radiation efficiency against frequency

### 4.4.3 Design validation

The performance of the proposed design is validated using a different simulation software. The antenna is modelled and simulated in Ansys HFSS environment. HFSS is chosen because it uses a different computational technique compared to CST. Fig. 4.30 is a plot of the simulated reflection coefficients from CST and HFSS simulators, plotted on the same axes for comparison. We observe that the HFSS curve shows a good antenna performance from 125.22 GHz to 150.76 GHz, representing 18.5% bandwidth. We note the deviation from the 20.39% bandwidth reported for CST simulation. This reduction does not significantly impact on the bandwidth performance of the proposed design. The HFSS curve is slightly shifted upwards, with respect to the CST curve. This means that the corresponding higher-order resonances are also shifted. From the two curves, we also observe differences in the level of reflection coefficients at all frequencies. These differences are attributed to the different computational techniques of CST and HFSS.

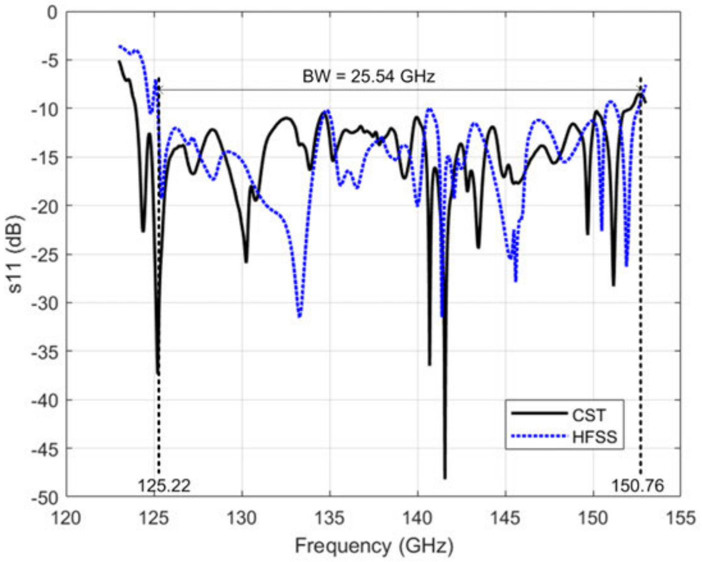

Figure 4.30: Performance comparison of the simulated reflection coefficients of the proposed design in CST and HFSS

The proposed design is compared with published works with similar antenna structures. Table 4.6 presents the performance comparison of the proposed design with the earlier works reported in [14], [45], [69], [130], [131], [132], [133], [134], [140] and [141]. There is increased research interest for D-band communications as evidenced by the different antenna designs reported in literature. In order to evaluate the performance of the proposed design, there is need to compare the performance of antennas with similar structure. Therefore, Table 4.6 compares the performance of published SIW-DRA designs across different frequency bands. The impedance bandwidth of the proposed design is lower than that presented in [45] and [132]. However, the design frequencies of [45] and [132] is much lower than that of the proposed design. For the antenna operating in the same frequency band presented in [14], [140] and [141], the proposed design offers improved bandwidth performance. The gain performance of the proposed design is superior to the earlier reported works. However, we note that the radiation efficiency of the proposed design is slightly lower, compared to designs [140] and [141] operating in the same frequency band.

Table 4.6: Performance comparison of the proposed antenna with other published works

| Reference | Type | Feeding | Technique | $f_o$ (GHz) | Bandwidth | Gain | Efficiency |
|---|---|---|---|---|---|---|---|
| [45], 2010 | CDRA | HMSIW | Cross slot feeding | 60 | 24.2% | 5.5 dB | 92% |
| [133], 2014 | RDRA | SIW | Modification of DRA | 35 | 12% | 5 dBi | 94% |
| [14]-Ant 3, 2014 | On-chip RDRA | HMSIW | HOM | 135 | 13% | 3.7 dBi | 62% |
| [69], 2016 | CDRA | SIW | Cross slot feeding | 6.56 | 8.8% | 3.7 dB | - |
| [134], 2018 | CDRA | SIW | HOM | 25.8 | 2.15% | 10.8 dBi | 87% |
| [131], 2019 | RDRA | SIW | Differential $TE_{20}$ feeding | 27.5-28.4 | 3.2% | 4.2 dBi | 86% |
| [132], 2021,Band I | RDRA | SIW | HOM | 24.5-27.5 | 24% | 9.9 dB | 96% |
| [132], 2021,Band II | RDRA | SIW | HOM | 33-37 | 12% | 9.9 dBi | 96% |
| [130], 2021 | RDRA | SIW | Fractal Geometry + HOM | 5.74 | 19.5% | 5.96 dBi | - |
| [140], 2022 | RDRA | SIW | HOM | 141 | 9% | 8.79 dBi | 81% |
| [141], 2022 | RDRA | SIW | HOM | 125.76 | 13.4% | 12.3 dBi | 84% |
| This work | RDRA | SIW | HOM | 141.59 | 20.39% | 11.67 dBi | 79% |

CDRA – Cylindrical DRA, Efficiency - radiation efficiency, HMSIW – Half Mode SIW, HOM – Higher-Order Mode, RDRA – Rectangular DRA

## 4.5 Chapter summary

In this chapter, a method for merging the passbands of a dual-band SIW-DRA antenna to achieve a broad bandwidth is proposed. This involves the application of impedance matching techniques targeting the mismatches in the stop band, without causing deterioration in the passbands. In the development of the systematic approach for bandwidth enhancement, three different designs are presented.

In the first design, a DRA exhibiting dual-band characteristics, with a narrow stop band is presented. The application of inductive vias in the feed structure results in the merging together of the two closely lying bands. Further improvements is achieved using a DGS on the ground plane. The results demonstrate that embedding of inductive vias in the SIW feed structure enhances the DRA bandwidth. In section 3, a dual-band SIW-DRA is presented. The DRA is optimized for dual-band applications through the modification of the slot shape and optimization of the antenna parameters.

A wideband and high-gain SIW-DRA is presented in section 4. The preliminary findings on the use of inductive vias is applied to the dual-band design presented in section 3, for bandwidth enhancement. Besides the inductive vias, a matching stub and DR offsetting techniques are also employed for bandwidth improvement. The passbands of the dual-band antenna are merged together to achieve a wideband operation. The proposed design achieves a simulated -10 dB impedance bandwidth of 20.39%, ranging from 123.97 GHz – 152.13 GHz. The antenna exhibits a peak gain of 11.67 dBi, directivity of 13.36 dBi and radiation efficiency of 79%. In addition, the proposed antenna has stable broadband radiation pattern in the frequency band of operation. Parametric results show that the positions and diameter of the inductive via significantly contribute to the merging of the two bands.

## Chapter 5

# DESIGN OF HIGH-ISOLATION $2 \times 2$ MIMO SIW-DRA USING METAMATERIAL STRUCTURES

### 5.1 Introduction

The previous chapters were devoted to the design of high-gain and wideband single-element SIW-fed DRAs for D-band frequencies. In this chapter, we propose the integration of MIMO technology with wideband antennas for D-band applications. Different MIMO antenna topologies have been designed for applications in the mm-wave band. However, very little information exists in open literature for MIMO designs for frequencies above 100 GHz. The need for high-performance designs at these high frequencies cannot be over-emphasized. Moreover, the designs presented in the previous chapters demonstrate the suitability of the SIW-fed DRA for high-efficiency antennas for D-band applications. Therefore, we propose to design a $2 \times 2$ SIW-DRA MIMO antenna.

We note that SIW-fed DRA MIMO antennas have been proposed in [131], [132] and [142] for application at lower frequencies. In [131] a quad-element $4 \times 4$ MIMO is proposed for application in the 27.5 GHz – 28.4 GHz band. The elements are orthogonally placed with respect to each other to achieve spatial and polarization diversity. Isolation greater than -40 dB is achieved across the entire band of operation. A similar topology is employed in [132] for the design of a dual-band antenna at 24.5 GHz – 27.5 GHz and 33 GHz – 37 GHz, with isolations better than -22 dB and -17 dB in the two bands respectively with no additional isolation techniques. The topologies presented in [131] and [132] do not allow for integration of a high number of antenna elements in a given space. A better topology that allows for increased integration is presented in [142] in which a $2 \times 2$ MIMO-based SIW-DRA with spatial and $180^o$ polarization is proposed for application at 8 GHz – 12 GHz regime with an isolation better than -25 dB. In these designs, mutual coupling reduction is achieved through the use of spatial and polarization diversity techniques.

In this work, the ability of the SIW structure to confine fields within its closed structure is applied in the design of robust MIMO antennas. The MIMO antenna elements are placed at zero inter-element distance to achieve high antenna integration in a given space. Due to lack of circulating ground currents, the causes of mutual coupling are likely due to parasitic and scattering effects of adjacent elements and surfaces. Consequently, a decoupling structure is proposed in the form of a metamaterial wall to rotate the polarization of the spatial fields and minimize their interactions. The design philosophy for both the proposed single-element antenna and the 2 × 2 MIMO antenna, together with the associated decoupling network is presented.

## 5.2 Antenna design

The design details for the single antenna element, the 2 × 2 MIMO structure and the metamaterial-based decoupling wall are presented.

### 5.2.1 Single element antenna design

The geometry of the proposed single-element antenna is depicted in Fig. 5.1. The antenna consists of a DR element placed on top of a SIW feeding cavity. The design of the SIW-DRA is a three-step design process that involves the design of the feed network, the design of the DR element and the application of impedance matching techniques for bandwidth enhancement.

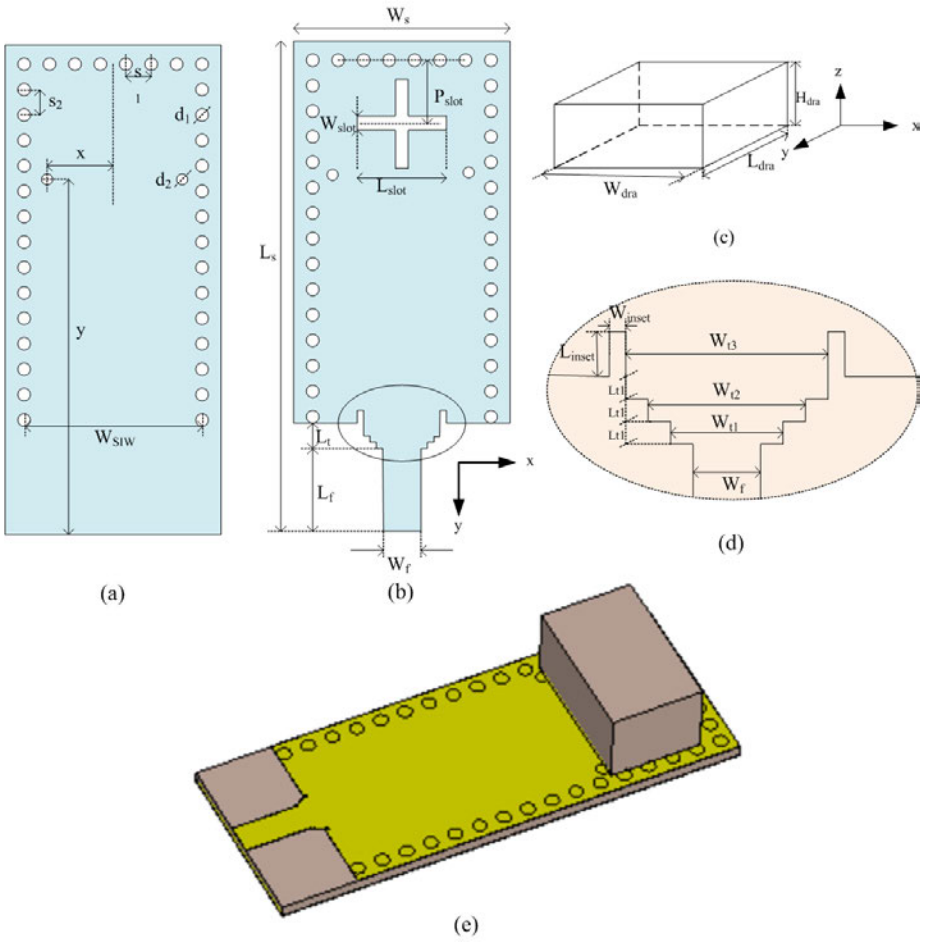

Figure 5.1: Geometry of the proposed SIW-DRA showing (a) bottom view (b) top view (c) DR element (d) inset view of the stepped impedance section and (e) 3-D view

#### 5.2.1.1 Design of the SIW feeding cavity

The SIW feed is designed from RT Duroid 5880 substrate material of relative permittivity $\epsilon_r$ =2.2, loss tangent $\tan\delta$ =0.0009 and substrate thickness $h$ =0.254 mm. The SIW cavity is formed by rows of equally spaced metal via that form the walls of the guide, with one end terminated with a via fence. The design procedure involves the mapping of the dimensions the air-filled conventional RWG to that of a dielectric-filled SIW so that they exhibit similar propagation characteristics at the lowest cut-off frequency for the $TE_{10}$ mode. The via-to-via width of the SIW, $W_{SIW}$ is obtained using equations (2.26), (2.27) and (2.28) [92], [93]. The key design parameters of via diameter, $d$ and pitch, $s$ are selected according to the rules presented in [91] to minimize radiation through the guide walls. In designing the SIW, care should be taken to avoid over-perforation so as not to adversely affect the mechanical rigidity and strength of the SIW. The rule of thumb is choosing $p/\lambda_c > 0.05$. This means that the number of cylindrical vias should not exceed 20 per wavelength [143].

The proper determination these design parameters minimizes the radiation losses through the guide walls. The width of the SIW in equation (2.28) is based on the dominant $TE_{10}$ propagating modes. The feeding cavity is designed to operate in higher-order modes by scaling the SIW effective width to form an oversized waveguide, while maintaining the via diameter and pitch sizes. One end of the SIW is terminated with a fence of equally spaced vias to form a cavity of length $L_{eff}$. SIW structures support the propagation of only $TE_{m0}$ modes because of lack of lateral currents as a result of dielectric gaps formed by the via separations. Therefore, the resonant modes for the $TE_{m0l}$ modes of the resonator are given by [144]:

$$f_{m0l} = \frac{c}{2\pi\sqrt{\varepsilon_r}}\sqrt{\left(\frac{m\pi}{W_{eff}}\right)^2 + \left(\frac{l\pi}{L_{eff}}\right)^2} \tag{5.1}$$

The SIW cavity is designed to resonate at higher-order modes to achieve a wide antenna impedance bandwidth. In order to determine the actual excited modes, the SIW resonator is simulated using CST MWS for the entire D-band. The $S_{11}$ plot in Fig. 5.2 shows that the resonances of the cavity occur at 116.69 GHz, 133.04 GHz, 141.86 GHz and 151.1 GHz. The associated resonant modes were identified from the E-field distribution patterns at the individual resonant frequencies to be $TE_{306}$, $TE_{308}$, $TE_{309}$ and $TE_{3010}$. These results were verified using the theoretical equation and the mode frequencies obtained as 116.44 GHz, 132.90 GHz, 141.96 GHz and 151.44 GHz. The slight shift between the simulated and calculated frequencies is attributed to the loading effects on the cavity.

The SIW is fed from a 50Ω microstrip line, through a stepped impedance microstrip sections. A cross-slot is etched on the upper broad wall of the SIW cavity to couple energy to the DR element. A pair of inductive shorting posts/vias is used for impedance matching of the antenna. Further improvement in the input impedance reflection coefficient is achieved using an inset feed.

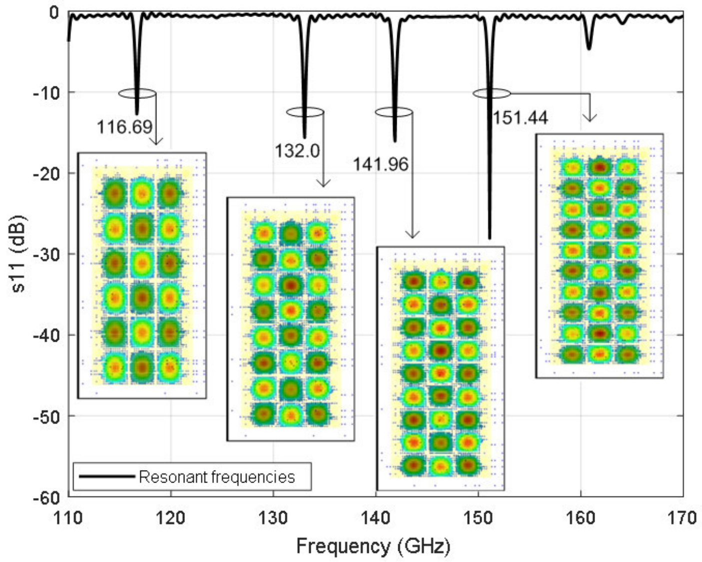

Figure 5.2: Simulated $S_{11}$ of the cavity resonator showing the resonance frequencies and the associated E-field patterns for (a) $TE_{306}$ at 116.69 GHz (b) $TE_{308}$ at 133.04 GHz (c) $TE_{309}$ at 141.86 GHz and $TE_{3010}$ at 151.1 GHz.

#### 5.2.1.2 Design of the DR element

The DR element is chosen from 99.5% alumina dielectric material of relative permittivity $\epsilon_{rd}$ =9.9. A RDRA is preferred because of its high number of free parameters necessary for bandwidth control. The bandwidth performance of a DRA depends on the choice of the permittivity of its material and its physical dimensions. The width ($W_{dra}$), length ($L_{dra}$) and height ($H_{dra}$) of the RDRA are selected to ensure the DRA operates in higher-order modes. The resonant frequency of a particular mode can be predicted by solving the transcendental equation given by equations (2.19) - (2.23) [60].

#### 5.2.1.3 Impedance matching and antenna evolution

When excited in higher-order modes, a DR element exhibits multiple resonances, each of which is associated with a different mode. Wideband operation is achieved by merging adjacent resonance bands through the application of impedance matching schemes to minimize reflections. The proposed design employs multiple impedance matching techniques that include the embedding of metallic shorting posts in the SIW structure, modification of the feeding slot to a cross-slot and the use of a series of stair-shaped impedance converter transition sections to minimize reflections.

The application of the different impedance matching techniques to the conventional SIW-DRA give rise to different antenna configurations. In describing the evolution of the antenna, we describe and investigate four different antenna structures depicted in Fig. 5.3. For convenience, these configurations are labelled Ant. I-IV. The different techniques involve the modification of the feed cavity, and thus for brevity, only the top view of the

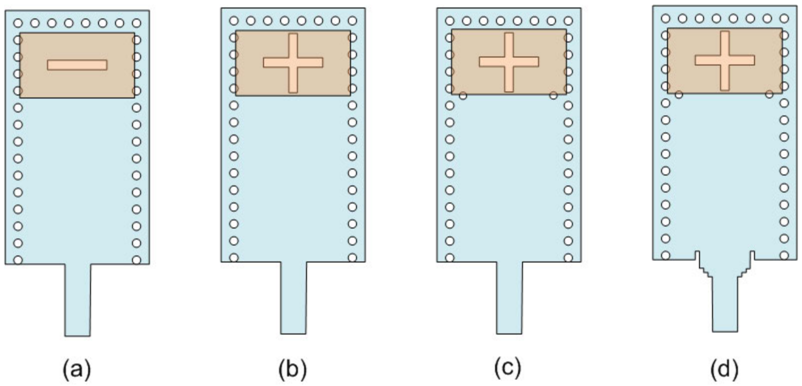

Figure 5.3: Top views showing the evolution of the different antenna configurations for wideband performance (a) Ant. I - the conventional SIW-DRA design, (b) Ant. II - cross-slot feeding aperture, (c) Ant. III - embedded metallic shorting posts and (d) stepped impedance conversion sections

SIW-DRA is shown.

The structure of the proposed conventional SIW-DRA antenna is shown in Fig. 5.3 (a). The antenna is excited from a waveport feed through a 50 $\Omega$ microstrip line and its performance investigated between the frequencies of 135 GHz – 170 GHz. Fig. 5.4 (a) shows the simulated input reflection coefficients of Ant. I, indicating that the antenna suffers severe impedance mismatch around 151 GHz and above 160 GHz. In addition, the plot shows the multi-resonant nature of the antenna as a result of excitation of multiple higher-order DR modes. The antenna could be optimized for dual band operation with bandwidths less than 10% in both bands. However, a broadband antenna is desirable to exploit the high data rate potential of D-band spectrum.

To minimize these mismatch, the feeding aperture is modified to form a cross slot as shown in Fig. 5.3 (b). Slots behave like magnetic current sources for the excitation of the fields inside the DR element [130]. By proper selection of the slot shape and position, efficient coupling of electromagnetic energy can be achieved for improved bandwidth performance. In Fig. 5.4 (b), the reflection coefficients for the Ant. I and Ant. II are plotted on the same axes. It can be observed that the effects of the cross-slot of Ant. II causes improvement in the mismatches exhibited by Ant. I. This is evident from the increased resonances and overall improvement in the reflection coefficients across the entire frequency band. However, the cross slot introduces mismatches around 139 GHz, 141 GHz, 147 GHz and 159 GHz, which cause deterioration in performance at these frequencies.

Further improvements in impedance matching is achieved through the introduction of metal shorting posts into the SIW feeding structure. Fig. 5.3 (c) shows Ant. III, which incorporates a pair of symmetric metal vias placed at a distance $x$ from the longitudinal axis and $y$ from the input port. The inductive vias have been employed in MPAs and SIW filters for performance enhancement. These create discontinuities that act like reactive elements, which gives rise to localized reflections and storage of reactive energy due to the excitation of higher order propagating modes in the SIW [138]. Fig. 5.4 (c) compares the

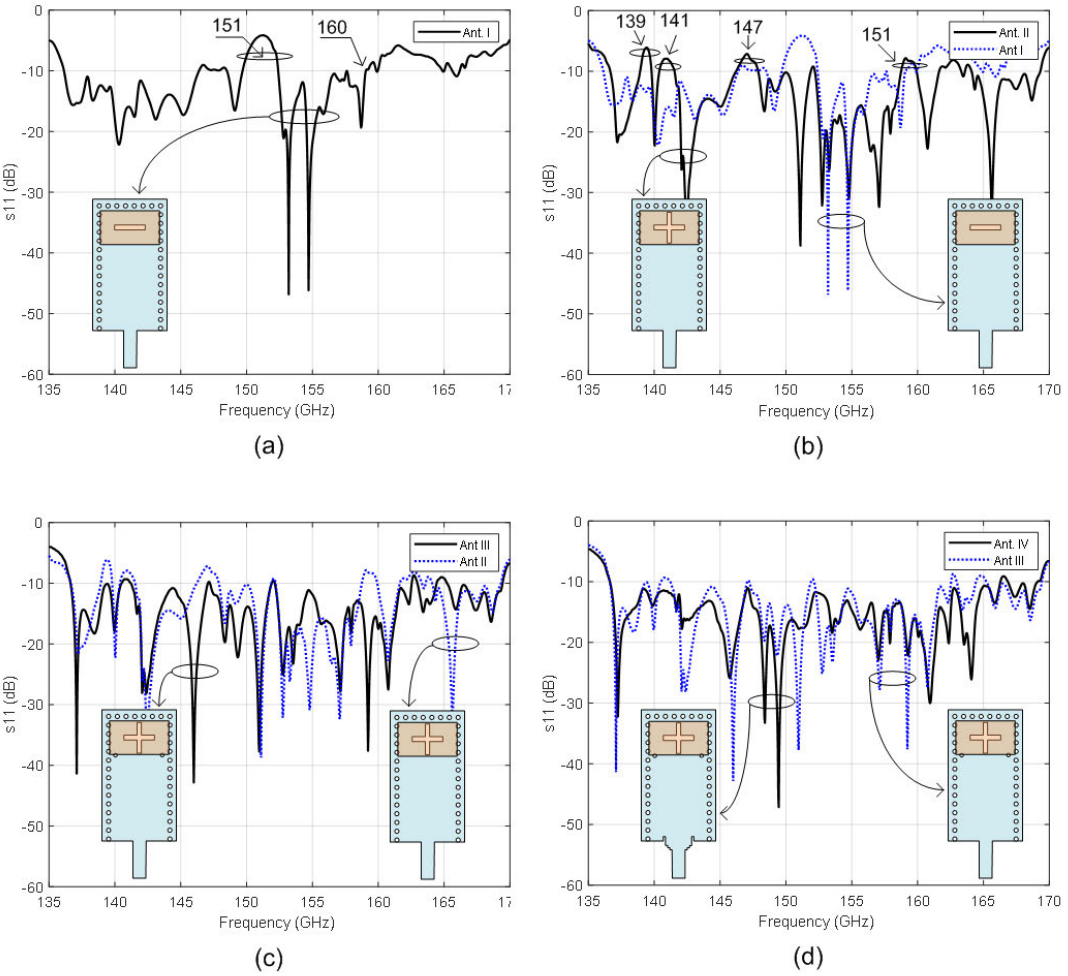

Figure 5.4: Graphs showing the reflection coefficient plots for the different antenna design evolution stages (a) Ant. I (b) Ant. I & II (c) Ant. II & III and (d) Ant. III & IV

input reflection coefficients of Ant. II and Ant. III. From the reflection coefficient plots, it may be observed that the metal shorting posts causes significant improvements in the impedance matching of Ant. III.

The SIW structure is usually connected through a 50Ω microstrip line for integration with other planar components. Sometimes, it is necessary to design a transition between the microstrip line and the SIW for good impedance matching. Simulation results showed that a stepped impedance transition sections offers better matching compared to the commonly used tapered transition. Fig. 5.3 (d) depicts the proposed antenna designated Ant. IV showing a stair-shaped microstrip-to-SIW transition sections. The contribution of this technique to the input impedance matching of the antenna can be observed from Fig. 5.4 (d).

Extensive parametric optimization was performed using CST MWS software to determine the antenna dimensional parameters. The detailed dimensions of the proposed single antenna element are listed in Table 5.1.

Table 5.1: Dimensional parameters of the proposed single element SIW-DRA

| Parameter | Description | Value | Parameter | Description | Value |
|---|---|---|---|---|---|
| $d_1$ | SIW via diameter | 0.3 | $s_2$ | Lateral via pitch | 0.557 |
| $d_2$ | Inductive via diameter | 0.27 | $W_{dra}$ | Resonator width | 3.325 |
| $h$ | Substrate height | 0.254 | $W_f$ | Feed width | 0.67 |
| $H_{dra}$ | Resonator height | 1.625 | $W_{inset}$ | Inset width | 0.05 |
| $L_{dra}$ | Resonator length | 2.065 | $W_s$ | Substrate width | 4.1 |
| $L_f$ | Feed length | 1.48 | $W_{SIW}$ | Effective SIW width | 3.5 |
| $L_{inset}$ | Inset feed length | 0.08 | $W_{slot}$ | Slot width | 0.35 |
| $L_s$ | Substrate length | 10.525 | $W_{t1}$ | $1^{st}$ transition section width | 0.75 |
| $L_{slot}$ | Slot length | 1.8 | $W_{t2}$ | $2^{nd}$ transition section width | 0.84 |
| $L_t$ | Length of stepped transition | 0.24 | $W_{t3}$ | $3^{rd}$ transition section width | 0.95 |
| $L_{t1}$ | Length of each stepped section | 0.08 | $x$ | $x$-position of inductive Via | 1.42 |
| $P_{slot}$ | Slot position | 1.47 | $y$ | $y$-position of inductive Via | 7.66 |
| $s_1$ | Terminating via pitch | 0.5 | | | |

All dimensions are in $mm$ units

### 5.2.2 MIMO antenna design

Fig. 5.5 presents the configuration of the proposed 2 × 2 MIMO antenna. Two single-element SIW-DRAs are placed side by side along the lateral axis, with zero inter-element distance of separation. There is need for MIMO antenna designs to minimize the potential effects of high correlation due to the close packing of antenna elements in limited space in terminal equipment. One possible way is to increase the inter-element distance of separation. This approach is not attractive because it enhances the physical area. The aim of this study is to design a 2 × 2 MIMO antenna with zero inter-element distance of separation. We investigate two MIMO antenna structures: with and without a decoupling network. Figs. 5.5 (a) and 5.5 (b) show the top view and 3-D view of the proposed topology for the case with an integrated decoupling network. The proposed topology is compact and allows for high integration of antenna elements. Improved isolation is achieved by inserting a decoupling network between the two DR elements.

### 5.2.3 Design of the MTMPR wall

The proposed decoupling structure is an MTMPR wall inserted between antenna radiating elements to reduce mutual coupling due to spatial field interactions. This technique is similar to the design proposed in [111] for microstrip-fed DRA MIMO antenna. The MTMPR wall comprises a 1 × 4 array of MTM cells, whose unit cell structure is shown in Fig. 5.6. It is composed of a six-arm modified Gammadion (Swastika) shape etched out on both sides of RT Duroid 5880 substrate material to form a complementary structure. The structure exhibits chirality – geometric property of lack of a mirror symmetry plane [145], while the back-to-back metallic layers have conjugate symmetry. A 1 × 4 array of the unit cell with a periodicity $L_1 = 0.66\ mm$ is inserted between the two DR elements such that its upper edge is aligned with the upper DRA walls in the y-direction, while its bottom is

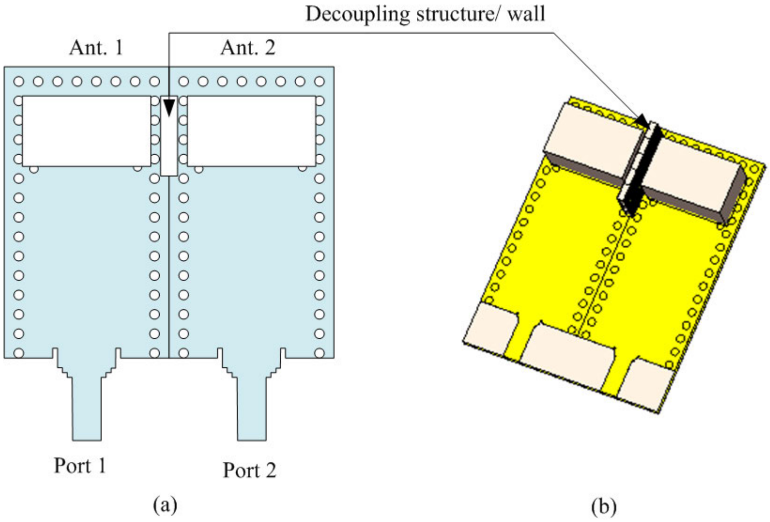

Figure 5.5: Geometry of the proposed 2 × 2 MIMO antenna (a) Top view and (b) 3-D view

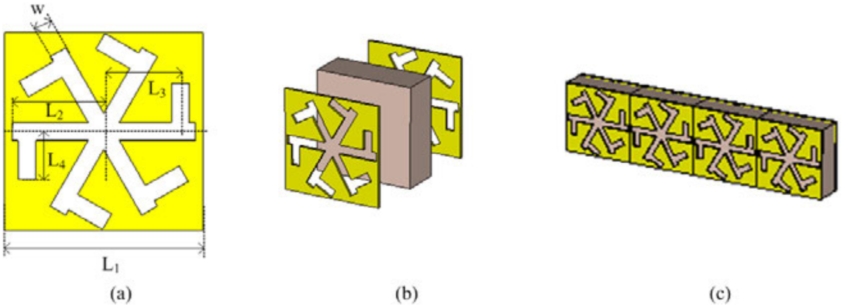

Figure 5.6: Geometry of the proposed MTMPR wall (a) side view of the unit cell, (b) isometric view showing the different layers indicating the conjugate symmetry of the first and third layer of the MTM structure and (c) 1 × 4 array MTMPR wall. The dimensions of the proposed design are as follows: $L_1 = 0.66\ mm$, $L_2 = 0.315\ mm$, $L_3 = 0.255\ mm$, $L_4 = 0.16\ mm$ and $w = 0.06\ mm$

placed at 0.05 $mm$ above the SIW in the $z$-direction.

The MTMPR wall is designed in the transmission mode, such that an electromagnetic signal transmitted through it undergoes a phase rotation, effectively altering its polarization. The transmission characteristics of the MTM structure is determined through the simulation of its unit cell with Floquet port settings. The CST microwave studio was used to simulate the MTMPR unit cell. Fig. 5.7 shows the simulation setup used to investigate the polarization characteristics of the proposed MTMPR wall. The unit cell periodic boundary conditions are applied in the $x$- and $y$-directions while the Floquet port excitations in the positive and negative $z$-directions of the unit cell. The Floquet ports excite two linearly polarized plane waves with orthogonal electric fields, which are represented as $TE_{00}$ and $TM_{00}$ modes. The co-polar and cross-polar coupling between the modes is represented in terms of S-parameters. The reflection coefficients are plotted in Fig. 5.8 (a) showing an operation band of 138.01 GHz – 166.04 GHz.

The co-polarized and cross-polarized reflection components are given by $r_{xx} =$

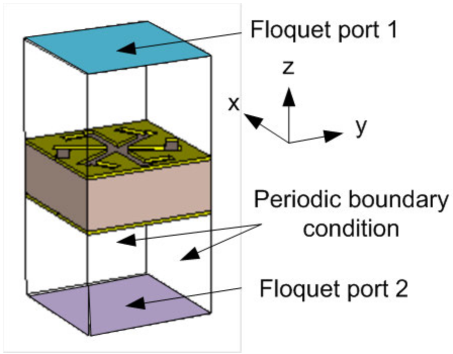

Figure 5.7: Simulation setup of the unit cells to determine the co-polarized and cross-polarized reflection components

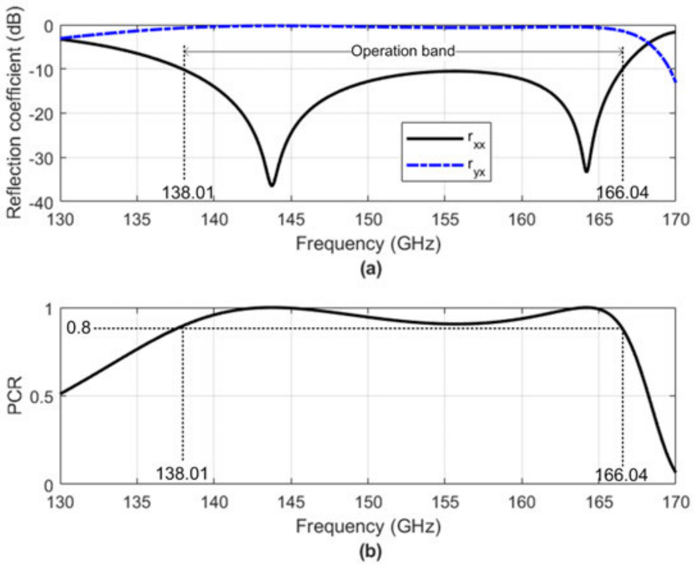

Figure 5.8: Simulation for $x-$polarized incident waves (a) reflection amplitude (b) PCR plot

$|E_{rx}|/|E_{ix}|$ represents reflection from $x-$to$-x$ and $r_{yx} = |E_{ry}|/|E_{ix}|$ represent reflection from $y-$to$-x$. The subscripts $i$ and $r$ represents the incident and reflected polarization state, while $x$ and $y$ represent the electromagnetic wave direction [146]. The polarization efficiency is determined by the polarization conversion rate (PCR). This is defined as the ratio of reflected power in cross-polarized components to the total power in both co- and cross-polarized components and is defined by equation (5.2).

$$PCR = \frac{|r_{yx}^2|}{|r_{yx}^2| + |r_{xx}^2|} \tag{5.2}$$

Fig. 5.8 (b) shows the simulated PCR against frequency, indicating a high value of 80% throughout the band of interest.The PCR is a measure of the efficiency with which the polarization state of the input signal is rotated. A high PCR value of 80% indicates that the MTMPR structure can rotate a linearly polarized wave by $90^o$ with good efficiency.

## 5.3 Results and discussion

The proposed SIW-DRA based MIMO antenna is modeled and simulated in CST MWS environment for performance evaluation. This section presents simulation results for the single and MIMO antenna designs as well as the analysis of MIMO performance metrics.

### 5.3.1 Single antenna element

The simulated reflection coefficient of the single-element antenna is shown in Fig. 5.9. The plot shows a frequency of operation of between 136.68 GHz – 166.28 GHz. This represents an impedance bandwidth of 19.5%. It is observed from the $S_{11}$ curve that the SIW –DRA exhibits multiple resonances. The unique internal field distributions define the different modes of the DR. Therefore, each of these resonances exhibited is associated with the different modes excited. The dimensions of the DR are selected to excite fundamental and higher-order modes. Impedance matching techniques are applied to merge these adjacent resonance bands for wideband operation of the antenna. Matching techniques are progressively applied for performance improvement. Together with the multimode excitation of the DR element, the impedance matching techniques applied include the use of inductive shorting posts, modification of the feeding aperture to a cross slot, use of a series of stepped microstrip feed line sections as well as the use of inset feed.

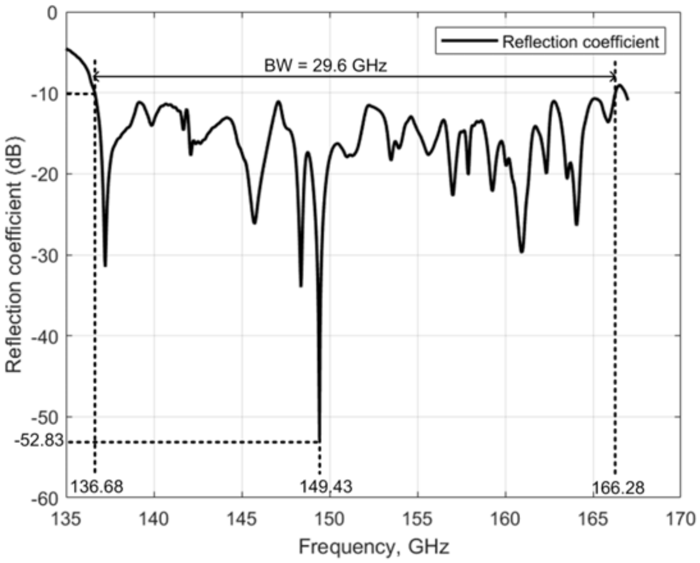

Figure 5.9: Simulated reflection coefficient of the proposed single element SIW-DRA antenna

### 5.3.2 MIMO antenna performance

Two different MIMO antennas, one without and another with the MTMPR wall are designed. The two configurations are investigated and their performances compared.

Because of the zero distance of separation between Ant. 1 and Ant. 2, there is a need to investigate parasitic and scattering effects due to the close proximity of adjacent surfaces on the reflection coefficient of the MIMO antennas. Because of symmetry, the reflection coefficients at ports 1 and 2 are identical ($S_{11}$=$S_{22}$) and only results for port 1 ($S_{11}$) are presented. The simulated $S_{11}$ performances presented in Fig. 5.10, are plotted on the same axes for performance comparison. Simulation results show that the bandwidth performance of the MIMO antenna with no mutual coupling reduction (MTMPR) wall is not affected. However, there is a reduction in the magnitude of the reflection coefficient from -52.83 dB at 149.43 GHz to -35.88 dB at 149.5 GHz. With the MTMPR wall integrated, there is a greater potential for degradation of the reflection coefficient of the MIMO antenna. Simulations show that the degradation due to the MTMPR wall and other adjacent surfaces is mitigated by the proper selection of the size of this decoupling wall and its positioning. A 1 × 4 array of MTMPR unit cells is placed such that the upper edge is aligned with the DRA walls while the bottom is 0.05 *mm* above the SIW structure. Therefore, we observe from the $S_{11}$ plot that the bandwidth performance is not altered by the MTMPR wall. However, there is an increase in the magnitude of the reflection coefficient to -42.68 dB at 137.37 GHz, as compared to the case of no MTMPR wall. In comparing the two MIMO configurations, the MTMPR wall cause improvement in the $S_{11}$ performance, with a potential shift in the upper cutoff frequency (around 166.5 GHz) for bandwidth enhancement.

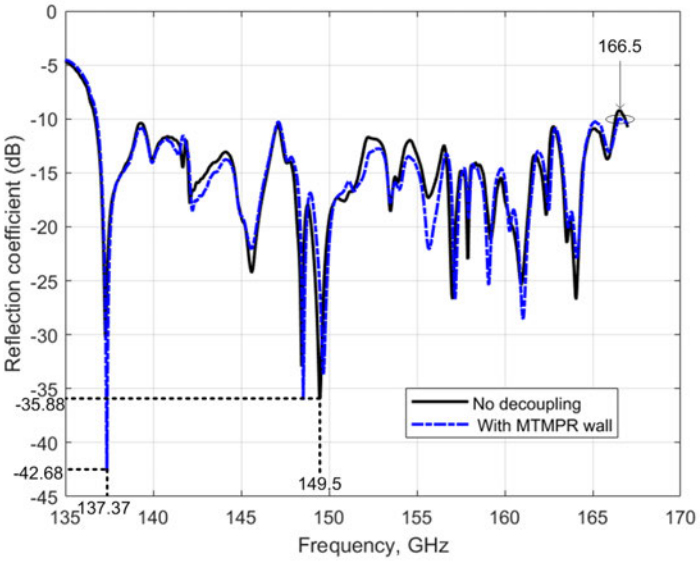

Figure 5.10: Simulated reflection coefficients of the proposed 2 × 2 MIMO antenna with no decoupling applied and with an MTMPR wall

Fig. 5.11 compares the isolation performance of the two MIMO configurations. Due to symmetry, $S_{12}$=$S_{21}$. We observe that the $S_{12}$ performance of the MIMO antenna with no decoupling applied is -19.51 dB. This performance is better than the MPA-based MIMO antennas reported in [105], [106] and [107] for which mutual decoupling techniques have been applied. The SIW confines the electromagnetic energy within its walls. Therefore,

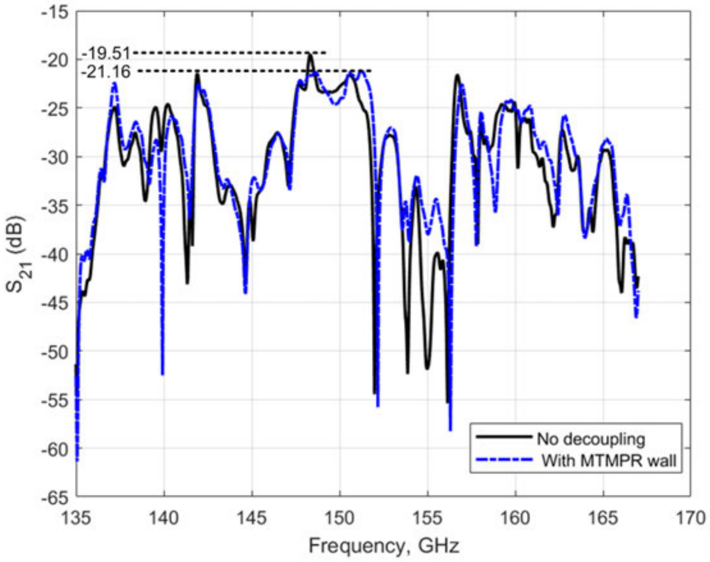

Figure 5.11: Simulated isolation of the proposed 2 × 2 MIMO antenna for the cases with no decoupling applied and with an MTMPR wall

there is minimization of circulating ground currents between adjacent SIW structures, leading to low mutual coupling. This lends SIW-DRA robustness in the design of high-isolation MIMO antennas. This isolation performance is less than the 20 dB, recommended for practical MIMO wireless systems [147].

To enhance the isolation, a decoupling MTMPR wall is introduced between the two DR elements. From Fig. 5.11 it is seen that the isolation performance of the MIMO antenna is improved and its value across the entire bandwidth of operation is greater than 21.16 dB. The MTMPR wall reduces the mutual coupling while maintaining a good impedance matching in the antenna elements.

The improvement in isolation can be explained by understanding the mechanism by which the MTMPR wall alters the polarization of an electromagnetic wave. A linearly polarized wave can be resolved into a sum of a right-hand circularly polarized (RHCP) and a left-hand circularly polarized (LHCP) wave of the same amplitude. An MTMPR wall has a different transmission phase for incident RHCP and LHCP waves, which causes rotation of the polarization plane of a wave transmitting through the wall [111]. The fields from one DR element transmitting to the second undergo a phase rotation as it transmits through the MTMPR wall. Consequently, these transmitted fields have their polarization rotated such that they tend to be orthogonal to the fields of the second DR element. The interaction of orthogonally polarized fields causes a reduction in mutual coupling to enhance isolation.

The improvement in the isolation may further be investigated by studying the surface current distribution on the antenna elements. Because of antenna symmetry, the current distribution for one antenna when the second is terminated in a 50Ω matched load is identical. Therefore, for brevity, the currents in Ant. 1 and Ant. 2 when port 1 is excited while port 2 is matched are presented. Fig. 5.12 presents the simulated surface currents for the two MIMO antenna configurations for three different resonant frequencies of 137.24 GHz, 149.43 GHz and 164.06 GHz. These frequencies are selected to represent the lower, middle and upper bands of the antenna operation.

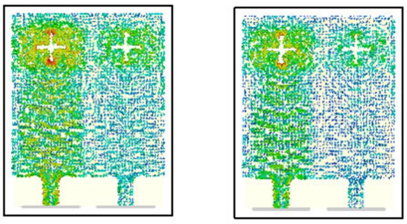

(a) f = 137.24 GHz (b) f= 137.24 GHz

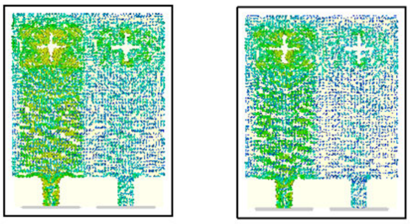

(c) f = 149.43 GHz (d) f = 149.43 GHz

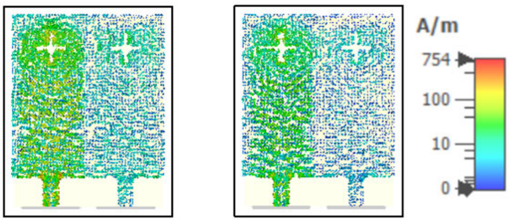

(e) f = 164.06 GHz (f) f = 164.06 GHz

Figure 5.12: Simulated surface currents of the 2 × 2 MIMO antennas at 137.24 GHz, 149.43 GHz and 164.06 GHz.

It is observed that there is a high surface current distribution on Ant. 1, especially near the coupling aperture. This is true for both MIMO configurations at the three resonant frequencies. This is expected because Ant. 1 is the driven antenna, for which energy needs to be coupled to the DR element for good radiation performance. The effect of mutual coupling is evident from the induced surface currents on Ant. 2. This shows that some portion of energy is also coupled to Ant. 2. When the MTMPR wall is placed between the DR elements, the current in Ant. 2 is significantly reduced as observed from Fig. 5.12 (b), (d) and (e), demonstrating the mutual coupling reduction effect of the applied technique.

The simulated 2-D radiation patterns of the proposed MIMO antenna are shown in Fig. 5.13. Only the far-field patterns for Ant. 1 when Ant. 1 is excited and Ant. 2 is terminated in a matched load are presented for the different resonant frequencies. The simulated far-field radiation patterns reveal that the antenna exhibits stable radiation patterns in the broadside radiation. This is expected because different modes of DRs radiate like magnetic multipoles, with broadside radiation patterns [18], [60]. An important requirement is that the radiation patterns of individual modes to be merged should be similar to minimize the degradation of the antenna performance [79].

The radiation patterns of the two MIMO configurations are plotted on the same axes for comparison. It may be observed that the decoupling technique does not significantly affect the radiation pattern in the principle E- and H-planes. Table 5.2 compares the far-field characteristics at the different frequencies.

Table 5.2: Simulated radiation pattern characteristics of the proposed MIMO antennas

| E-plane | | | | | | |
|---|---|---|---|---|---|---|
| | No decoupling | | | MTMPR wall | | |
| f (GHz) | 137.24 | 149.43 | 164.06 | 137.24 | 149.43 | 164.06 |
| Main Lobe Magnitude (dBi) | 10.2 | 5.78 | 9.9 | 10.3 | 6.33 | 9.7 |
| Main Lobe Direction | 9.0$^o$ | 64$^o$ | 13.0$^o$ | 8.0$^o$ | 64$^o$ | 14.0$^o$ |
| Angular width | 28.8$^o$ | 14.7$^o$ | 6.9$^o$ | 28.9$^o$ | 14.8 | 7.0$^o$ |
| Side Lobe Level (dB) | -1.2 | -1.2 | -1.1 | -1.7 | -1.8 | -1.4 |
| H-plane | | | | | | |
| Main Lobe Magnitude (dBi) | 6.8 | 6.44 | 9.97 | 7.04 | 7.11 | 9.97 |
| Main Lobe Direction | 2.0$^o$ | 23.0$^o$ | 7.0$^o$ | 2.0$^o$ | 24.0$^o$ | 7.0$^o$ |
| Angular width | 22.8$^o$ | 31.9$^o$ | 68.8$^o$ | 24.1$^o$ | 23.6 | 59.0$^o$ |
| Side Lobe Level (dB) | -2.7 | -13.4 | -9.3 | -2.9 | -0.7 | -9.3 |

The gain and radiation efficiency of the antenna were also considered. Figs. 5.14 and 5.15 show plots of the simulated gain and radiation efficiency against frequency respectively. The proposed $2 \times 2$ MIMO antenna attains a peak gain of 11.06 dBi and total radiation efficiency of 84%.

### 5.3.3 MIMO diversity performance

The diversity performance of the proposed MIMO antenna is analyzed by evaluating its parameters. Key MIMO performance metrics include the envelope correlation coefficient (ECC), diversity gain (DG), mean effective gain (MEG), channel capacity loss (CCL) and the total active reflection coefficient (TARC). This section presents the MIMO antenna performance metrics.

#### 5.3.3.1 Envelope correlation coefficient

For a practical MIMO antenna, the correlation between the antenna individual elements should be low. ECC provides a measure of the correlation between the elements. A higher value of ECC indicates tight coupling [100]. Two approaches that lend itself useful in the evaluation of ECC is the use of the 3-D radiated fields and that from its scattering parameters. For the proposed $2 \times 2$ MIMO design, ECC is evaluated from the far-field radiated patterns. The ECC between the $i^{th}$ and $j^{th}$ antenna elements is computed from the far field radiated fields using the equation presented in [132], [148].

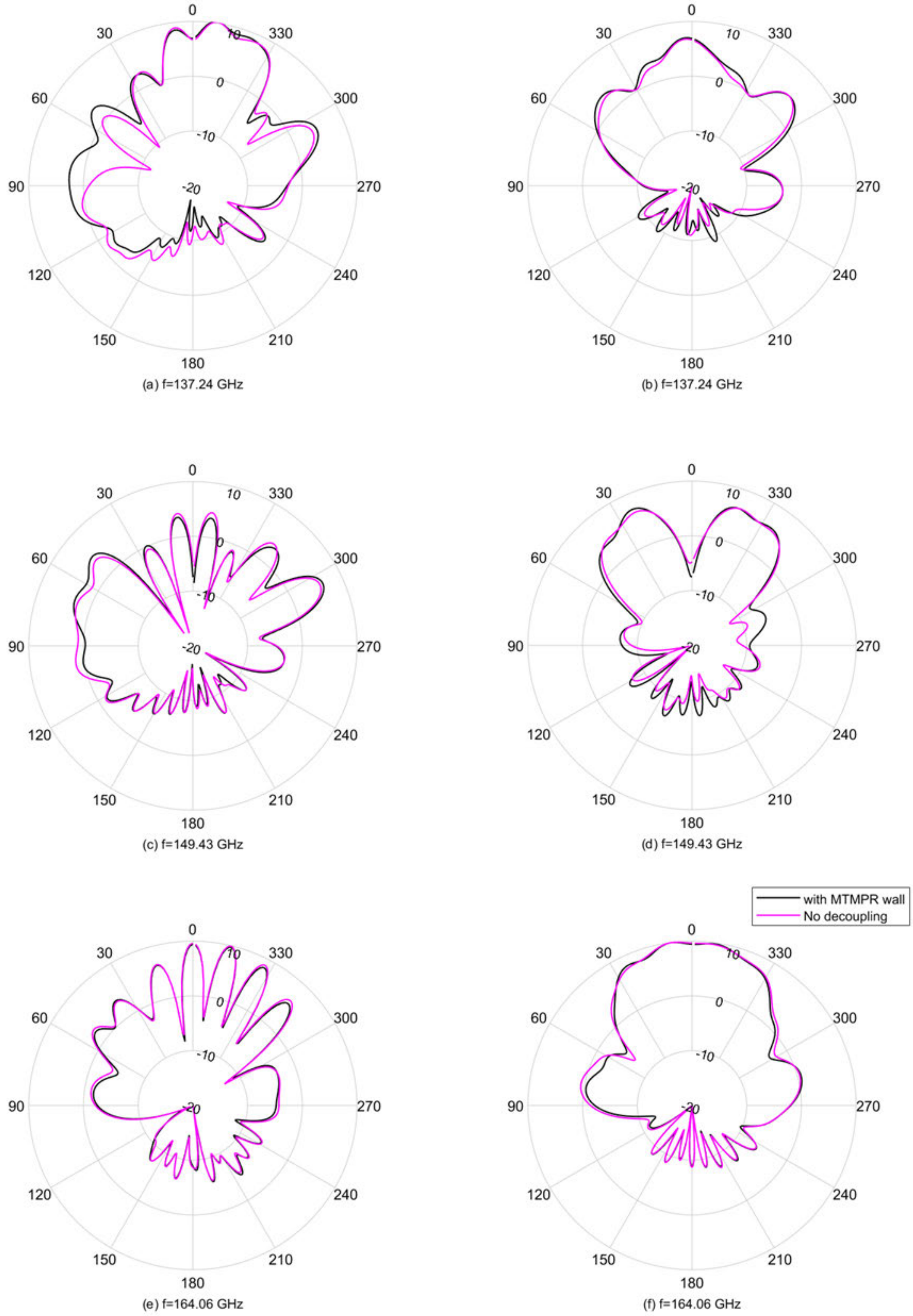

(a) f=137.24 GHz (b) f=137.24 GHz

(c) f=149.43 GHz (d) f=149.43 GHz

(e) f=164.06 GHz (f) f=164.06 GHz

Figure 5.13: Simulated E- and H-plane radiation patterns for the two 2 × 2 MIMO antenna configurations at 137.24 GHz, 149.43 GHz and 164.06 GHz.

$$ECC = \rho_e = \frac{\left| \iint_{4\pi} \left[ \vec{F}_i(\theta,\phi) * \vec{F}_j(\theta,\phi) \right] d\Omega \right|^2}{\iint_{4\pi} \left| \vec{F}_i(\theta,\phi) \right|^2 d\Omega \iint_{4\pi} \left| \vec{F}_j(\theta,\phi) \right|^2 d\Omega} \tag{5.3}$$

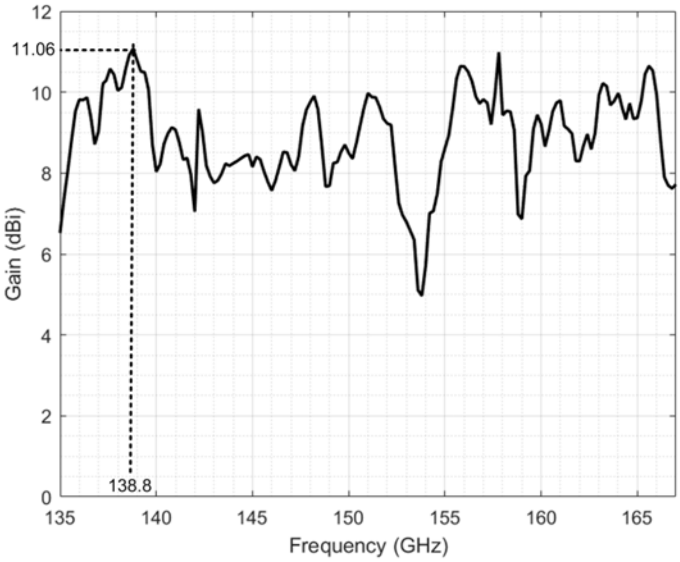

Figure 5.14: Graphs showing simulated gain of the proposed 2 × 2 MIMO antenna.

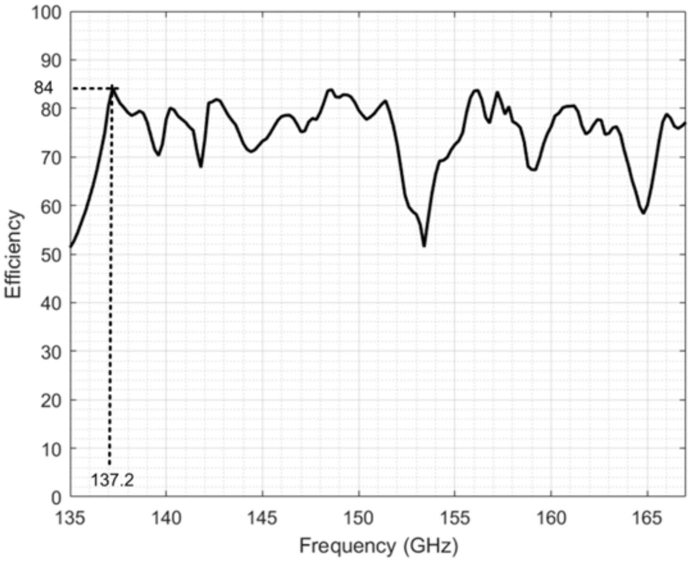

Figure 5.15: Graphs showing simulated total radiation efficiency of the proposed 2 × 2 MIMO antenna.

Where $\vec{F}_i$ and $\vec{F}_j$ represents the radiation pattern of the antenna with ports $i$ and $j$ excited, $*$, the Hermitian product operator and $\Omega$, the solid angle. A plot of the variation of ECC with frequency is shown in Fig. 5.16 (a). It may be observed that within the antenna operating band, the peak value of ECC is 0.008 which is less than 0.5, indicating good MIMO performance [149].

#### 5.3.3.2 Diversity gain

For a MIMO antenna, the DG presents the enhancement of the signal-to-noise ratio of a multiple antenna system over that of a single antenna. This is often calculated from ECC from the expression:

$$DG = 10\sqrt{1-|\rho_e|^2} \tag{5.4}$$

Fig. 5.16 (b) shows the simulated DG of the proposed MIMO antenna. A DG performance between different ports greater than 9.9 indicates improved diversity performance.

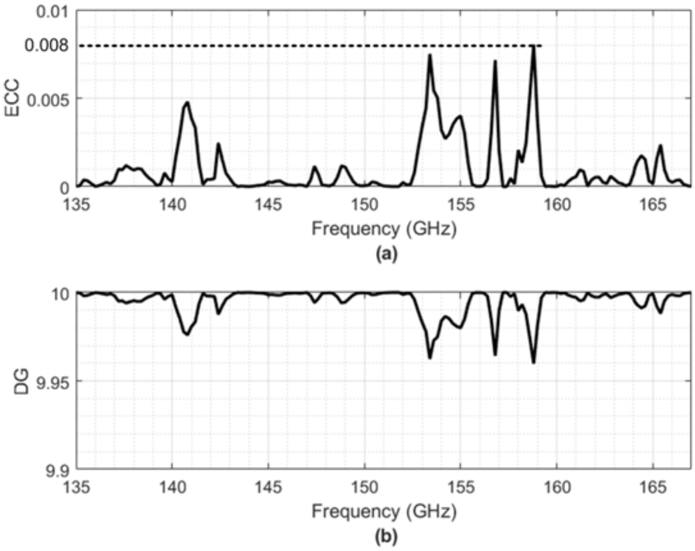

Figure 5.16: Graphs showing (a) ECC curve and (b) DG curve of the proposed 2 × 2 MIMO antenna.

#### 5.3.3.3 Mean effective gain

In multipath fading environments, the mean signal level received over a given path is used to estimate the antenna gain performance. This characterization, referred to as MEG, relates the power received by a multi-port antenna to that of an isotropic antenna [149]. MEG is calculated for each port from the expression:

$$MEG_i = 0.5\left[1-\sum_{j=1}^{M}|S_{ij}|^2\right] \tag{5.5}$$

The measure of similarity of MEG curves is obtained as the ratio $MEG_i/MEG_j$. For a 2 × 2 MIMO, $(i=1, j=2)$. For optimum MIMO performance, this ratio between MEG for the different ports should be less than 3dB [149], which is satisfied in the proposed design.

#### 5.3.3.4 Total active reflection coefficient

Another important MIMO characterization metric is TARC. TARC curves define the effective bandwidth of a MIMO system. For a two-element MIMO, TARC may be calculated from the expression:

$$TARC = \frac{\sqrt{(|S_{11} + S_{12}e^{j\theta}|^2) + (|S_{21} + S_{22}e^{j\theta}|^2)}}{\sqrt{2}} \tag{5.6}$$

Where $\theta$ is the phase angle of the input excitation. The TARC curves shown in Fig. 5.17 are obtained exciting port 1 with a $0^o$ phase input, while that of port 2 was swept from $0^o$ to $180^o$ in steps of $30^o$. The interpretation of Fig. 5.17 is that the operating bandwidth of the proposed $2 \times 2$ MIMO antenna is not severely degraded by phase changes in the excitation ports. This bandwidth robustness lends the proposed design suitable for MIMO applications.

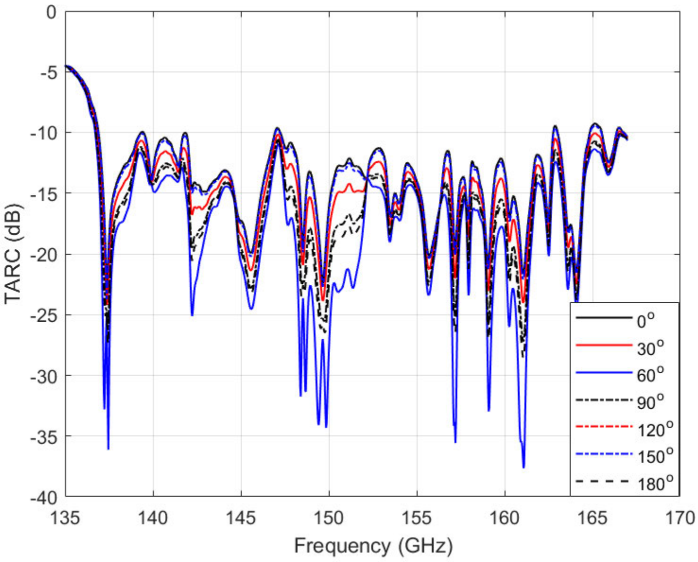

Figure 5.17: Graph showing the TARC curves of the proposed $2 \times 2$ MIMO antenna.

#### 5.3.3.5 Channel capacity loss

CCL indicates the upper bound of reliable signal transmission of a MIMO antenna system. For a $2 \times 2$ MIMO system, CCL is expressed as:

$$CCL = -log_2 det(\Psi^R) \tag{5.7}$$

Where $\psi^R$ is a $2 \times 2$ correlation matrix. The elements can be obtained as $\psi_{ii} = 1 - (|S_{ii}|^2 + |S_{ij}|^2)$ and $\psi_{ij} = -(S_{ii}^* S_{ij} + S_{ji}^* S_{jj})$ [150].

A plot of the capacity loss of the MIMO system is depicted in Fig. 5.18 showing a channel capacity loss below the acceptable limit of 0.4 bits/s/Hz in the 136.68 GHz – 166.28 GHz band of operation. This renders the proposed design suitable for practical MIMO systems [149].

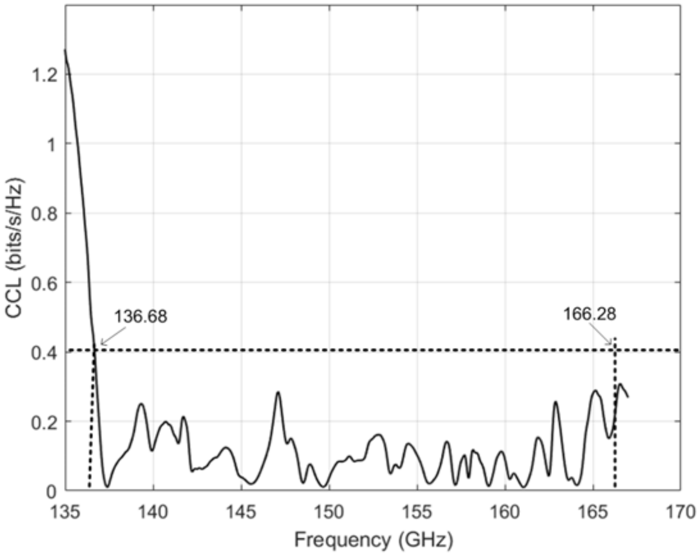

Figure 5.18: Simulated channel capacity loss for the proposed 2 × 2 MIMO antenna.

### 5.3.4 Design validation

The proposed 2 × 2 MIMO design is simulated using Ansoft HFSS software for performance verification and design validation. HFSS and CST electromagnetic simulators employ different numerical computational techniques, *viz,* finite element method and finite integration technique methods respectively. The results of the two softwares are compared for design verification. Fig. 5.19 compares the $S_{11}$ performance curves of the single-element antenna from CST and HFSS.

From Fig. 5.19, it is observed that the bandwidth performance of the HFSS curve is 136.83 GHz - 164.81 GHz, representing 18.6%. There is some little difference in the bandwidth performance as observed from the $S_{11}$ curves of CST and HFSS. However, this deterioration is equivalent to 0.9%, which does invalidate the suitability of the design.

Fig. 5.20 compares the E- and H-fields radiation plots of the proposed 2 × 2 MIMO antenna design when simulated using both CST and HFSS at different frequencies. We observe close similarities between the two radiation plots, depicting broadside antenna patterns.

Fig. 5.21 compares the $S_{21}$ curves obtained from the two full-wave electromagnetic simulators. There is good agreement in the simulated isolation performance between the two simulators.

In addition to these antenna parameters, key MIMO metrics are also determined from

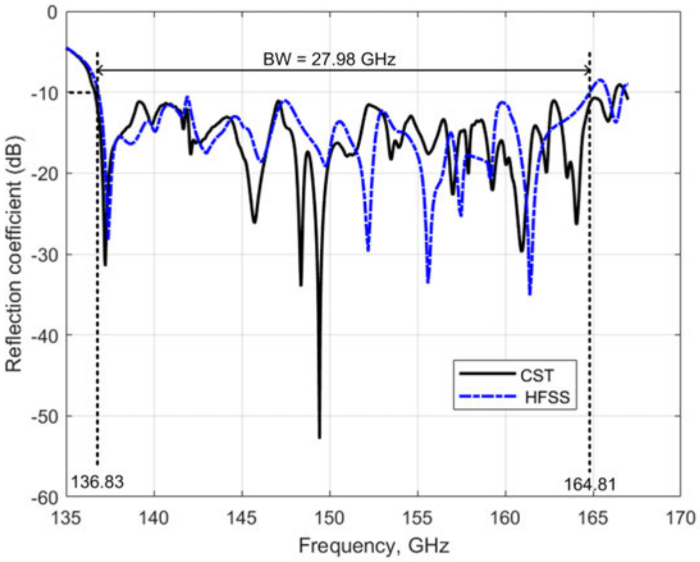

Figure 5.19: Performance comparison of the simulated $S_{11}$ curves of the proposed single element antenna in CST and HFSS.

the HFSS simulations for validation of the proposed design. diversity metrics of ECC, TARC and CCL are evaluated and presented.

Fig. 5.22 compares the ECC plots obtained from CST and HFSS simulations. The plots show that in both cases, ECC is below the standard limit of 0.5 for effective diversity performance.

Fig. 5.23 show plots for the TARC evaluated from HFSS simulations. The curves maintain the original characteristics of a single antenna, with changes in the magnitude of the reflection coefficients at different frequencies.

Finally, Fig. 5.24 compares the CCL plot obtained from CST and HFSS simulations. The curves exhibit close similarities and are within an acceptable limit of 0.4 bits/s/Hz in the passband. Therefore, the proposed design is suitable for application of MIMO antennas in D-band.

The performance of the proposed MIMO antenna is compared with similar previous works reported in [105], [106], [107], [108], [109], [110], [111], [112], [113] and [114]. Table 5.3 compares the performance of various antenna parameters for the different designs. We observe that the previously published MIMO antennas are designed in the mm-wave frequencies below 100 GHz. In terms of bandwidth and gain performances, the ME dipole design presented in [113] has a superior performance to the proposed design. The comparatively better gain is explained by the fact that the design uses a 2 × 2 antenna array as a single element in a 4 × 4 MIMO arrangement. Despite the radiation efficiency performance of the proposed MIMO design being relatively lower compared to those in [107], [108], [109], [110] and [111], it presents superior bandwidth and gain performances. In addition, the simulated radiation efficiency of 84% is satisfactorily high and does not render the design ineffective.

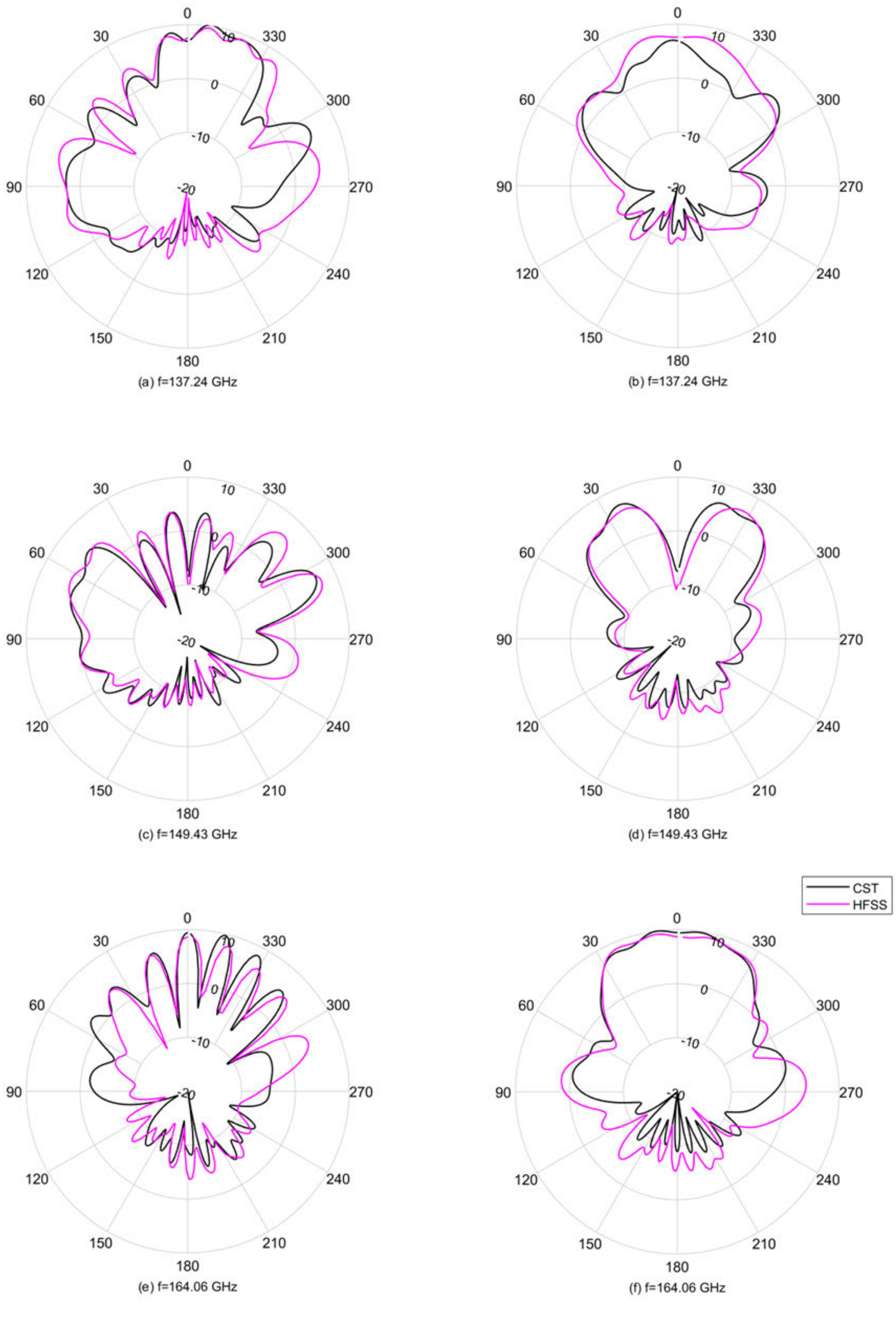

(a) f=137.24 GHz

(b) f=137.24 GHz

(c) f=149.43 GHz

(d) f=149.43 GHz

(e) f=164.06 GHz

(f) f=164.06 GHz

Figure 5.20: Performance comparison of the simulated E- and H-plane radiation patterns for the two $2 \times 2$ MIMO antennas using CST and HFSS at different frequencies.

The isolation performances of the MIMO designs are also compared. The performances of the designs [109], [110], [113] and [114] are superior to that of the presented design. The designs in [109] and [110] are based on $2 \times 2$ MIMO CDRA arranged to achieve $180^o$

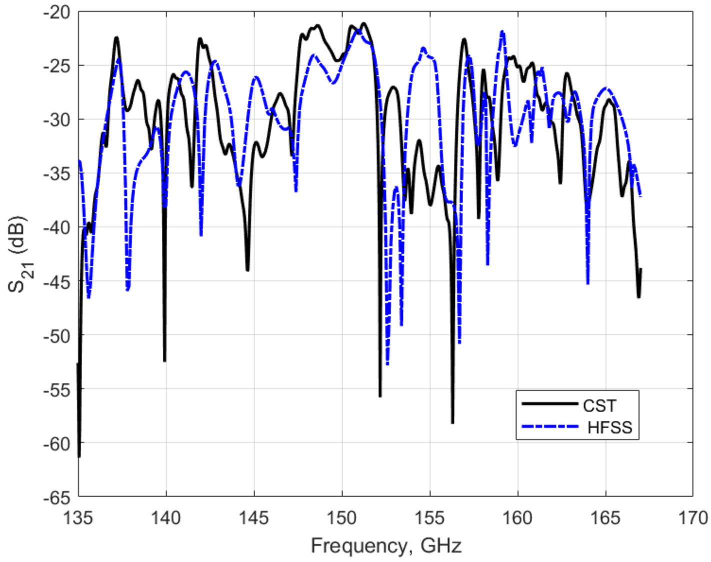

Figure 5.21: Performance comparison of the simulated $S_{21}$ curves of the proposed $2 \times 2$ MIMO antenna in CST and HFSS.

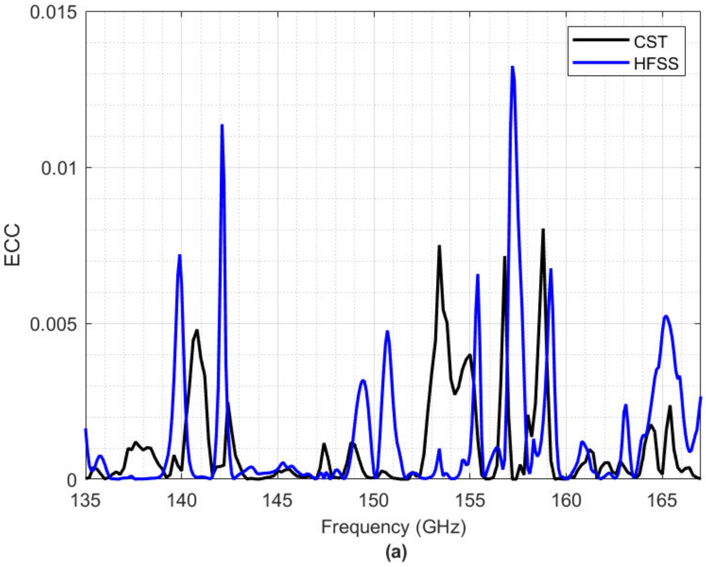

Figure 5.22: Graphs showing the performance comparison of the simulated ECC using CST and HFSS.

polarizations relative to each other. Similarly in [113], the $4 \times 4$ MIMO elements are arranged to achieve a $90^o$ orthogonal polarization between the individual elements. The design presented in [114] is a $2 \times 2$ SIW slot MIMO antenna arranged with a $90^o$ orthogonal polarization. This means that the designs in [109], [110], [113] and [114] employ more than one isolation technique involving polarization diversity in addition to the applied mutual reduction technique, whereas the elements of the proposed design are linearly arranged with a zero distance of separation between adjacent elements. The proposed design has an isolation performance $>$ 20 dB and allows for the integration of a higher number of antenna elements. This renders the proposed design a better choice for D-band MIMO

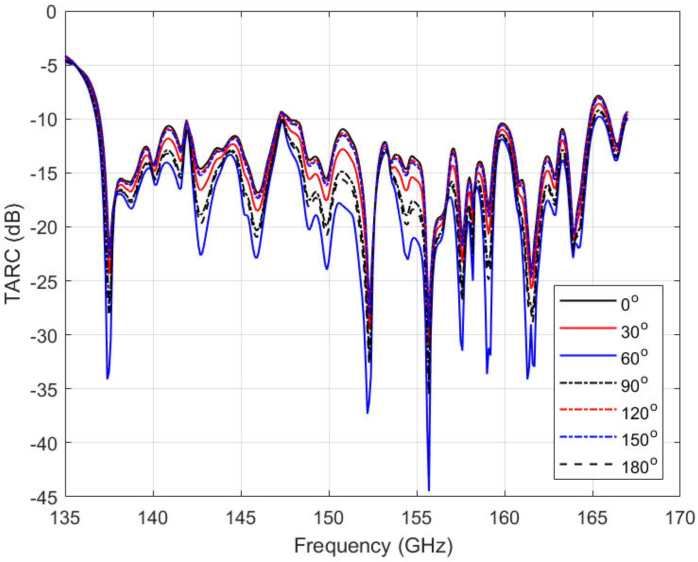

Figure 5.23: Graphs showing the HFSS simulation curves for TARC for the proposed 2 × 2 MIMO antenna.

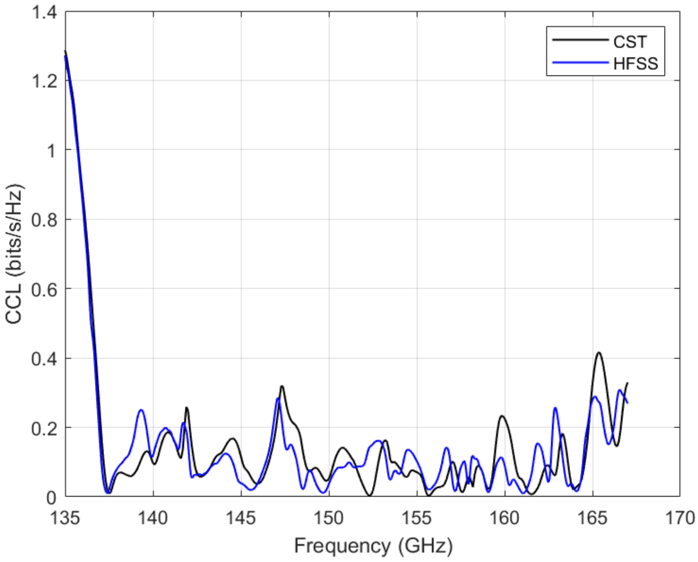

Figure 5.24: Graphs showing simulated channel capacity loss for the proposed 2 × 2 MIMO antenna using CST and HFSS.

applications.

Table 5.3: Performance comparison of the different MIMO antennas

| Ref | Type | Feeding | $f_0$(GHz) | BW | Gain,dBi | Efficiency | Isolation,dB | Technique |
|---|---|---|---|---|---|---|---|---|
| [105],2014 | MPA | Coplanar | 60 | 14.6% | - | - | -15 | Stub |
| [106],2017 | MPA | Microstrip | 57-64 | 12.3% | - | 50-60% | -15 | NL |
| [107],2021 | MPA | Microstrip | 60.4-68.9 | 13.14% | 8.8 | 96.5-98% | -15 | Patch holes + DGS |
| [108],2022 | MPA | Microstrip | 60 | 7% | 7.5 | 94% | -20 | AMC |
| [109],2017 | CDRA | Microstrip + slot | 57-63 | 10% | - | 90% | -30 | FSS wall |
| [110],2017 | CDRA | Microstrip | 56.6–64.8 | 13.5% | 7.9 | 91% | -30 | Metasurface wall |
| [111],2017 | CDRA | Microstrip + slot | 57-64 | 11.6% | - | 88% | -16 | MTMPR wall |
| [112],2012 | CDRA | Microstrip + slot | 57-64 | 11.6% | - | - | -15 | Superstrate + DGS |
| [113],2019 | ME dipole | MRWG | 57-71 | 21.9% | 14.5 | 82% | -30 | EBG |
| [114],2021 | Slot | SIW | 41.44 - 43.74 | 5.47% | 7.8 | - | -43.6 | Orthogonal diversity |
| **This work** | RDRA | SIW | 136.68–166.28 | 19.5% | 11.06 | 84% | -21.16 | MTMPR wall |

BW - Bandwidth, Efficiency - radiation efficiency, ME - Magneto-electric, MRWG - Microstrip ridge gap waveguide, NL - Neutralization line

## 5.4 Chapter summary

In this chapter, a SIW-DRA based 2 × 2 MIMO antenna for D-band frequency regime is presented. An MTMPR wall is integrated with the MIMO antenna isolation improvement. The proposed design possesses stable broadside radiation patterns and achieves a bandwidth of 19.5%, realized gain of 11.06 dB with isolation less than - 21.16 across the entire frequency of operation. The MIMO diversity metrics are within acceptable limits, rendering the proposed design suitable for D-band MIMO applications.

From the simulated results, we report the robustness of the SIW feed for MIMO applications. A well-designed SIW behaves like a metallic waveguide that confines all the energy within itself. Consequently, low isolation due to common ground effects and ground currents is minimized. Because of this reason, the inter-element spacing can be minimized to achieve higher integration. Therefore, a 2 × 2 MIMO topology, with zero inter-element distance of separation is proposed, to allow for high integration of antenna elements. In addition, an MTMPR wall is proposed and integrated into the MIMO for mutual coupling reduction and isolation enhancement. This provides a shield to minimize the spatial interaction of electromagnetic fields, with simulation results showing improvement in isolation performance.

# Chapter 6

# CONCLUSION AND FUTURE WORK

## 6.1 Conclusion

The preliminary chapters one and two presented the motivation for undertaking the study and the general theory necessary for the understanding of the radiation mechanism of the DRA as well as the design of SIW-fed DRAs. In chapters three, four and five, the different antenna designs are presented and evaluated. This chapter presents the conclusions which may be drawn from the performance evaluation of these designs.

In chapter three, a wideband SIW-DRA is presented. The design operates between 122.58 GHz to 139.51 GHz, with a -10 dB impedance bandwidth of 13.4%. The DR element is designed to operate in higher-order modes. The use of a DGS and via offset impedance matching techniques are effective in merging together the adjacent resonant bands for wideband operation. Besides the broad bandwidth, the antenna exhibits a peak gain of 12.3 dBi, a directivity of 13.14 dBi and a high radiation efficiency of 84 %. Moreover, the antenna radiates broadband radiation characteristics.

In chapter four, a wideband and high-gain antenna is presented in section 4. The design presents a systematic approach for the transformation of a dual-band antenna to a wideband design, through the application of impedance matching techniques to merge together the passbands of a dual-band antenna. The design demonstrates the effectiveness of embedding inductive vias in the SIW feed structure for DRA bandwidth improvement. The antenna achieves a -10 dB wideband bandwidth ranging from 123.97 GHz – 152.13 GHz, equivalent to 20.39%. The antenna has a peak gain of 11.67 dBi, directivity of 13.36 dBi and radiation efficiency of 79%. In addition, the antenna possesses a stable broadband radiation pattern in the frequency band of operation.

In chapter five, a $2 \times 2$ SIW-fed DRA MIMO antenna is presented. Two antenna elements are linearly arranged, with a zero inter-element distance of separation, to allow for high integration of antenna elements. An MTMPR wall is designed and integrated with the MIMO antenna to minimize mutual coupling between the tightly placed DR elements. The MTMPR wall shows improvement in the isolation without causing deterioration in the bandwidth performance. The MIMO antenna achieves a -10 dB bandwidth of 19.5%, peak gain of 11.06 dBi and a high radiation efficiency of 84%, with isolation less than - 21.16 dB across the frequency band of operation. The MIMO diversity metrics are evaluated and are within acceptable limits for practical antenna applications.

The future generation communication networks are expected to provide ubiquitous coverage, with potential frequencies for 6G communications in the sub-terahertz band. This is expected to provide the high data rates required to meet the data traffic demands of the connected devices. The general trends in antenna design towards 6G include the design of antennas at higher frequencies, use of low loss materials and incorporating of MIMO technology in the designs. In line with the objectives of this research, different antenna designs have been presented in this thesis to meet the requirements of future generation 6G wireless communications. The antennas performances demonstrate wide bandwidths, high gains and improved isolations for MIMO configurations at D-band. The presented antenna designs have the potential to offer solutions as antenna elements at D-band to meet the stringent requirements of increased network capacities and low latencies.

In conclusion, we present a summary of the research findings from the presented designs and analyses. These contributions can be summed up as follows:

(i) Design of high-gain, high radiation efficiency and wideband antennas for applications in D-band. The presented designs exhibit bandwidths of 13.4%, 20.39% and 19.5% with efficiencies of 84%, 79% and 84% respectively.

(ii) Development of a systematic approach for the transformation of a dual-band antenna to a wideband design, targeting the impedance improvement in the stop band without deteriorating the performance of the passbands. This has been demonstrated through the merging of dual bands of an antenna of 7.2% and 6.28% bandwidths in their passbands to realize a wide bandwidth of 20.39%.

(iii) The finding that the SIW structure offers a robust feed structure for MIMO applications. This enables the individual MIMO elements to be spaced very close to each other to achieve high integration of antenna elements. A high isolation of -19.51 dB is achieved for the case of no mutual coupling technique applied on the MIMO configuration.

(iv) Design of a MTMPR wall structure for the minimization of spatial interactions of electromagnetic fields between adjacent DRAs for isolation improvement. The designed MTMPW wall has a polarization conversion rate above 80% across the entire operating band and the integration of the wall with the MIMO antenna improves the isolation of the MIMO configuration from -19.51 dB to -21.16 dB.

## 6.2 Future work

In this thesis, wideband and high-gain antennas have been presented. These designs were based on LP DRAs. Linear polarized antennas require that the transmitter and the receiver are aligned so that there is minimization of polarization mismatches which lead to transmission loss and deterioration in the performance of wireless communication systems. CP waves are insensitive to polarization mismatch and allow for the flexible orientation between the transmitting and receiving devices while maintaining a constant level of signal reception. This has led to the development of CP antenna designs. For point-to-point communications at D-band, a LP beam may result in increased mismatch loss. The use of CP antennas relaxes the requirement of precise orientation of receiving and transmitting antenna systems for improved performance in future wireless systems. In addition, CP waves have better channel performance as well as low multipath interference when compared with linear polarization at millimeter waves.

Several techniques for the generation of CP waves in DRA antennas have been reported in literature. These techniques are based on single and multiple feeding arrangements, hybrid antennas elements, modifications of the shape of the feeding slot and its orientation, modifications in the DR element, excitation of multiple modes in the DR, incorporation of parasitic patches, metal coatings, metasurfaces among others. The future scope of our work is extension of the SIW-DRA to achieve CP antenna designs. We propose to incorporate CP techniques that will increase the DRA axial ratios without increasing the complexity of the antenna design and fabrication processes as well as minimization of complex geometries and fabrication complexities.

# References

[1] S. Henry, A. Alsohaily, and E. S. Sousa, “5g is real: Evaluating the compliance of the 3gpp 5g new radio system with the itu imt-2020 requirements,” *IEEE Access*, vol. 8, pp. 42 828–42 840, 2020.

[2] S. Kumar, A. S. Dixit, R. R. Malekar, H. D. Raut, and L. K. Shevada, “Fifth generation antennas: A comprehensive review of design and performance enhancement techniques,” *IEEE Access*, vol. 8, pp. 163 568–163 593, 2020.

[3] M. Hirzallah, M. Krunz, B. Kecicioglu, and B. Hamzeh, “5g new radio unlicensed: Challenges and evaluation,” *IEEE Transactions on Cognitive Communications and Networking*, vol. 7, no. 3, pp. 689–701, 2021.

[4] S. Chinkhong and P. Kaewplung, “A design approach for 5g-nr radio planning using both fr1 and fr2 on any selected outdoor and indoor areas,” in *2023 International Conference on Electronics, Information, and Communication (ICEIC)*, 2023, pp. 1–4.

[5] C.-X. Wang, X. You, X. Gao, X. Zhu, Z. Li, C. Zhang, H. Wang, Y. Huang, Y. Chen, H. Haas, J. S. Thompson, E. G. Larsson, M. D. Renzo, W. Tong, P. Zhu, X. Shen, H. V. Poor, and L. Hanzo, “On the road to 6g: Visions, requirements, key technologies and testbeds,” *IEEE Communications Surveys  Tutorials*, pp. 1–1, 2023.

[6] H. Sarieddeen, M.-S. Alouini, and T. Y. Al-Naffouri, “An overview of signal processing techniques for terahertz communications,” *Proceedings of the IEEE*, vol. 109, no. 10, pp. 1628–1665, 2021.

[7] P. Heydari, “Transceivers for 6g wireless communications: Challenges and design solutions,” in *2021 IEEE Custom Integrated Circuits Conference (CICC)*, 2021, pp. 1–8.

[8] M. Lotti, M. Caillet, and R. D’Errico, “Comparison of indoor channel characteristics for sub-thz bands from 125 ghz to 300 ghz,” in *2022 16th European Conference on Antennas and Propagation (EuCAP)*, 2022, pp. 1–5.

[9] N. Rajatheva, I. Atzeni, E. Bjornson, A. Bourdoux, S. Buzzi, J.-B. Dore, S. Erkucuk, M. Fuentes, K. Guan, Y. Hu, X. Huang, J. Hulkkonen, J. M. Jornet, M. Katz, R. Nilsson, E. Panayirci, K. Rabie, N. Rajapaksha, M. Salehi, H. Sarieddeen, T. Svensson, O. Tervo, A. Tolli, Q. Wu, and W. Xu, “White paper on broadband connectivity in 6g,” 2020.

[10] D. Seo, H. Kim, S. Oh, J. Kim, and J. Oh, "Ultrathin high-gain d-band transmitarray based on a spatial filter topology utilizing bonding layer effect," *IEEE Antennas and Wireless Propagation Letters*, vol. 21, no. 10, pp. 1945–1949, 2022.

[11] C. Ma, S. Ma, L. Dai, Q. Zhang, H. Wang, and H. Yu, "Wideband and high-gain d-band antennas for next-generation short-distance wireless communication chips," *IEEE Transactions on Antennas and Propagation*, vol. 69, no. 7, pp. 3700–3708, 2021.

[12] L. Zhou, M. Tang, Z. Gao, J. Mao, H. Yue, and Y. Tang, "Design and fabrication of patch antenna array on quartz glass substrate at 146 ghz," in *2020 International Conference on Microwave and Millimeter Wave Technology (ICMMT)*, 2020, pp. 1–3.

[13] A. Altaf, W. Abbas, and M. Seo, "A wideband siw-based slot antenna for *d*-band applications," *IEEE Antennas and Wireless Propagation Letters*, vol. 20, no. 10, pp. 1868–1872, 2021.

[14] D. Hou, W. Hong, W.-L. Goh, J. Chen, Y.-Z. Xiong, S. Hu, and M. Madihian, "D-band on-chip higher-order-mode dielectric-resonator antennas fed by half-mode cavity in cmos technology," *IEEE Antennas and Propagation Magazine*, vol. 56, no. 3, pp. 80–89, 2014.

[15] Y. Xu, S. Wen, and Y. Dong, "A d-band magneto-electric dipole antenna array based on ltcc technology," in *2021 IEEE International Workshop on Electromagnetics: Applications and Student Innovation Competition (iWEM)*, vol. volume1, 2021, pp. 1–3.

[16] K. Katoch and G. Singh, "Highly directive dielectric resonator rod array antenna at terahertz frequency for imaging applications," in *2017 Fourth International Conference on Image Information Processing (ICIIP)*, 2017, pp. 1–6.

[17] D. Soren, R. Ghatak, R. K. Mishra, and D. R. Poddar, "Dielectric resonator antennas: Designs and advances," *Progress in Electromagnetics Research B*, vol. 60, pp. 195–213, 2014.

[18] R. K. Mongia and P. Bhartia, "Dielectric resonator antennas—a review and general design relations for resonant frequency and bandwidth," *International Journal of Microwave and Millimeter-Wave Computer-Aided Engineering*, vol. 4, no. 3, pp. 230–247, 1994. [Online]. Available: https://onlinelibrary.wiley.com/doi/abs/10.1002/mmce.4570040304

[19] M. de Kok, A. B. Smolders, and U. Johannsen, "A review of design and integration technologies for d-band antennas," *IEEE Open Journal of Antennas and Propagation*, vol. 2, pp. 746–758, 2021.

[20] U. Nissanov, G. Singh, and N. Kumar, "High gain microstrip array antenna with siw and fss for beyond 5g at thz band," *Optik*, vol. 236, p. 166568, 2021. [Online]. Available: https://www.sciencedirect.com/science/article/pii/S0030402621002928

[21] S. Zhao, Y. Xu, and Y. Dong, "An ltcc-based antenna array for d-band terahertz communication," *IEEE Antennas and Wireless Propagation Letters*, pp. 1–5, 2023.

[22] D. Wang and K.-D. Xu, "Dual-band substrate integrated waveguide cavity-backed antenna based on ltcc in d-band," in *2022 International Applied Computational Electromagnetics Society Symposium (ACES-China)*, 2022, pp. 1–3.

[23] W. Zha, B. Feng, and X. Ding, "A flat wideband transmitarray antenna in d-band," in *2022 IEEE 5th International Conference on Electronic Information and Communication Technology (ICEICT)*, 2022, pp. 981–983.

[24] T. Saeidi and S. Karamzadeh, "High gain wide band flexible leaky wave mimo antenna for aip applications," in *2022 Workshop on Microwave Theory and Techniques in Wireless Communications (MTTW)*, 2022, pp. 90–94.

[25] G. Ulisse, G. Ducournau, and V. Krozer, "Antennas for a point to multi-point communication system operating in d-band," in *2021 46th International Conference on Infrared, Millimeter and Terahertz Waves (IRMMW-THz)*, 2021, pp. 1–2.

[26] S. R. Zahran, L. Boccia, G. Amendola, S. Moscato, M. Oldoni, and D. Tresoldi, "Broadband d-band antenna array based on 64 stepped horns for 5g backhauling applications," in *2021 15th European Conference on Antennas and Propagation (EuCAP)*, 2021, pp. 1–5.

[27] P. K. Verma, R. Kumar, and M. Singh, "Design and simulation of dielectric tapered rod as feed for dielectric lens antenna at 140 ghz," in *2008 International Conference on Recent Advances in Microwave Theory and Applications*, 2008, pp. 233–235.

[28] E. Usama, M. A. Basha, and S. Safavi-Naeini, "D-band compact and high gain pyramid dielectric antenna array using silicon technology," in *2018 18th International Symposium on Antenna Technology and Applied Electromagnetics (ANTEM)*, 2018, pp. 1–2.

[29] X. Wang, G. Xiao, L. Yang, H. Li, and Q. Xu, "Broadband d-band patch antenna array in wafer-level package based on bcb process," *IEEE Open Journal of Antennas and Propagation*, vol. 3, pp. 1172–1179, 2022.

[30] W. Ahmad, M. Kucharski, H. Ng, and D. Kissinger, "A compact efficient d-band micromachined on-chip differential patch antenna for radar applications," in *2019 IEEE International Symposium on Antennas and Propagation and USNC-URSI Radio Science Meeting*, 2019, pp. 2201–2202.

[31] W. A. Ahmad, M. Kucharski, A. Di Serio, H. J. Ng, C. Waldschmidt, and D. Kissinger, "Planar highly efficient high-gain 165 ghz on-chip antennas for

integrated radar sensors," *IEEE Antennas and Wireless Propagation Letters*, vol. 18, no. 11, pp. 2429–2433, 2019.

[32] Y. Wang, X. Yi, J. Xu, B. Zheng, W. Che, and Q. Xue, "Gain enhancement of millimeter-wave on-chip antenna through low-cost packaging technology," in *2022 IEEE 10th Asia-Pacific Conference on Antennas and Propagation (APCAP)*, 2022, pp. 1–2.

[33] B. Chen, Y. Tang, H. Yue, Z. Wen, H. Zhu, and X. Deng, "Ad-band wideband e-shaped patch loaded by open stubs for antenna in package (aip) application," in *2020 IEEE MTT-S International Wireless Symposium (IWS)*, 2020, pp. 1–3.

[34] H. Gulan, S. Beer, S. Diebold, P. Pahl, B. Goettel, and T. Zwick, "Cpw fed 2 × 2 patch array for d-band system-in-package applications," in *2012 IEEE International Workshop on Antenna Technology (iWAT)*, 2012, pp. 64–67.

[35] T. Li, K. Schneider, A. Haag, A. Visweswaran, A. Bhutani, and T. Zwick, "Design of wideband dielectric resonator antenna for d-band applications," in *2021 International Symposium on Antennas and Propagation (ISAP)*, 2021, pp. 1–2.

[36] H. Kim and J. Oh, "140-ghz wideband array antenna-in-package using multimode resonance," *IEEE Transactions on Antennas and Propagation*, vol. 71, no. 3, pp. 2136–2144, 2023.

[37] H.-C. Kuo, C.-W. Kuo, C.-C. Wang, and C.-P. Hung, "A d-band magnetoelectric dipole antenna-in-package (aip) implemented on bt-based organic substrate," *IEEE Transactions on Components, Packaging and Manufacturing Technology*, vol. 12, no. 10, pp. 1673–1680, 2022.

[38] X. Jia, X. Li, S. Erdogan, K.-S. Moon, J. W. Kim, K.-Q. Huang, M. B. Jordan, and M. Swaminathan, "Antenna with embedded die in glass interposer for 6g wireless applications," *IEEE Transactions on Components, Packaging and Manufacturing Technology*, vol. 13, no. 2, pp. 219–229, 2023.

[39] K.-Q. Huang and M. Swaminathan, "Antenna array on glass interposer for 6g wireless communications," *IEEE Transactions on Components, Packaging and Manufacturing Technology*, vol. 13, no. 2, pp. 211–218, 2023.

[40] L. N. Vijay Kumar and M. Swaminathan, "Ultra-wide bandwidth substrate integrated waveguide fed vivaldi antenna in d-band using glass interposer," in *2023 IEEE Radio and Wireless Symposium (RWS)*, 2023, pp. 150–152.

[41] S. Erdogan, K.-S. Jack Moon, M. Kathaperumal, and M. Swaminathan, "D-band integrated and miniaturized quasi yagi antenna array in glass interposer," *IEEE Transactions on Terahertz Science and Technology*, pp. 1–10, 2023.

[42] S. S. Yao, Y. J. Cheng, M. M. Zhou, Y. F. Wu, and Y. Fan, "D-band wideband air-filled plate array antenna with multistage impedance matching based on mems

micromachining technology," *IEEE Transactions on Antennas and Propagation*, vol. 68, no. 6, pp. 4502–4511, 2020.

[43] A. Bisognin, D. Titz, F. Ferrero, C. Luxey, G. Jacquemod, P. Brachat, C. Laporte, and H. Ezzeddine, "D-band quasi-yagi antenna in ipd process," in *2013 7th European Conference on Antennas and Propagation (EuCAP)*, 2013, pp. 330–331.

[44] C. Gu, S. Gao, V. Fusco, G. Gibbons, B. Sanz-Izquierdo, A. Standaert, P. Reynaert, W. Bösch, M. Gadringer, R. Xu, and X. Yang, "A d-band 3d-printed antenna," *IEEE Transactions on Terahertz Science and Technology*, vol. 10, no. 5, pp. 433–442, 2020.

[45] Q. Lai, C. Fumeaux, W. Hong, and R. Vahldieck, "60 ghz aperture-coupled dielectric resonator antennas fed by a half-mode substrate integrated waveguide," *IEEE Transactions on Antennas and Propagation*, vol. 58, no. 6, pp. 1856–1864, 2010.

[46] Y.-X. Guo and H. Chu, "60-ghz ltcc dielectric resonator antenna array," in *2013 IEEE Antennas and Propagation Society International Symposium (APSURSI)*, 2013, pp. 1874–1875.

[47] C. A. Balanis, *Antenna theory: analysis and design*, 3rd ed. John Wiley Sons, 2005.

[48] H. J. Visser, *Antenna theory and applications.* John Wiley & Sons, 2012.

[49] R. Richtmyer, "Dielectric resonators," *Journal of applied physics*, vol. 10, no. 6, pp. 391–398, 1939.

[50] S. Long, M. McAllister, and L. Shen, "The resonant cylindrical dielectric cavity antenna," *IEEE Transactions on Antennas and Propagation*, vol. 31, no. 3, pp. 406–412, 1983.

[51] K. M. Luk, K. W. Leung *et al.*, "Dielectric resonator antennas," Research studies press, Tech. Rep., 2003.

[52] R. Kumar Mongia and A. Ittipiboon, "Theoretical and experimental investigations on rectangular dielectric resonator antennas," *IEEE Transactions on Antennas and Propagation*, vol. 45, no. 9, pp. 1348–1356, 1997.

[53] Y.-M. Pan, K. W. Leung, and K.-M. Luk, "Design of the millimeter-wave rectangular dielectric resonator antenna using a higher-order mode," *IEEE Transactions on Antennas and Propagation*, vol. 59, no. 8, pp. 2780–2788, 2011.

[54] A. Buerkle, K. Sarabandi, and H. Mosallaei, "Compact slot and dielectric resonator antenna with dual-resonance, broadband characteristics," *IEEE Transactions on Antennas and Propagation*, vol. 53, no. 3, pp. 1020–1027, 2005.

[55] C.-P. Chua, P. A. Pavovich, R. M. Dragos, and M.-S. Leong, "A compact and wideband rectangular dielectric resonator antenna," in *2005 7th Electronic Packaging Technology Conference*, vol. 1. IEEE, 2005, pp. 4–pp.

[56] Y. Gao, Z. Feng, and L. Zhang, “Experimental investigation of new radiating mode in rectangular hybrid dielectric resonator antenna,” *IEEE Antennas and Wireless Propagation Letters*, vol. 10, pp. 91–94, 2011.

[57] M. Zou and J. Pan, “Investigation of resonant modes in wideband hybrid omnidirectional rectangular dielectric resonator antenna,” *IEEE Transactions on Antennas and Propagation*, vol. 63, no. 7, pp. 3272–3275, 2015.

[58] Y. Gao, Z. Feng, and L. Zhang, “Investigation of a new radiating mode and the traditional dominant mode in rectangular dielectric resonator antenna,” *IEEE Antennas and Wireless Propagation Letters*, vol. 11, pp. 909–912, 2012.

[59] T.-H. Chang and J.-F. Kiang, “Bandwidth broadening of dielectric resonator antenna by merging adjacent bands,” *IEEE Transactions on Antennas and Propagation*, vol. 57, no. 10, pp. 3316–3320, 2009.

[60] A. Petosa and S. Thirakoune, “Rectangular dielectric resonator antennas with enhanced gain,” *IEEE Transactions on Antennas and Propagation*, vol. 59, no. 4, pp. 1385–1389, 2011.

[61] S. Maity and B. Gupta, “Closed form expressions to find radiation patterns of rectangular dielectric resonator antennas for various modes,” *IEEE Transactions on Antennas and Propagation*, vol. 62, no. 12, pp. 6524–6527, 2014.

[62] M. Suma, P. Bijumon, M. Sebastian, and P. Mohanan, “A compact hybrid cpw fed planar monopole/dielectric resonator antenna,” *Journal of the European Ceramic Society*, vol. 27, no. 8, pp. 3001–3004, 2007, papers Presented at the Fourth International Conference on Microwave Materials and their Applications - MMA2006, Oulu, Finland. [Online]. Available: https://www.sciencedirect.com/science/article/pii/S0955221906006534

[63] U. Illahi, J. Iqbal, M. I. Sulaiman, M. M. Alam, M. M. Su’ud, and M. H. Jamaluddin, “Singly-fed rectangular dielectric resonator antenna with a wide circular polarization bandwidth and beamwidth for wimax/satellite applications,” *IEEE Access*, vol. 7, pp. 66 206–66 214, 2019.

[64] M. H. Seko and F. S. Correra, “Excitation of dielectric resonator antennas by loop coupling,” *IEEE Antennas and Wireless Propagation Letters*, vol. 18, no. 4, pp. 656–658, 2019.

[65] A. Kishk, G. Zhou, and A. Glisson, “Analysis of dielectric-resonator antennas with emphasis on hemispherical structures,” *IEEE Antennas and Propagation Magazine*, vol. 36, no. 2, pp. 20–31, 1994.

[66] T.-H. Chang and J.-F. Kiang, “Broadband dielectric resonator antenna with metal coating,” *IEEE Transactions on Antennas and Propagation*, vol. 55, no. 5, pp. 1254–1259, 2007.

[67] S. Keyrouz and D. Caratelli, "Dielectric resonator antennas: Basic concepts, design guidelines, and recent developments at millimeter-wave frequencies," *International Journal of Antennas and Propagation*, vol. 2016, pp. 1–20, 01 2016.

[68] W. J. Yang, Y. M. Pan, and P. F. Hu, "Circularly polarized filtering dielectric resonator antenna," in *2022 IEEE Conference on Antenna Measurements and Applications (CAMA)*, 2022, pp. 1–3.

[69] B. Thilagam, M. Kartha, and J. Kumar, "Performance analysis of cylindrical dielectric resonator antenna with various slot configurations on substrate integrated waveguide," *IJCTA*, vol. 9, pp. 7581–7588, 01 2016.

[70] D. Hou, Y.-Z. Xiong, W.-L. Goh, S. Hu, W. Hong, and M. Madihian, "130-ghz on-chip meander slot antennas with stacked dielectric resonators in standard cmos technology," *IEEE Transactions on Antennas and Propagation*, vol. 60, no. 9, pp. 4102–4109, 2012.

[71] P. Gupta, D. Guha, and C. Kumar, "Dual-mode cylindrical dra: Simplified design with improved radiation and bandwidth," *IEEE Antennas and Wireless Propagation Letters*, vol. 20, no. 12, pp. 2359–2362, 2021.

[72] X. S. Fang, L. P. Weng, and Z. Fan, "Design of the wideband and low-height omnidirectional cylindrical dielectric resonator antenna using arced-apertures feeding," *IEEE Access*, vol. 11, pp. 20 128–20 135, 2023.

[73] M.-D. Yang, Y.-M. Pan, Y.-X. Sun, and K.-W. Leung, "Wideband circularly polarized substrate-integrated embedded dielectric resonator antenna for millimeter-wave applications," *IEEE Transactions on Antennas and Propagation*, vol. 68, no. 2, pp. 1145–1150, 2020.

[74] S.-J. Guo, L.-S. Wu, K. W. Leung, and J.-F. Mao, "Microstrip-fed differential dielectric resonator antenna and array," *IEEE Antennas and Wireless Propagation Letters*, vol. 17, no. 9, pp. 1736–1739, 2018.

[75] C. Tong, B. Yang, X. Huang, N. Yang, X. Liu, and K. W. Leung, "Compact shared-aperture slot/dr antenna with large frequency ratio," *IEEE Antennas and Wireless Propagation Letters*, pp. 1–5, 2023.

[76] L.-X. Cui, X.-H. Ding, W.-W. Yang, L. Guo, L.-H. Zhou, and J.-X. Chen, "Communication compact dual-band hybrid dielectric resonator antenna for 5g millimeter-wave applications," *IEEE Transactions on Antennas and Propagation*, vol. 71, no. 1, pp. 1005–1010, 2023.

[77] S.-K. Zhao, N.-W. Liu, Q. Chen, G. Fu, and X.-P. Chen, "A low-profile dielectric resonator antenna with compact-size and wide bandwidth by using metasurface," *IEEE Access*, vol. 9, pp. 29 819–29 826, 2021.

[78] Y. Coulibaly, T. A. Denidni, and H. Boutayeb, “Broadband microstrip-fed dielectric resonator antenna for x-band applications,” *IEEE Antennas and Wireless Propagation Letters*, vol. 7, pp. 341–345, 2008.

[79] A. Petosa and A. Ittipiboon, “Dielectric resonator antennas: A historical review and the current state of the art,” *IEEE Antennas and Propagation Magazine*, vol. 52, no. 5, pp. 91–116, 2010.

[80] L. Guo, C. Zhou, H. Li, P. Chu, and W. W. Yang, “Low-profile and broadband dielectric resonator antenna using higher-order modes,” *IEEE Antennas and Wireless Propagation Letters*, vol. 20, no. 10, pp. 1988–1992, 2021.

[81] L. Wang, S.-W. Wong, X. Zhang, Y. He, L. Zhang, W. Li, and L. Zhu, “Stable high-gain linearly and circularly polarized dielectric resonator antennas based on multiple high-order modes,” *IEEE Transactions on Antennas and Propagation*, vol. 70, no. 12, pp. 12 270–12 275, 2022.

[82] Nasimuddin and K. P. Esselle, “A low-profile compact microwave antenna with high gain and wide bandwidth,” *IEEE Transactions on Antennas and Propagation*, vol. 55, no. 6, pp. 1880–1883, 2007.

[83] E. Erfani, T. Denidni, S. Tatu, and M. Niroo-Jazi, “A broadband and high gain millimeter-wave hybrid dielectric resonator antenna,” in *2016 17th International Symposium on Antenna Technology and Applied Electromagnetics (ANTEM)*, 2016, pp. 1–2.

[84] W.-W. Yang, X.-Y. Dong, Y.-L. Li, and J.-X. Chen, “A self-packaged circularly polarized dielectric resonator antenna with wide bandwidth and high gain,” *IEEE Antennas and Wireless Propagation Letters*, vol. 17, no. 12, pp. 2188–2192, 2018.

[85] Y. M. Pan and S. Y. Zheng, “A low-profile stacked dielectric resonator antenna with high-gain and wide bandwidth,” *IEEE Antennas and Wireless Propagation Letters*, vol. 15, pp. 68–71, 2016.

[86] M. Mrnka and Z. Raida, “Enhanced-gain dielectric resonator antenna based on the combination of higher-order modes,” *IEEE Antennas and Wireless Propagation Letters*, vol. 15, pp. 710–713, 2016.

[87] Z.-X. Xia and K. W. Leung, “Gain enhancement of rectangular dielectric resonator antenna using ebg surface,” in *2018 IEEE Asia-Pacific Conference on Antennas and Propagation (APCAP)*, 2018, pp. 102–103.

[88] M. Chauhan, A. Rajput, and B. Mukherjee, “Wideband circularly polarized low profile dielectric resonator antenna with meta superstrate for high gain,” *AEU - International Journal of Electronics and Communications*, vol. 128, p. 153524, 2021. [Online]. Available: https://www.sciencedirect.com/science/article/pii/S1434841120314527

[89] M. Akbari, S. Gupta, M. Farahani, A. R. Sebak, and T. A. Denidni, "Gain enhancement of circularly polarized dielectric resonator antenna based on fss superstrate for mmw applications," *IEEE Transactions on Antennas and Propagation*, vol. 64, no. 12, pp. 5542–5546, 2016.

[90] B. Bahreini, H. Oraizi, N. Noori, and S. Fakhte, "Design of a circularly polarized parasitic array with slot-coupled dra with improved gain for the 5g mobile system," *IEEE Antennas and Wireless Propagation Letters*, vol. 17, no. 10, pp. 1802–1806, 2018.

[91] K. Wu, D. Deslandes, and Y. Cassivi, "The substrate integrated circuits - a new concept for high-frequency electronics and optoelectronics," in *6th International Conference on Telecommunications in Modern Satellite, Cable and Broadcasting Service, 2003. TELSIKS 2003.*, vol. 1, 2003, pp. P–III.

[92] D. Pozar, *Microwave Engineering, 4th Edition.* Wiley, 2011. [Online]. Available: https://books.google.co.za/books?id=JegbAAAAQBAJ

[93] J. E. Rayas-Sanchez and V. Gutierrez-Ayala, "A general em-based design procedure for single-layer substrate integrated waveguide interconnects with microstrip transitions," in *2008 IEEE MTT-S International Microwave Symposium Digest*, 2008, pp. 983–986.

[94] L. Yan, W. Hong, G. Hua, J. Chen, K. Wu, and T. J. Cui, "Simulation and experiment on siw slot array antennas," *IEEE Microwave and Wireless Components Letters*, vol. 14, no. 9, pp. 446–448, 2004.

[95] J. Xu, Z. N. Chen, X. Qing, and W. Hong, "A single-layer siw slot array antenna with te20 mode," in *Asia-Pacific Microwave Conference 2011*, 2011, pp. 1330–1333.

[96] P. Wu, K. Liu, and Z. Yu, "220 ghz high-gain substrate integrated antennas with low fabrication cost based on higher order mode and pcb technology," *IEEE Transactions on Antennas and Propagation*, vol. 71, no. 1, pp. 18–28, 2023.

[97] M. M. Sani, R. Chowdhury, and R. K. Chaudhary, "Design and analysis of multiple input multiple output antenna for wideband applications using cylindrical dielectric resonator," *AEU - International Journal of Electronics and Communications*, vol. 131, p. 153598, 2021. [Online]. Available: https://www.sciencedirect.com/science/article/pii/S1434841120328028

[98] G. Das, N. K. Sahu, and R. K. Gangwar, "Dielectric resonator based multiport antenna system with multi-diversity and built-in decoupling mechanism," *AEU - International Journal of Electronics and Communications*, vol. 119, p. 153193, 2020. [Online]. Available: https://www.sciencedirect.com/science/article/pii/S143484112030399X

[99] R. Mondal, P. S. Reddy, D. C. Sarkar, and P. P. Sarkar, "Investigation on mimo antenna for very low ecc and isolation characteristics using fss and metal-wall,"

*AEU - International Journal of Electronics and Communications*, vol. 135, p. 153708, 2021. [Online]. Available: https://www.sciencedirect.com/science/article/pii/S1434841121001059

[100] D. Serghiou, M. Khalily, V. Singh, A. Araghi, and R. Tafazolli, "Sub-6 ghz dual-band $8 \times 8$ mimo antenna for 5g smartphones," *IEEE Antennas and Wireless Propagation Letters*, vol. 19, no. 9, pp. 1546–1550, 2020.

[101] J. L. Volakis, *Antenna engineering handbook.* McGraw-Hill Education, 2007.

[102] S. Catreux, P. Driessen, and L. Greenstein, "Data throughputs using multiple-input multiple-output (mimo) techniques in a noise-limited cellular environment," *IEEE Transactions on Wireless Communications*, vol. 1, no. 2, pp. 226–235, 2002.

[103] U. Sharma and G. Srivastava, "A study of various techniques to reduce mutual coupling in mimo antennas," in *2020 Second International Conference on Inventive Research in Computing Applications (ICIRCA)*, 2020, pp. 1–7.

[104] R. S. Aziz, S. Koziel, L. Leifsson, and S. Szczepanski, "A study of mutual coupling suppression between two closely spaced planar monopole antenna elements for 5g new radio massive mimo system applications," *Electronics*, vol. 12, no. 12, 2023. [Online]. Available: https://www.mdpi.com/2079-9292/12/12/2630

[105] C. Zhang and P. Gao, "A planar 60ghz antenna for mimo/diversity applications," in *2014 15th International Conference on Electronic Packaging Technology*, 2014, pp. 1350–1352.

[106] K. Pedram, M. Karamirad, and S. M. Husain Ranjbaran, "A novel circular polarization mimo antenna in 60 ghz technology," in *2017 IEEE 4th International Conference on Knowledge-Based Engineering and Innovation (KBEI)*, 2017, pp. 0335–0338.

[107] S. Singh, A. Kumar Singh, Karunesh, A. Pandey, and R. Singh, "A novel mimo microstrip patch antenna for 5g applications," in *2021 International Conference on Computing, Communication, and Intelligent Systems (ICCCIS)*, 2021, pp. 828–833.

[108] G. Raviteja, "A linearly arranged quad-port wideband mimo antenna with amc for 60 ghz millimeter-wave applications," in *2022 First International Conference on Electrical, Electronics, Information and Communication Technologies (ICEEICT)*, 2022, pp. 1–9.

[109] R. Karimian, A. Kesavan, M. Nedil, and T. A. Denidni, "Low-mutual-coupling 60-ghz mimo antenna system with frequency selective surface wall," *IEEE Antennas and Wireless Propagation Letters*, vol. 16, pp. 373–376, 2017.

[110] A. Dadgarpour, B. Zarghooni, B. S. Virdee, T. A. Denidni, and A. A. Kishk, "Mutual coupling reduction in dielectric resonator antennas using metasurface shield for 60-ghz mimo systems," *IEEE Antennas and Wireless Propagation Letters*, vol. 16, pp. 477–480, 2017.

[111] M. Farahani, J. Pourahmadazar, M. Akbari, M. Nedil, A. R. Sebak, and T. A. Denidni, “Mutual coupling reduction in millimeter-wave mimo antenna array using a metamaterial polarization-rotator wall,” *IEEE Antennas and Wireless Propagation Letters*, vol. 16, pp. 2324–2327, 2017.

[112] A. Hagras, T. A. Denidni, M. Nedil, and Y. Coulibaly, “Low-mutual coupling antenna array for millimeter-wave mimo applications,” in *Proceedings of the 2012 IEEE International Symposium on Antennas and Propagation*, 2012, pp. 1–2.

[113] A. T. Hassan and A. A. Kishk, “4×4 mimo antenna elements fed by microstrip ridge gap waveguide,” in *2019 IEEE International Symposium on Antennas and Propagation and USNC-URSI Radio Science Meeting*, 2019, pp. 419–420.

[114] P. Liu, X.-W. Zhu, Y. Zhang, L. Tian, Z. H. Jiang, and N. Zhang, “2-element slot antenna array based on substrate integrated waveguide at q-band,” in *2020 International Symposium on Antennas and Propagation (ISAP)*, 2021, pp. 393–394.

[115] C. A. Balanis, *Advanced engineering electromagnetics.* John Wiley & Sons, 2012.

[116] B. Ajewole, P. Kumar, and T. Afullo, “I-shaped metamaterial using srr for multi-band wireless communication,” *Crystals*, vol. 12, no. 4, 2022. [Online]. Available: https://www.mdpi.com/2073-4352/12/4/559

[117] S. B. Glybovski, S. A. Tretyakov, P. A. Belov, Y. S. Kivshar, and C. R. Simovski, “Metasurfaces: From microwaves to visible,” *Physics Reports*, vol. 634, pp. 1–72, 2016, metasurfaces: From microwaves to visible. [Online]. Available: https://www.sciencedirect.com/science/article/pii/S0370157316300618

[118] S. Yadav, M. P. Abegaonkar, M. M. Sharma, and C. P. Jain, “A quad-band polarization independent metamaterial absorber,” in *2017 IEEE Applied Electromagnetics Conference (AEMC)*, 2017, pp. 1–2.

[119] S. H. Zainud-Deen, M. M. Badawy, and H. A. Malhat, “Dielectric resonator antenna loaded with metamaterial polarizer for circular polarization,” in *2019 36th National Radio Science Conference (NRSC)*, 2019, pp. 76–83.

[120] R. Ahila Priyadharshini, S. Arivazhagan, M. Arun, and A. Arunadevi, “Half mode rogers rt duroid 5880 substrate integrated waveguide cavity backed v-slot antenna for c-band applications,” *Materials Today: Proceedings*, vol. 37, pp. 1854–1858, 2021, international Conference on Newer Trends and Innovation in Mechanical Engineering: Materials Science. [Online]. Available: https://www.sciencedirect.com/science/article/pii/S2214785320355565

[121] J. Wang, Z.-C. Hao, and K.-K. Fan, “A 110–150 ghz siw-rectangular waveguide transition for terahertz applications,” in *2016 IEEE MTT-S International Microwave Workshop Series on Advanced Materials and Processes for RF and THz Applications (IMWS-AMP)*, 2016, pp. 1–3.

[122] A. Saxena, S. Joshi, A. Gupta, S. Saxena, and D. Kumar, “Gain and bandwidth enhancement of cpw-fed patch antenna for wideband applications,” in *2016 IEEE International Conference on Recent Trends in Electronics, Information Communication Technology (RTEICT)*, 2016, pp. 1622–1625.

[123] Y. M. Pan, K. W. Leung, and K. Lu, “Study of resonant modes in rectangular dielectric resonator antenna based on radar cross section,” *IEEE Transactions on Antennas and Propagation*, vol. 67, no. 6, pp. 4200–4205, 2019.

[124] W. M. Abdel Wahab, D. Busuioc, and S. Safavi-Naeini, “Low cost planar waveguide technology-based dielectric resonator antenna (dra) for millimeter-wave applications: Analysis, design, and fabrication,” *IEEE Transactions on Antennas and Propagation*, vol. 58, no. 8, pp. 2499–2507, 2010.

[125] P. Bhartia, I. Bahl, R. Garg, and A. Ittipiboon, *Microstrip Antenna Design Handbook*. Artech House Publishers, 2001.

[126] A. P. Kumar and A. K. Ojha, “Cross-polarization reduction of a cylindrical dielectric resonator antenna with parasitic strip loading,” in *2018 International Conference on Signal Processing and Communications (SPCOM)*, 2018, pp. 139–142.

[127] C. Kumar and D. Guha, “Nature of cross-polarized radiations from probe-fed circular microstrip antennas and their suppression using different geometries of defected ground structure (dgs),” *IEEE Transactions on Antennas and Propagation*, vol. 60, no. 1, pp. 92–101, 2012.

[128] X. Yi and H. Wong, “A wideband substrate integrated waveguide-fed open slot antenna,” *IEEE Transactions on Antennas and Propagation*, vol. 68, no. 3, pp. 1945–1952, 2020.

[129] R. E. Collin, *Field Theory of Guided Waves*, 2nd ed., ser. IEEE Press Series on Electromagnetic Wave Theory. Wiley, 1991.

[130] W. Luo, Y. Feng, Y. Ren, and B. Yin, *AEU - International Journal of Electronics and Communications*, vol. 142, p. 153984, 2021. [Online]. Available: https://www.sciencedirect.com/science/article/pii/S1434841121003812

[131] A. Sharma, A. Sarkar, A. Biswas, and M. J. Akhtar, “Millimeter-wave quad-port multiple-input multiple-output dielectric resonator antenna excited differentially by te20 mode substrate integrated waveguide,” in *2019 URSI Asia-Pacific Radio Science Conference (AP-RASC)*, 2019, pp. 1–4.

[132] P. Rajat Girjashankar and T. Upadhyaya, “Substrate integrated waveguide fed dual band quad-elements rectangular dielectric resonator mimo antenna for millimeter wave 5g wireless communication systems,” *AEU - International Journal of Electronics and Communications*, vol. 137, p. 153821, 2021. [Online]. Available: https://www.sciencedirect.com/science/article/pii/S1434841121002181

[133] K. Gong and X. H. Hu, “Low-profile substrate integrated dielectric resonator antenna implemented with pcb process,” *IEEE Antennas and Wireless Propagation Letters*, vol. 13, pp. 1023–1026, 2014.

[134] M. Mrnka, M. Cupal, Z. Raida, A. Pietrikova, and D. Kocur, “Millimetre-wave dielectric resonator antenna array based on directive ltcc elements,” *IET Microwaves, Antennas & Propagation*, vol. 12, no. 5, pp. 662–667, 2018.

[135] D. Deslandes and K. Wu, “Integrated microstrip and rectangular waveguide in planar form,” *IEEE Microwave and Wireless Components Letters*, vol. 11, no. 2, pp. 68–70, 2001.

[136] M. Abdolhamidi and M. Shahabadi, “X-band substrate integrated waveguide amplifier,” *IEEE Microwave and Wireless Components Letters*, vol. 18, no. 12, pp. 815–817, 2008.

[137] Z. Wang, S. Adhikari, D. Dousset, C.-W. Park, and K. Wu, “Substrate integrated waveguide (siw) power amplifier using cbcpw-to-siw transition for matching network,” in *2012 IEEE/MTT-S International Microwave Symposium Digest*, 2012, pp. 1–3.

[138] R. E. Collin, *Field Theory of Guided Waves*, 2nd ed., ser. IEEE Press Series on Electromagnetic Wave Theory. Wiley, 1991.

[139] N. Marcuvitz, *Waveguide handbook.* Peregrinus, 1986.

[140] E. K. Chemweno, P. Kumar, and T. J. O. Afullo, “Bandwidth enhancement of a substrate integrated waveguide dielectric resonator antenna using metallic shorting vias,” in *2022 International Conference on Electromagnetics in Advanced Applications (ICEAA)*, 2022, pp. 302–305.

[141] E. K. Chemweno, P. Kumar, and T. J. O. Afullo, “Substrate integrated waveguide - dielectric resonator antenna for future wireless communication,” *SAIEE Africa Research Journal*, vol. 113, no. 3, pp. 119–128, 2022.

[142] A. Sharma, A. Sarkar, A. Biswas, R. Sloan, and Z. Hu, “A polarization diversity substrate integrated waveguide fed rectangular dielectric resonator antenna,” in *2016 Asia-Pacific Microwave Conference (APMC)*, 2016, pp. 1–4.

[143] D. Deslandes and K. Wu, “Accurate modeling, wave mechanisms, and design considerations of a substrate integrated waveguide,” *IEEE Transactions on Microwave Theory and Techniques*, vol. 54, no. 6, pp. 2516–2526, 2006.

[144] A. O. Nwajana and E. R. Obi, “A review on siw and its applications to microwave components,” *Electronics*, vol. 11, no. 7, 2022. [Online]. Available: https://www.mdpi.com/2079-9292/11/7/1160

[145] P.-C. Tang, L.-M. Si, G. Cheng, W.-D. Hu, X. Lv, and Z.-S. Li, “Broadband high transmittance 220 ghz polarization rotator with chiral metamaterial,” in *2020 Cross Strait Radio Science  Wireless Technology Conference (CSRSWTC)*, 2020, pp. 1–3.

[146] Z. Faraz, B. Kamal, S. Ullah, A. Aziz, and H. Kanwal, “High efficient and ultra-wideband polarization converter based on i-shaped metasurface for rcs reduction,” *Optics Communications*, vol. 530, p. 129101, 2023. [Online]. Available: https://www.sciencedirect.com/science/article/pii/S0030401822007489

[147] M. A. Ul Haq and S. Koziel, “Ground plane alterations for design of high-isolation compact wideband mimo antenna,” *IEEE Access*, vol. 6, pp. 48 978–48 983, 2018.

[148] S. Ghosh and M. V. Swati, “A compact mm-wave mimo antenna array,” in *2021 Asian Conference on Innovation in Technology (ASIANCON)*, 2021, pp. 1–4.

[149] P. Sharma, R. N. Tiwari, P. Singh, P. Kumar, and B. K. Kanaujia, “Mimo antennas: Design approaches, techniques and applications,” *Sensors*, vol. 22, no. 20, pp. 1–25, 2022. [Online]. Available: https://www.mdpi.com/1424-8220/22/20/7813

[150] X. Zhou, X. Quan, and R. Li, “A dual-broadband mimo antenna system for gsm/umts/lte and wlan handsets,” *IEEE Antennas and Wireless Propagation Letters*, vol. 11, pp. 551–554, 2012.